ANALYSIS AND INTERPRETATION OF VOLCANO DEFORMATION IN ALASKA:

STUDIES FROM OKMOK AND MT. VENIAMINOF VOLCANOES

By

Thomas J. Fournier

RECOMMENDED:

_____
Dr. Jessica Larsen

_____
Dr. Peter Cervelli

_____
Dr. Douglas Christensen

_____
Dr. Stephen McNutt

_____
Dr. Jeffrey Freymueller, Advisory Committee Chair

_____
Dr. Michael Whalen, Chair, Department of Geology and Geophysics

APPROVED:

_____
Dr. Joan Braddock, Dean, College of Natural Science and Mathematics

_____
Dr. Lawrence K. Duffy, Dean of the Graduate School

_____
Date

ANALYSIS AND INTERPRETATION OF VOLCANO DEFORMATION IN ALASKA: STUDIES FROM OKMOK AND MT. VENIAMINOF VOLCANOES

A

THESIS

Presented to the Faculty

of the University of Alaska Fairbanks

in Partial Fulfillment of the Requirements

for the Degree of

DOCTOR OF PHILOSOPHY

By

Thomas J. Fournier, B.A.

Fairbanks, Alaska

December 2008

Abstract

Four studies focus on the deformation at Okmok Volcano, the Alaska Peninsula and Mt. Veniaminof. The main focus of the thesis is the volcano deformation at Okmok Volcano and Mt. Veniaminof, but also includes an investigation of the tectonic related compression of the Alaska Peninsula. The complete data set of GPS observations at Okmok Volcano are investigated with the Unscented Kalman Filter time series analysis method. The technique is shown to be useful for inverting geodetic data for time dependent non-linear model parameters. The GPS record at Okmok from 2000 to mid 2007 shows distinct inflation pulses which have several months duration. The inflation is interpreted as magma accumulation in a shallow reservoir under the caldera center and approximately 2.5km below sea level. The location determined for the magma reservoir agrees with estimates determined by other geodetic techniques. Smaller deflation signals in the Okmok record appear following the inflation pulses. A degassing model is proposed to explain the deflation. Petrologic observations from lava erupted in 1997 provide an estimate for the volatile content of the magma. The solution model VolatileCalc is used to determine the amount of volatiles in the gas phase. Degassing can explain the deflation, but only under certain circumstances. The magma chamber must have a radius between ~1and 2km and the intruding magma must have less than approximately 500ppm CO_2. At Mt. Veniaminof the deformation signal is dominated by compression caused by the convergence of the Pacific and North American Plates. A subduction model is created to account for the site velocities. A network of GPS benchmarks along the Alaska Peninsula is used to infer the amount of coupling along the mega-thrust. A transition from high to low coupling near the Shumagin Islands has important implications for the seismogenic potential of this section of the fault. The Shumagin segment likely ruptures in more frequent smaller magnitude quakes. The tectonic study provides a useful backdrop to examine the volcano deformation at Mt. Veniaminof. After being corrected for tectonic motion the sites velocities indicate inflation at the volcano. The deformation is interpreted as pressurization occurring beneath the volcano associated with eruptive activity in 2005.

Table of Contents

Page

List of Figures

Page

List of Tables

Acknowledgments

I would like to acknowledge the many people who contributed to this work and supported me in this endeavor; unfortunately there is not enough space here to list them all.

I would like to thank my Advisory Committee in particular, their guidance, input and scientific perspectives helped to shape these studies. In particular Jeff Freymueller contributed much time and effort to the work presented here. For this I am grateful. Peter Cervelli, Jessica Larsen, Steve McNutt and Doug Christiansen all provided valuable insight and direction when it was needed.

I must thank my fellow graduate students, particularly Samik Sil, Ryan Cross, and Julie Elliot, who helped to create a collaborative learning environment. Their willingness to share ideas and offer constructive criticism on a daily basis helped to broaden my perspective. Without their support and the support of many other students there is no doubt that this work would have been far more difficult.

The University of Alaska Fairbanks, Geophysical Institute, Alaska Volcano Observatory, and Geophysical Society of Alaska provided financial support for my education. Larry Mastin and Kaj Johnson provided computer code that I used for different aspects of this project. I am grateful to the USGS staff at the Alaska Volcano Observatory in Anchorage for welcoming me to join them for the final two years of my studies.

Finally, I owe a great deal of gratitude to my loving wife Kelly for all of her support and encouragement. Without her, accomplishing this goal would not have been possible. My family provided an enormous amount of motivation, support and sometimes a needed distraction. Thank you, Michael, Laurel, Mom, and Dad for being there for me.

Chapter 1: Interpreting Volcano Deformation in Alaska

1.1 Introduction

Surface deformation has long been studied at active volcanoes and has been documented as a signal of unrest. It can signify that an eruption is imminent, but can also occur without an ensuing eruption. The following chapters explore the insight that surface deformation reveals about subsurface processes using modern instruments.

This thesis presents studies at two different volcanoes in Alaska: Okmok and Mt. Veniaminof. At each location the Global Positioning System (GPS) data are inverted for deformation source geometries. At Okmok petrologic data and a volatile solution model are used to examine the impact that volatiles have on the deformation record. At Mt. Veniaminof seismic and geologic observations are used to put the deformation into the context of the volcanic system. The deformation is associated with eruptive activity that occurred in the interval between observations. A subduction zone model is also presented. The main motivation of the study was to provide a better frame of reference for the observation at Mt. Veniaminof, but the results reveal abrupt changes along the subduction interface.

1.2 Chapter Overviews

1.2.1 Chapter 2

The high activity rate of Okmok Volcano makes it ideal for studying magmatic processes and the accessibility of the volcano allows for an optimally distributed GPS network. Continuous GPS instruments (CGPS) installed in 2002 give a detailed look at the evolution of deformation events. In Chapter 2 an examination of the deformation record reveals rapid inflation of the volcano associated with intrusion of magma into a shallow reservoir. A time series analysis method is used to track the volume change in the shallow reservoir.

1.2.2 Chapter 3

Chapter 3 explores some of the subtler details in the deformation record at Okmok. In particular a degassing model is proposed to explain the deflation signals that follow prominent inflation periods. Degassing is a likely explanation for the deflation signals. Petrologic studies provide constraints on the composition and volatile content of the magma. The degassing model describes the deformation and provides additional constraints on the magma chamber size and volatile content of the magma.

1.2.3 Chapter 4

The convergence of the Pacific plate with the North American plate creates a significant amount of compression across the Alaska Peninsula. In order to investigate the volcanic signal at Mt. Veniaminof a subduction model is created to account for the plate convergence. The model shows an abrupt change in character along the plate interface, which has important implications for the seismic hazard along this section of the subduction zone.

1.2.4 Chapter 5

Unlike Okmok Volcano, Mt. Veniaminof has a very short history of deformation observations (the observations published here are the first recorded at Mt. Veniaminof). The short observation history and the fact that observations were conducted in two campaigns means that there is no temporal information in the data. The data set is useful for examining the location and magnitude of the deformation source, which can be combined with other information to better understand the magmatic processes beneath the volcano. In Chapter 5 the data are examined in the context of the eruptive activity in 2005.

1.2.5 Chapter 6

In Chapter 6 a summary of results from the previous chapters is presented. Some ideas on how these studies can be expanded and how the results can be applied are proposed.

Chapter 2: Tracking Magma Volume Recovery at Okmok Volcano Using an Unscented Kalman Filter[1]

2.1 Abstract

Changes beneath a volcano can be observed through position changes in a GPS network, but distinguishing the source of site motion is not always straightforward. The records of continuous GPS sites provide a favorable data set for tracking magma migration. Dense campaign observations usually provide a better spatial picture of the overall deformation field, at the expense of an episodic temporal record. Combining these observations provides the best of both worlds. A Kalman filter provides a means for integrating discrete and continuous measurements and for interpreting subtle signals. The Unscented Kalman Filter (UKF) is a non-linear method for time-dependent observations. We demonstrate the application of this technique to deformation data by applying it to GPS data collected at Okmok volcano. Seven years of GPS observations at Okmok are analyzed using a Mogi source model and the UKF. The deformation source at Okmok is relatively stable at 2.5km depth below sea level, located beneath the center of the caldera, which means the surface deformation is caused by changes in the strength of the source. During the seven years of GPS observations more than 0.5m of uplift has occurred, a majority of that during the time period January 2003 to July 2004. The total volume recovery at Okmok since the last eruption in 1997 is ~60-80%. The UKF allows us to solve simultaneously for the time-dependence of the source strength and for the location without a priori information about the source.

2.2 Introduction

Volcanic deformation measurement is a powerful tool used to gain insight to the interior dynamics of a volcano. The recent increase in the number of continuous deformation instruments makes this tool available at many volcanoes. Most continuously

[1] Fournier, T., J. Freymueller, and P. Cervelli, (2008), Tracking magma volume recovery at Okmok Volcano using an Unscented Kalman Filter, *J. Geophys. Res., doi:10.1029/*2008JB005837.

recording networks are augmented by campaign surveys that provide better spatial coverage than the continuous network alone, but which lack the temporal continuity of the continuous network. Okmok volcano has a well distributed campaign network and continuously operating GPS instruments (Fig. 2.1), which provide a record of the deformation that has occurred there over the past 7 years. We incorporate the available GPS data for a time-dependent analysis of the deformation.

Okmok is a shield volcano with a 10-km diameter summit caldera, located in the Aleutian Arc. It occupies the northeasternmost part of Umnak Island (Fig. 2.1). Frequent eruptions at Okmok make it an ideal volcano to study the dynamics of intrusive and eruptive behavior. Okmok has had an eruption every ten to twenty years for the past several hundred years and possibly longer [*Begét et al., 2005; Miller et al., 1998*]. The 1997 eruption emanated from Cone A, located in the southwest quadrant of the caldera, while the most recent eruption occurred in 2008 and produced new vents near Cone D (Fig. 2.1). The 1997 eruption produced an extensive basaltic lava flow that is 5km long and tens of meters thick [*Lu et al., 2003a*]. An eruption in 1958, from Cone A, produced a similar sized basalt flow [*Grey, 2003*] and intermittent ash eruptions from Cone A occurred in 1960, 1981, 1983, and 1986 [*Begét et al., 2005*]. The 2008 eruption was similar to an 1817 eruption that also occurred in the northern part of the caldera. Both of these eruptions produced mainly tephra, a result of the magma interacting with the water table. The caldera was formed by eruptions 12000 and 2050 years ago, in which basaltic andesite was the most voluminous eruptive product [*Finney et al., 2008*].

Since 1992, InSAR and GPS observations have been used to learn about surface deformation at the volcano. These observations show inflation prior to the 1997 eruption, co-eruptive deflation and continued inflation following the eruption [*Mann et al., 2002; Lu et al., 2000; Lu et al., 2005*]. In 2000 the first of yearly campaign GPS measurements were made and in 2002 continuous GPS instruments were installed at a few sites on the volcano. Results from the early campaigns show continued inflation at the volcano [*Miyagi et al., 2004*]. Both data sources, InSAR and GPS, indicate a fairly stable

deformation source at ~3km below the surface of the center of the caldera. The overall deformation field before, during and after the 1997 eruption is dominated by this source. Previous studies [*Mann et al., 2002; Lu et al., 2000; Lu et al., 2005; Miyagi et al., 2004*] all used time independent models to find the best source geometry. We show here that even with a time-dependent model a stable source location is the preferred geometry.

In this paper we present data from the continuous sites and repeat surveys of the campaign sites. The well-distributed campaign GPS network on Okmok gives a good representation of the displacement field, which allows for accurate modeling of the deformation source. The time series from the continuous sites show the temporal history of deformation in much more detail. The two data types are complementary and together allow us to better understand the processes working beneath Okmok. We model all the available GPS data collected at Okmok and compare two models, the first with a freely moving source and the second with a fixed source. Both cases highlight the stability of the deformation source at Okmok. Since the two model results have only minor differences, the fixed model, being the simpler model, is preferred.

The Kalman Filter is a natural method to incorporate both continuous and campaign measurements for both temporal continuity and spatial coverage to better resolve a time-varying deformation source. The Kalman Filter has one significant limitation in that it is a linear method and most deformation source models are non-linear. An often used work around is to assume a fixed orientation and solve for the linear parameter, a strength or magnitude term. This method works very well if an optimal geometry is chosen and if the geometry does not change over the time period of interest. If the optimal geometry is unknown then the non-linear nature of the problem cannot be avoided. We present here a non-linear Kalman Filter that estimates time-varying deformation parameters and their covariance without calculation of partial derivatives.

As the number of continuously recording GPS instruments has increased, the Kalman filter has gained popularity as a time-dependent modeling technique, particularly for determining fault-slip evolution [*e.g. Segall and Matthew, 1997; Segall et al., 2000;*

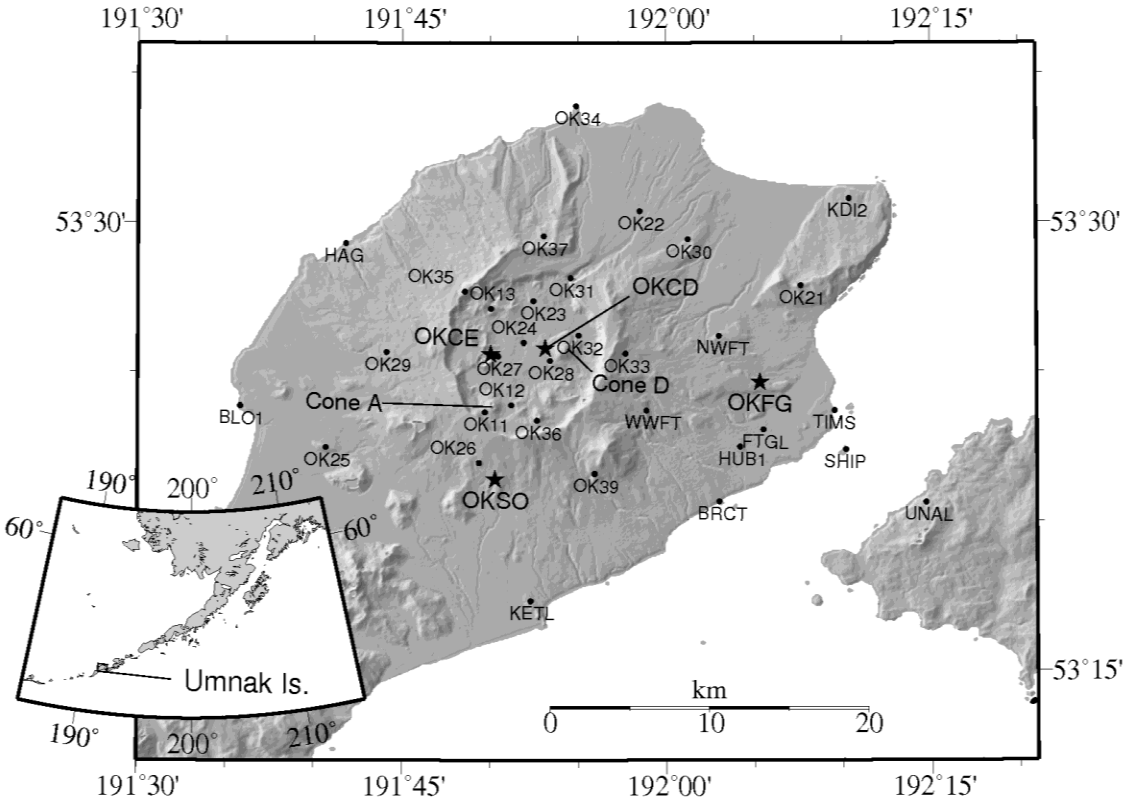

Figure 2.1: Map of Okmok GPS sites. The stars show the locations of the four CGPS instruments, the black dots show the locations of campaign benchmarks. Cone A, located in the southwest quadrant of the caldera, is the site of most historical eruptions. The 2008 eruptive activity originated near Cone D. The base map is a digital elevation model obtained from the Shuttle Radar Topography Mission.

Larson et al., 2001; McGuire and Segall, 2003; Fukuda et al., 2004] and dike propagation [*e.g. Ozawa et al., 2004*]. The linear Kalman filter has been the preferred method to solving time-dependent problems with noisy data, no doubt because it is easy to implement. *Segall and Matthews* [*1997*] used a linear Kalman filter along with a maximum likelihood method to determine optimal temporal and spatial smoothing hyper-parameters for the evolution of fault slip. The hyper-parameters determine how the model parameters, fault slip and slip velocity, change in time and space. This required the additional step of optimizing the smoothing-parameters by trying several values before running the optimal filter. As the number of smoothing hyper-parameters is increased this method quickly becomes untenable. *Fukuda et al.* [*2004*] developed a Monte Carlo Mixture Kalman Filter to optimize the smoothing parameters for a similar fault slip estimation problem. They included the extra benefit of temporally varying hyper-parameters which improved on some of the problems encountered by *Segall and Matthews* [*1997*] who used fixed hyper-parameters. The Monte Carlo method used to optimize the hyper-parameters reduced the computational time, but still required multiple implementations of the filter to converge on optimal parameter values. *McGuire and Segall* [*2003*] used an Extended Kalman Filter (EKF) to directly estimate the hyper-parameters along with the other linear model parameters. The EKF is a non-linear implementation of the Kalman Filter and requires linearizing the non-linear components of the model by Taylor series expansion. Linearization can cause biases in the transformation due to the violation of the assumption of local linearity. In a Kalman Filter small biases are amplified by the recursive nature of estimation, which can lead to divergence of the estimates. For the model presented by *McGuire and Segall* [*2003*] the only non-linear parameters were the hyper-parameters and parameters used to enforce non-negative fault slip, which simplifies implementation of the EKF. Directly estimating the hyper-parameters greatly reduces the computation time because the filter only needs to be run at most a few times and then only if initial parameter estimates are poor.

The method presented here differs from the EKF in one fundamental way. While the EKF tries to approximate a non-linear function with a linear function, the Unscented Kalman Filter (UKF) attempts to reproduce the distribution of a Gaussian random variable (GRV) that has been transformed by a non-linear function. To accomplish this, a minimal set of "points" are chosen to represent the distribution of the un-transformed GRV. These points are then passed through the true non-linear transformation and a new, transformed GRV is constructed from the distribution of the transformed points. A GRV is a variable that represents a population distribution with a mean and covariance. For some time now the UKF has been used in engineering applications, particularly in tracking problems and robotics [*Van Zandt, 2002*].

The application of this technique to geodetic data is demonstrated here and is then applied to GPS data collected at Okmok volcano. There are many Kalman filtering type strategies that may perform comparably to the UKF, but the UKF was chosen because of its performance record and the fact that existing codes can be easily adapted to operate in the algorithm. The UKF improves on the EKF in three ways, (1) the UKF provides higher order accuracy in the transformation, which often translates into better estimates than the EKF [e.g. *Wan and van der Merwe, 2001, Julier and Uhlmann, 2004, and Psiaki and Wada, 2007*], (2) partial derivatives do not need to be calculated, making model set up much simpler and (3) a *priori* information about model parameters is not required. Initialization of the UKF with model parameter estimates is required, but as discussed below, the ability of the UKF to converge on "true" parameter values even with poor initialization means that rigorous calculation of initial values is not necessary. The additional computational cost of the UKF, roughly 2 to 3 times that of a single run of the EKF [*Psiaki and Wada, 2007*], is not a significant setback in utilizing the UKF. The ability of the UKF to quickly determine model parameters and their uncertainties, whether the parameters are linear or not, makes this an ideal method to apply to deformation data where model geometry is changing or is unknown.

2.3 Methods

2.3.1 Unscented transformation

Here we demonstrate how an Unscented Kalman Filter (UKF) is used to estimate the state of a Mogi point source. The UKF provides a means of estimating temporal variations in nonlinear parameters, such as Mogi source position, while at the same time providing a reliable estimate of the covariance. We begin with an overview of the Unscented Transform (UT), which is crucial to the nonlinear estimation used in the UKF. Following that is a synopsis of how to incorporate the UT into a Kalman Filter to create the UKF. This explanation follows that of *Julier and Uhlmann* [*2004*] and *Wan and van der Merwe* [*2001*]. The symbols and notation used are summarized in Tables 2.1 and 2.2.

The UKF works in the same manner as the Kalman Filter except that it utilizes the UT to estimate the mean and covariance of the state parameters. The Kalman filter relies on a state-space formulation of the model. This formulation is described below, but for now it is sufficient to understand that the "state" is a vector containing all the model parameters for a given time. It is the state of the system at a certain time and if we know the state then we can predict the location of GPS benchmarks at that time.

The UT works by approximating a Gaussian random variable (GRV), as opposed to the common practice of approximating a nonlinear function with a linear one. The UT accomplishes this by choosing a set of points that matches exactly the GRV. Then the set of points are propagated through the non-linear transformation, g, and the transformed points are used to calculate a new transformed GRV. The function g may be any function, but in the case of volcano deformation g may represent the transformation from the amount of dike opening to GPS position. The transformed points are then used to calculate the post-transformation statistics. This special set of points, S, chosen to have mean θ and covariance $\boldsymbol{\Sigma}_{\theta}$, called *sigma points*, consists of L+1 vectors and associated weights, $S=\{s^{(i)}, W^{(i)}: i=0, 1, \ldots, L\}$. The size of the state dimension, L, determines how many points are required to reproduce the true mean and covariance of the GRV. The set of sigma points and weights are composed of vectors, $s^{(i)}$, with length equal to the

Table 2.1: Symbols used to represent time series modeling are shown along with a description of the parameter and any sub- and super-scripts used with the particular parameter. See Table 2.2 for a description of the sub- and super-scripts. The last three columns denote whether the symbol represents a scalar (s), vector (v) or matrix (m).

Description	Symbol	Sub-script	Super-script	s	v	m
Generic mean	Θ				×	
Generic covariance	$\boldsymbol{\Sigma}_{\theta}$					×
Sigma point	s		*(i)*		×	
Generic function	g			-	-	-
Transformed sigma point	z		$'$, *(i)*		×	
Sigma point weight	W	m, c	*(i)*	×		
Transformed generic mean	Θ				×	
Transformed generic covariance	$\boldsymbol{\Sigma}_{\Theta}$					×
Sum of state, process noise and observation noise dimensions	L			×		
Sigma point scaling hyper-parameter	K			×		
Sigma point scaling hyper-parameter	α			×		
Sigma point scaling hyper-parameter	κ			×		
Sigma point scaling hyper-parameter	β			×		
Observation matrix (function)	$\boldsymbol{H}$	$\boldsymbol{k}$				×
Transition matrix (function)	$\boldsymbol{F}$	$\boldsymbol{k+1,k}$				×
Observation noise	$\boldsymbol{v}$	$\boldsymbol{k}$			×	
Observation noise covariance	$\boldsymbol{R}$	$\boldsymbol{k}$				×
Observation noise mean	$\boldsymbol{\mu}$	$\boldsymbol{k}$			×	
Process noise	$\boldsymbol{w}$	$\boldsymbol{k}$			×	
Process noise covariance	$\boldsymbol{Q}$	$\boldsymbol{k}$				×
Process noise mean	$\boldsymbol{\eta}$	$\boldsymbol{k}$			×	
Data estimate	$\hat{\boldsymbol{y}}$	$\boldsymbol{k}$	_		×	
Data	$\boldsymbol{y}$	$\boldsymbol{k}$			×	
State mean estimate	$\hat{\boldsymbol{x}}$	0, $\boldsymbol{k}$, N	_, f, s		×	
State covariance	$\boldsymbol{P}$	0**,** $\boldsymbol{k}$**,** N**,** $\boldsymbol{yy}$**,** $\boldsymbol{xy}$	_, f, s			×
Kalman Gain	$\boldsymbol{K}$	$\boldsymbol{k}$				×
Identity matrix	$\boldsymbol{I}$					×
Smooth gain matrix	$\boldsymbol{A}$	$\boldsymbol{k}$				×
State sigma point	χ	$\boldsymbol{k}$	x, v, w, $'$		×	
Transformed sigma point (state → observation)	γ	$\boldsymbol{k}$	$'$		×	
Site position	p	$t,1,2$	*(j)*		×	
Regional velocity	v				×	
Time	t			×		
Reference frame translation	f	t			×	
Displacement from Mogi source	M	r,z			×	
Mogi source parameters	ε	t			×	
Random walk variance scaling hyper-parameter	λ	X,Y,Z,S			×	
Random walk noise value	ω	X,Y,Z,S			×	
Expectation operator	$E[\cdot]$			-	-	-

Table 2.2: Subscript and Superscript symbols are described with their meaning and use. The Parameters column indicates the parameters that use the particular sub/super-script and the final column shows which equations they are used in. See Table 2.1 for a description of the parameters

Description	Symbol		Parameters	Equations
	subscript	superscript		
Sigma point index		(i)	*W, s, z,* χ, γ	(1)-(5), (15), (16)
mean	*m*		*W*	(5), (15)
covariance	*c*		*W*	(5), (15), (16)
Pre-transformation covariance	θ		$\boldsymbol{\Sigma}$	-
Post-transformation covariance	Θ		$\boldsymbol{\Sigma}$	(4)
Post-transformation sigma point		´	z **,** χ, γ	(2), (3), (4), (15), (16)
Time index	***k***		-	(6)-(16)
Innovation covariance	***yy***		***P***	(15)
Cross covariance	***xy***		***P***	(15)
a priori estimate		$\bar{}$	***x***, ***P***, ***y***	(11), (12), (15), (16)
Forward filter estimate		f	***x***, ***P***	(12), (16)
Smoothed filter estimate		s	***x***, ***P***	(12), (16)
Time index; transition from ***k*** to ***k+1***	***k+1,k***		***F***	(8), (11), (12)
Initial; as in ***k***=0.	0		***x***, ***P***, *p*	(10), (17)
Final; as in ***k***=N.	***N***		***x***, ***P***	(12)
State sigma point		*x*	χ	(15)
Process noise sigma point		*w*	χ	(15)
Observation noise sigma point		*v*	χ	(15)
GPS station index		*(j)*	*p*	(17)
time	*t*		*p, f,* ε	(17), (20)
Mogi source position (x-component)	X		λ, ω	(20)
Mogi source position (y-component)	Y		λ, ω	(20)
Mogi source position (z-component)	Z		λ, ω	(20)
Mogi source volume change	S		λ, ω	(20)
Radial (displacement)	r		*M*	(18)
Vertical (displacement)	z		*M*	(19)
Transpose operator		T	-	-
Inverse operator		-1	-	-

dimension of the state parameter, paired with scalar weights, $W^{(i)}$. In the example given above of dike opening relating to GPS position, each $s^{(i)}$ would be a vector of length 1, but if we wanted to relate the full dike orientation to a position, then the length of each $s^{(i)}$ would be larger. In order to provide an unbiased estimate the weights, $W^{(i)}$, must follow the condition

$$\sum_{i=0}^{d} W^{(i)} = 1. \tag{2.1}$$

Each point, $s^{(i)}$, is propagated through the non-linear transformation to give the transformed sigma points

$$z'^{(i)} = g(s^{(i)}). \tag{2.2}$$

The mean of the transformed distribution is given by the weighted average of the transformed points,

$$\Theta = \sum_{i=0}^{d} W^{(i)} z'^{(i)}, \tag{2.3}$$

and the covariance of the transformed distribution is given by the weighted outer product of the transformed points,

$$\mathbf{\Sigma}_{\Theta} = \sum_{i=0}^{d} W^{(i)} (z'^{(i)} - \Theta)(z'^{(i)} - \Theta)^{\mathbf{T}}. \tag{2.4}$$

The transformed mean and covariance are denoted as, Θ and $\mathbf{\Sigma}_{\Theta}$, respectively. The conditions above, in equations 2.1-2.4, can be satisfied with the set of points and weights defined in equation 2.5 below. The sigma points lie on a hyper-sphere surrounding the state, with the radius of the sphere determined by the three hyper-parameters α, β, and κ. The values of the hyper-parameters are chosen based on the size (dimension) of the problem, and we adopt conventional values for these, discussed later.

Above, L+1 points are used to satisfy the conditions (2.1)-(2.4), this is the minimum number of points required to capture the true mean and covariance of the un-transformed distribution. We use 2L+1 points to improve the accuracy of the estimation of the transformed mean and covariance [*Wan and van der Merwe, 2001*]. The sigma points and weights are defined below, where W_m, and W_c are the mean and covariance weights,

$$\begin{aligned} s^{(0)} &= \theta \\ \mathrm{K} &= \alpha^2 (L+\kappa) - L \\ W_m^{(0)} &= \frac{\mathrm{K}}{(\mathrm{K}+L)} \\ W_c^{(0)} &= \frac{\mathrm{K}}{(\mathrm{K}+L)} + 1 - \alpha^2 + \beta \\ s^{(i)} &= \theta + \sqrt{(\alpha^2 (\mathrm{K}+L)\boldsymbol{\Sigma}_\theta)^{(i)}} \\ W_m^{(i)} &= W_c^{(i)} = \frac{1}{2(\mathrm{K}+L)} \\ s^{(i+L)} &= \theta - \sqrt{(\alpha^2 (\mathrm{K}+L)\boldsymbol{\Sigma}_\theta)^{(i)}} \\ W_m^{(i+L)} &= W_c^{(i+L)} = \frac{1}{2(\mathrm{K}+L)} \end{aligned} \tag{2.5}$$

where $\sqrt{(\alpha^2 (K+L)\boldsymbol{\Sigma}_\theta)^{(i)}}$ refers to the ith (i=1,2,…,L) column of the square root matrix (lower Cholesky factorization), and L is the sum of the state, process noise and observation noise dimensions. The weights $W_m^{(i)}$ and $W_c^{(i)}$ are used to calculate the mean and covariance, respectively, using equations (2.3) and (2.4). Both θ and $\boldsymbol{\Sigma}_\theta$ are formed by concatenating the mean and covariance of the state, process noise and observation noise respectfully. The set of sigma points given in equation (2.5) are not the only points that satisfy the conditions in eqs. (2.1)-(2.4), in fact other point sets can capture more information about the higher-order moments of the transformed points [*Julier and Uhlmann, 2004, appendix IV*], but equation (2.5) is sufficient for the task presented here.

The performance of the filter is optimized by choosing hyper-parameters that lead to the most efficient choice of sigma points. The hyper-parameters α and κ are used to scale

the distribution to remove unwanted effects [*Julier, 2002*]. Generally α is a small positive number ($10^{-4} \leq \alpha \leq 1$), and to make the sigma-point distribution radius independent of the state dimension it is set to $\alpha = \frac{1}{\sqrt{L}}$ [*Van Zandt, 2002*]. For small enough α, the performance of the UKF mimics that of the EKF. Usually κ is set to $\kappa = 3-L$ [*Wan and van der Merwe, 2001*] or $\kappa = L^2 - L/2$ [*Van Zandt, 2002*]. The latter guarantees non-negative weights, and is the value that we use in this study. The hyper-parameter β is chosen to incorporate prior knowledge of the state and error distribution. For Gaussian distributions, β=2 matches the 3rd order terms and minimizes the fourth order errors in the Taylor series expansion of the transformed covariance [*Julier and Uhlmann, 2004, appendix VI*], and we use this value.

The UKF is often compared to the extended Kalman Filter [*Wan and van der Merwe, 2001, Julier and Uhlmann, 2004*] where a non-linear process is linearized around an estimate by taking partial derivatives of the non-linear function at the estimate location. Approximating a non-linear function with a linear one is sometimes effective, especially for small changes in the parameter space, but this technique only provides first order accuracy of the transformation. First order accuracy is the result of the higher order terms being ignored due to the assumption that they contribute very little to the transformation. On some occasions this is a valid assumption, but often it can lead to divergence of the EKF due to the propagation of biases and inaccuracies in the covariance. It should also be noted that the UKF does not require derivative calculations and is therefore simpler to implement.

Monte Carlo techniques have some similarities with the UKF, mainly that a set of model parameters (states) are passed through the function and an estimate of the true state is obtained. The first and obvious difference is that Monte Carlo methods use random states to converge on an estimate, while the UT (or UKF) uses a determined set of states chosen to have particular properties. The UT also uses the minimum number of states, 2L+1 in this case, required to propagate the mean and covariance with third order

accuracy, while a Monte Carlo method may exceed the minimum many times over. Of course this does not mean that the UKF is computationally faster than any particular Monte Carlo method.

A simple demonstration, presented by *Julier and Uhlmann* [*2004*], highlights the advantages of the UT over linearization. The transformation from polar to Cartesian coordinates is an often used non-linear transformation. Consider a sensor that measures distance and azimuth to an object with measurement uncertainties of 2% and 15% respectively. Figure 2.2 shows a sample of measurements made by this sensor and the transformation of those measurements into Cartesian coordinates. Figure 2.2 also shows the transformation of the mean and covariance information by linearization and by the UT. Linearization produces a bias in the estimate and under predicts the covariance, which if used in an EKF may lead to divergence of the filter. The UT uses five points to represent the distribution and produces an unbiased estimate and a covariance estimate that is slightly larger than the "true" covariance calculated from the transformed sample distribution. The over estimate in the covariance arises from the fact the sigma points only capture third order accuracy, which is still an improvement over first order accuracy used in linearization. The improved performance of the UT over linearization is dependent on the transformation and will not always be so dramatic. For example, in the example above, if the azimuth is better constrained the results obtained by linearization are greatly improved. The advantage of the UT is that it uses the true non-linear function and provides third order accuracy, which means that it always provides results at least equivalent to results obtained by linearization.

2.3.2 Kalman Filtering

A Kalman Filter allows for the inclusion of process and observation noise in the system of equations that describe the model. This allows for time correlations in the observations to be processed in a meaningful way. The Kalman Filter has two general modes of operation, forward predictive and backward smoothing. In the predictive mode

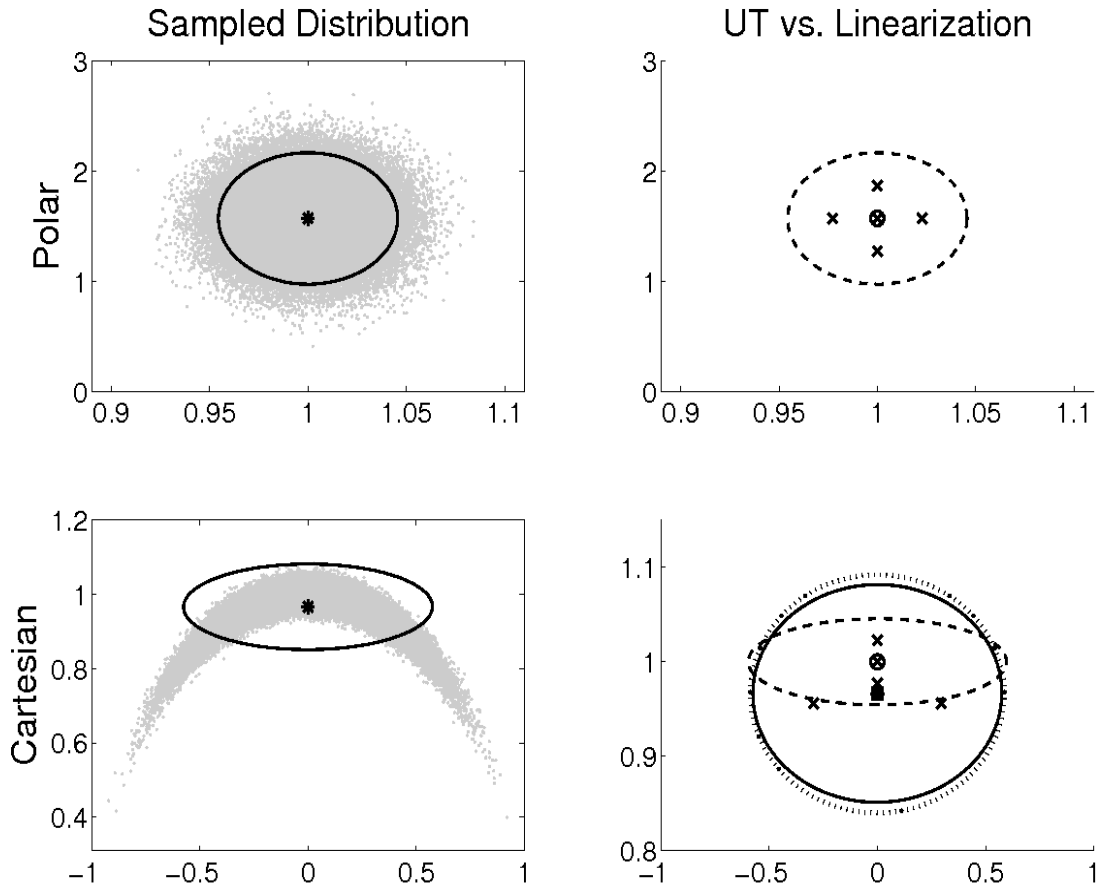

Figure 2.2: Polar to Cartesian coordinate transformation is shown by three different methods. On the left a random selection of points (gray dots) in the polar coordinate space is transformed through a non-linear function to Cartesian coordinate space. In both cases a mean and covariance can be calculated, black star and ellipse. On the right the same mean and covariance from the sample distribution is used in a linearized and unscented transformation. The three transformed results are shown in the bottom right pane: true mean and covariance (black star and ellipse), linearized transformed mean and covariance (circle and dashed ellipse), UT mean and covariance (square and dotted ellipse). Sigma points are shown as x's. In all cases the 1σ covariance ellipse is drawn.

all parameter estimates are based on past observations, while the smoothing mode incorporates all observations, past and future. The forward predictive mode of operation allows it to be used for real-time applications, providing the best estimate available now for constant or time-varying parameters. Outside of real time applications, we usually want to have estimates of time-varying parameters that are based on all available data, both before and after the time in question, and for this we need to include the backward smoothing step.

First we describe the forward and backward (smoother) Kalman Filter and then we incorporate the UT and arrive at the Unscented Kalman Filter (UKF) capable of predicting parameters associated with non-linear transformations. This formulation follows that of *Haykin* [*2001*] and is provided here for completeness.

The Kalman Filter works on the assumption that the process of interest can be described with a state-space model. The state-space formulation is very general and almost any process can be described with this set up. This type of model requires that the observation (data) estimates, $\hat{\boldsymbol{y}}$, can be predicted by a set of state parameters $\boldsymbol{x}$,

$$\hat{\boldsymbol{y}}_k = \boldsymbol{H}_k \boldsymbol{x}_k + \boldsymbol{v}_k , \tag{2.6}$$

where $\boldsymbol{H}$ is the referred to as the observation matrix and $\boldsymbol{v}$ is the observation noise. The mean and covariance of the noise source are,

$$\begin{aligned} \boldsymbol{E}[\boldsymbol{v}_k] &= \boldsymbol{\mu}_k \\ \boldsymbol{E}[\boldsymbol{v}_k \boldsymbol{v}_k^T] &= \boldsymbol{R}_k . \end{aligned} \tag{2.7}$$

The state evolves through time by means of a transition matrix $\boldsymbol{F}$,

$$\boldsymbol{x}_{k+1} = \boldsymbol{F}_{k+1,k} \boldsymbol{x}_k + \boldsymbol{w}_k . \tag{2.8}$$

The subscript k in the above equations refers to the time step, and the subscript of the transition matrix, $k+1,k$, indicates that $\boldsymbol{F}$ transforms the state $\boldsymbol{x}$ from time k to time $k+1$. The process noise, $\boldsymbol{w}$, is defined by a mean and covariance,

$$\begin{aligned} \boldsymbol{E}[\boldsymbol{v}_k] &= \boldsymbol{\eta}_k \\ \boldsymbol{E}[\boldsymbol{v}_k \boldsymbol{v}_k^T] &= \boldsymbol{Q}_k \end{aligned} . \tag{2.9}$$

With the model in the form described in equations 2.6- 2.9, the Kalman filter can be applied as follows. First, initial estimates of the state and the state covariance must be made.

$$\begin{aligned} \hat{\boldsymbol{x}}_0 &= \boldsymbol{E}[\boldsymbol{x}_0] \\ \boldsymbol{P}_0 &= \boldsymbol{E}[(\boldsymbol{x}_0 - \boldsymbol{E}[\boldsymbol{x}_0])(\boldsymbol{x}_0 - \boldsymbol{E}[\boldsymbol{x}_0])^T] \end{aligned} \tag{2.10}$$

For times beyond $k=0$ the state and covariance can be computed in the five steps shown below.

$$\begin{aligned} \text{State estimate propagation,} \quad & \hat{\boldsymbol{x}}_k^- = \boldsymbol{F}_{k,k-1}\hat{\boldsymbol{x}}_{k-1}; \\ \text{Covariance propagation,} \quad & \boldsymbol{P}_k^- = \boldsymbol{F}_{k,k-1}\boldsymbol{P}_{k-1}\boldsymbol{F}_{k,k-1}^T + \boldsymbol{Q}_{k-1}; \\ \text{Kalman gain matrix,} \quad & \boldsymbol{K}_k = \boldsymbol{P}_k^- \boldsymbol{H}_k^T [\boldsymbol{H}_k \boldsymbol{P}_k^- \boldsymbol{H}_k^T + \boldsymbol{R}_k]^{-1}; \\ \text{State estimate update,} \quad & \hat{\boldsymbol{x}}_k = \hat{\boldsymbol{x}}_k^- + \boldsymbol{K}_k(\boldsymbol{y}_k - \boldsymbol{H}_k \hat{\boldsymbol{x}}_k^-); \\ \text{Covariance update,} \quad & \boldsymbol{P}_k = (\boldsymbol{I} - \boldsymbol{K}_k \boldsymbol{H}_k)\, \boldsymbol{P}_k^-. \end{aligned} \tag{2.11}$$

In order to achieve the best estimate at any given time we must go back to all past times and incorporate the information gained from future observations. This in essence requires running the Kalman Filter backwards but in reality it is a bit simpler than that. The Rauch-Tung-Striebel (RTS) smoother [*Rauch et al.*, 1965] combines a backward pass of the Kalman Filter and a step that factors the backward and forward estimates into a smoothed estimate into single step. The RTS smoother only depends on the state mean and covariance estimates and the state transition matrix, which makes it straightforward to apply.

$$\begin{aligned} \text{Set the initial smoothed estimates,} \quad & \hat{\boldsymbol{x}}_N^s = \hat{\boldsymbol{x}}_N^f; \\ & \boldsymbol{P}_N^s = \boldsymbol{P}_N^f; \\ \text{Smoother gain matrix,} \quad & \boldsymbol{A}_k = \boldsymbol{P}_k^f \boldsymbol{F}_{k+1,k}^T [\boldsymbol{P}_{k+1}^{f-}]^{-1}; \\ \text{State estimate update,} \quad & \hat{\boldsymbol{x}}_k^s = \hat{\boldsymbol{x}}_k^f + \boldsymbol{A}_k(\hat{\boldsymbol{x}}_{k+1}^s - \hat{\boldsymbol{x}}_{k+1}^{f-}); \\ \text{Covariance update,} \quad & \boldsymbol{P}_k^s = \boldsymbol{P}_k^f + \boldsymbol{A}_k(\boldsymbol{P}_{k+1}^s - \boldsymbol{P}_{k+1}^{f-})\boldsymbol{A}_k^T. \end{aligned} \tag{2.12}$$

Where the superscript *f* refers to the estimates from the forward filter, s refers to the smoothed parameter estimates, and N is the final observation time. Applying the RTS

requires two steps, first a forward pass of the KF, equation 2.11, and then a backward pass, equation 2.12, to come up with a smoothed estimate that incorporates all the data.

We now have all the tools to apply a non-linear Kalman Filter and smoother using the UT. The state-space formulation of our model still looks like equations 2.6 and 2.8 but now instead of an explicitly linear function we have any arbitrary function,

$$y_k = H(x_k, v_k) \tag{2.13}$$

$$x_{k+1} = F(x_k, w_k) \tag{2.14}$$

We can form a sigma point set, χ, using equation 2.5 and then apply a modified set of KF equations that result from combining the procedure in equation 2.11 with the UT equations 2.3 and 2.4.

$$\begin{aligned}
\text{Sigma point propagation,} \quad & \chi'_k = F(\chi^x_{k-1}, \chi^w_{k-1}); \\
\textit{a priori} \text{ state,} \quad & \hat{x}_k^- = \sum_{i=0}^{2L} W_m^{(i)} \chi_k'^{(i)}; \\
\textit{a priori} \text{ covariance,} \quad & P_k^- = \sum_{i=0}^{2L} W_c^{(i)} (\chi_k'^{(i)} - \hat{x}_k^-)(\chi_k'^{(i)} - \hat{x}_k^-)^T; \\
\text{Observation propagation,} \quad & \gamma'_k = H(\chi'_k, \chi^v_{k-1}); \\
\textit{a priori} \text{ observation estimate,} \quad & \hat{y}_k^- = \sum_{i=0}^{2L} W_m^{(i)} \gamma_k'^{(i)}; \\
\text{Innovation covariance,} \quad & P_{yy} = \sum_{i=0}^{2L} W_c^{(i)} (\gamma_k'^{(i)} - \hat{y}_k^-)(\gamma_k'^{(i)} - \hat{y}_k^-)^T; \\
\text{Cross covariance,} \quad & P_{xy} = \sum_{i=0}^{2L} W_c^{(i)} (\chi_k'^{(i)} - \hat{x}_k^-)(\gamma_k'^{(i)} - \hat{y}_k^-)^T; \\
\text{Kalman gain matrix,} \quad & K_k = P_{xy}[P_{yy}]^{-1}; \\
\text{State estimate update,} \quad & \hat{x}_k = \hat{x}_k^- + K_k(y_k - \hat{y}_k^-); \\
\text{Covariance update,} \quad & P_k = P_k^- - K_k P_{yy} K_k^T.
\end{aligned} \tag{2.15}$$

This results in a forward or predictive UKF. This algorithm is provided in the Recursive Bayesian Estimation Library (ReBEL) toolkit for MATLAB® [*Van der Merwe et al., 2007*], which we use for all of our results. In order to obtain a non-linear smoother we can apply the same UT equations to the RTS smoothing procedure [*Psiaki and Wada,*

2007]. It should be noted though that if the state transition function, *F*, is linear then the RTS smoother in equation 2.12 can be used even if the observation function, *H*, is non-linear. The main advantage is that the computation time is significantly shorter for the linear smoother versus the sigma point or unscented smoother. Nevertheless in some cases the state transition function may be non-linear and the following smoother can be applied,

$$\begin{aligned} &\text{Smooth gain matrix,} && \boldsymbol{A_k} = \left[\sum_{i=0}^{2L} W_c^{(i)} (\chi_k^{(i)} - \hat{\boldsymbol{x}}_{\boldsymbol{k}}^{\boldsymbol{f}})(\chi_{k+1}^{-(i)} - \hat{\boldsymbol{x}}_{\boldsymbol{k+1}}^{-\boldsymbol{f}})^T\right] \boldsymbol{P}_{\boldsymbol{k+1}}^{-\boldsymbol{f}}; \\ &\text{State estimate update,} && \hat{\boldsymbol{x}}_{\boldsymbol{k}}^{\boldsymbol{s}} = \hat{\boldsymbol{x}}_{\boldsymbol{k}}^{\boldsymbol{f}} + \boldsymbol{A_k}(\hat{\boldsymbol{x}}_{\boldsymbol{k+1}}^{\boldsymbol{s}} - \hat{\boldsymbol{x}}_{\boldsymbol{k+1}}^{-\boldsymbol{f}}); \\ &\text{Covariance update,} && \boldsymbol{P}_{\boldsymbol{k}}^{\boldsymbol{s}} = \boldsymbol{P}_{\boldsymbol{k}}^{\boldsymbol{f}} + \boldsymbol{A_k}(\boldsymbol{P}_{\boldsymbol{k+1}}^{\boldsymbol{s}} - \boldsymbol{P}_{\boldsymbol{k+1}}^{-\boldsymbol{f}})\boldsymbol{A}_{\boldsymbol{k}}^{\boldsymbol{T}}. \end{aligned} \tag{2.16}$$

For a linear state transition function the smooth gain matrix, $\boldsymbol{A_k}$, reduces to the linear form of the matrix given in equation 2.12. Using the equation 2.16 for a problem with a linear state transition gives the exact results, except for deviations due to round off errors, as the standard RTS smoother.

For clarity above we distinguished between a forward filter and a smoother, but for the remainder of the paper all results are smoothed and we refer to the UKF or KF processes as including the smoothing step.

2.3.3 Modeling GPS data

The network of sites that we use lies in a region of convergence between the North American and Pacific plates, causing a regional scale tectonic signal. Often a reference station is used to remove common mode errors and any network wide tectonic signal that may mask the deformation source of interest, but depending on the observation history of the network, the network scale, and the tectonic environment, a reference station does not always provide a stable reference frame for analyzing observations. Instead of a reference station we use all sites to estimate regional velocity and reference frame translation terms, which together can be thought of as a pseudo-reference station. We apply the UKF to GPS positions in the International Terrestrial Reference Frame (ITRF).

Many studies have accounted for random benchmark motion with a random walk error term [e.g. *McGuire and Segall, 2003*; *Segall and Mathews, 1997*], but we do not attempt to estimate this error source. The large volcano related displacements tend to overwhelm any benchmark wobble. All of the deformation components in our model are spatially correlated, so it is unlikely that the spatially uncorrelated benchmark noise will be mapped into the model parameters to any significant degree. Most of the sites are surveyed, at best, once a year making it difficult to determine random motions of the benchmarks through long time gaps and survey related uncertainties.

Putting the components described above together, we write the position of a site *j* at any given time *t* as,

$$p_t^j = p_0^j + \mathrm{v}t + f_t + M(\varepsilon_t) \tag{2.17}$$

where p_0^j is the initial position of the site, v is the regional velocity, f_t is the reference frame translation, and $M(\varepsilon_t)$ is the deformation due to a Mogi source [*Mogi, 1958*] with parameters ε_t. For this small network we only use frame translations to approximate a reference frame transformation, assuming that the rotation and scale components of the transformation are close to zero. Equation 2.17 corresponds to *H* in the observation equation 2.13.

The Mogi parameters, ε_t, are the three dimensional location (*X, Y, Z*) and volume change (*S*) associated with the point source. The equations for the surface displacements caused by an isotropic point source are given by *Mogi* [*1958*],

$$M_r = C\frac{\sqrt{(p_1 - X)^2 + (p_2 - Y)^2}}{\left((p_1 - X)^2 + (p_2 - Y)^2 + Z^2\right)^{3/2}}, \tag{2.18}$$

$$M_z = C\frac{Z}{\left((p_1 - X)^2 + (p_2 - Y)^2 + Z^2\right)^{3/2}}, \tag{2.19}$$

where *X, Y, Z* is the source position and p_1 and p_2 are the *x, y* coordinates of the observation point. The radial and vertical displacements, M_r and M_z respectively, are transformed into Cartesian components for the purpose of comparison to the

observations. The coefficient in equations 2.18 and 2.19 is referred to as the source strength and can be written in terms of the volume change caused by displacement of the chamber walls, $S = 4\pi C/3$ [*Johnson, 1987*; *Delaney and McTigue, 1994*]. This volume change only represents the change associated with the deformation of the spherical chamber, but in the limiting case of an incompressible fluid this is also the volume of the fluid intrusion, a compressible fluid would result in a larger intrusion volume [*Johnson et al., 2000*].

The model should strictly constrain the Mogi source depth to be a positive number, and further it probably should even exclude certain shallow depth estimates, due to the break down of the point source assumption for shallow sources. For the examples shown here there was never a need to explicitly constrain the depth, although in some cases this may be required. Equations 2.17, 2.18 and 2.19 show that all the model parameters except the Mogi source location are linearly related to the observations.

We use the method of *McGuire and Segall* [*2003*] to represent the stochastic Mogi parameters,

$$\varepsilon_t = \lambda_{X,Y,Z,S}\omega_{X,Y,Z,S}, \tag{2.20}$$

where $\omega_{X,Y,Z,S}$ are four random walk noise values with variance $\sqrt{dt}$, corresponding to the four Mogi parameters. The hyper-parameters $\lambda_{X,Y,Z,S}$ control the temporal smoothness of the resulting Mogi parameter estimates. The hyper-parameters play the role of variances rather than weights, so for large values of $\lambda_{X,Y,Z,S}$ the parameters, ε, are allowed to change rapidly, while small values of the hyper-parameters result in temporally smoothed parameter values. The state vector is $x=[\omega_{X,Y,Z,S}\ f_{x,y,z}\ v_{x,y,z}\ p_{0x,y,z}^{\,j=1\ldots n}\ \lambda_{X,Y,Z,S}]$.

The state transition function, F, is the identity matrix with zeros along the diagonal corresponding to the reference frame translation terms. This is because the best estimate for the future state is the same as the current state except for the frame translation, which is always assumed to be independent from time to time

2.4 Data Simulations

Before we analyze the performance of the UKF we first must know what to expect for the parameter uncertainties based on the network geometry and uncertainties in the data. We use a "bootstrap" analysis to determine the expected confidence in estimating model parameters. A total of 10,000 simulations of Gaussian noise (σ = 3mm) are applied to the synthetic data constructed from a stationary inflationary source, and the noisy data are then inverted for the source parameters. This analysis shows the expected uncertainty for the model parameters in an idealized case. The example in Figure 2.3 uses the Okmok network geometry and gives a horizontal uncertainty of ±150m and a vertical uncertainty of ±250m for the location of the source. As expected, there is a clear trade-off between the depth and the strength of the source. This is the result of magnitude of surface deformation being matched either by a shallow weaker source or a deeper stronger source. The uncertainty in the volume estimate is ~0.5×10^6 m^3. There are more sources of uncertainty that are not accounted for, such as the heterogeneous elastic structure of the earth, and uncertainty in the true shape and force distribution of the source of deformation. It is difficult to assess how these uncertainties affect our ability to resolve the source parameters. The uncertainty estimates shown in Figure 2.3 are the best we can hope to achieve because real data are more difficult to characterize than this simulated case.

In order to ensure that the UKF can adequately estimate model parameters, a test case is used to demonstrate the filter performance. Simulated data containing realistic measurement errors are used to test the filter using the case of a moving source with a sinusoidal volume change history, which demonstrate the ability of the UKF to track changes in non-linear parameters. In the simulated scenario the source moves from a depth of 9km to 3.8km depth over a four year period and at the same time moves south westward for ~4km at a constant rate (Fig. 2.4A). During the four years the source changes from a deflationary source to an inflationary one (Fig. 2.4B). The synthetic data

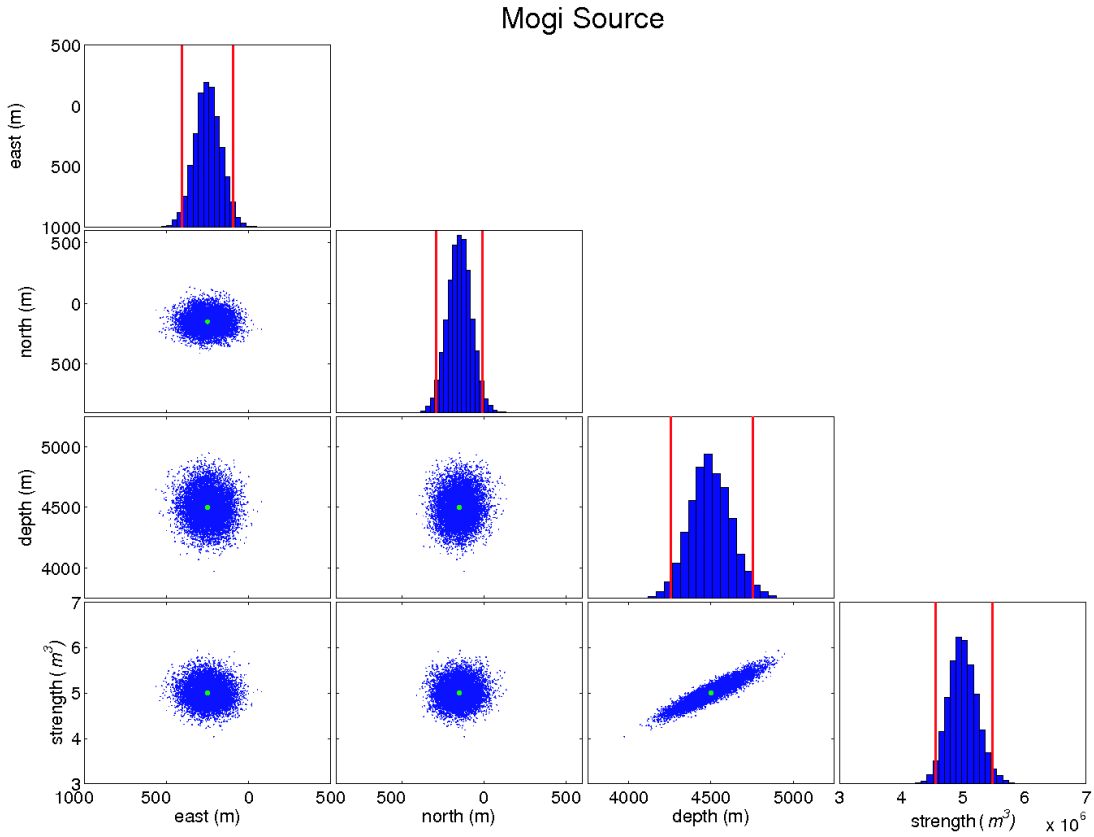

Figure 2.3: Bootstrap analysis is used to determine the expected uncertainty in model parameters. The site distribution of the Okmok network is used, along with noisy data from a Mogi model. Horizontal position is determined to ±150m, vertical to ±250m and the source strength has an uncertainty of $\pm 0.5 * 10^6$ m^3. The data are corrupted by white noise with a variance of 3 mm.

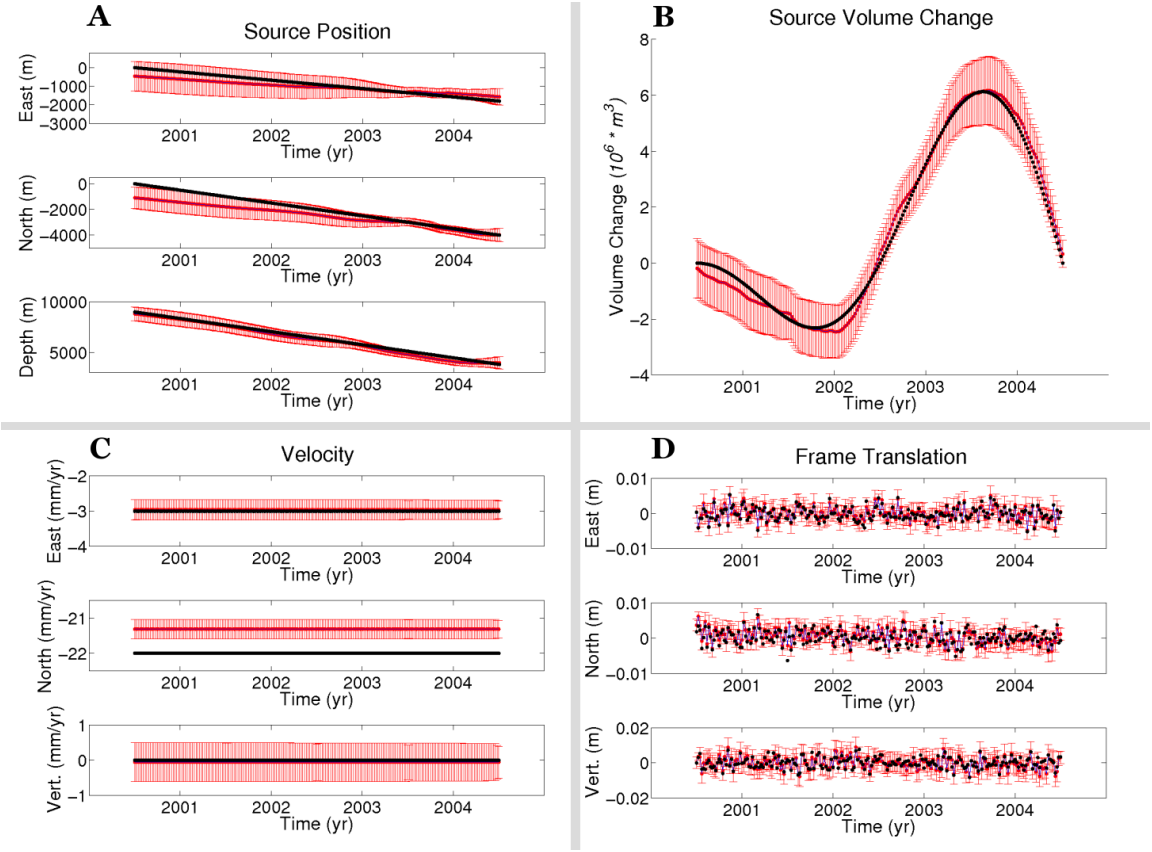

Figure 2.4: Filter results from synthetic data created from a moving Mogi source. In the simulation the source shallows and moves toward the southwest as indicated by the black lines Panel A. In each panel the black dots and lines represent the true values and the red dots show the model estimates and 2σ uncertainties. The filter was initialized at 0, 0 horizontal location, and 10km depth, which is close to the true location (black lines), but good results are obtained even if the initial horizontal position is displaced up to 10km horizontally and 5km vertically.

also include the effects of a constant regional tectonic velocity and random frame translational errors plus observation errors. The observation noise is chosen to mimic expected noise in GPS observations, that is σ_h=2mm and σ_v=4mm, for horizontal and vertical components respectively. We apply translational errors to mimic common mode error, σ_h=2mm and σ_v=3mm for horizontal and vertical components, respectively.

We generate synthetic weekly observations for the test using the GPS network at Okmok volcano (Fig. 2.1). Okmok has a widely distributed campaign network of 33 benchmarks and a sparse CGPS network of 4 instruments. A random selection of the campaign sites are "surveyed" once a year for as many as two weeks. The CGPS sites have data from every week during the 4 years of the simulation.

This simulation tests the ability of the filter to track changes in the source location as well as tests the ability of the filter to distinguish the trade-off between source volume change and depth. A wide aperture network should be able to reliably discern between a shallow weak source and a deeper stronger source, but if the network is sparse or poorly distributed the distinction between the two types of sources may not be easy. With a very sparse continuous network and a campaign network that is only observed once a year, the question becomes; can the filter distinguish the changes to the system? Movement of a pressurized point source may not be realistic but it does satisfy the goal of the exercise in providing a changing non-linear parameter. The movement of a pressure source may, to the first order, approximate slug flow in a conduit.

Best estimates are always found when using reliable initial estimates. The filter was initialized at the center of the local reference frame and at a depth of 10km, which is close to the true model values. The initial regional velocity is estimated from sites far from the volcano, in this case any site that is >10km from the center of the volcano. The velocity estimate obtained from the least-squares fit to the data from these sites is used as the initial estimate of the regional velocity and the uncertainty is used for the initial regional velocity covariance. Initial positions are determined from the first observation at the site and corrected with the regional velocity estimate.

Because it is hard to make an accurate initial estimate of the hyper-parameters, they are initially assigned large variance values. If the final estimate for these parameters is larger than 1σ from the starting value, the parameters are adjusted and the filter is re-run [*McGuire and Segall, 2003*]. Within a few iterations the hyper-parameters have converged to their final values.

The model parameter predictions are compared to the true model parameters in Figure 2.4. In almost all cases the true parameter values are within the estimated uncertainty of the parameter estimates. The most obvious instance where this is not the case is the north component of the regional velocity term (Fig. 2.4C). The UKF estimates ~21.3mm/yr southward motion, but the true motion is 22mm/yr. The difference is small, <1mm/yr, but it is significant. For the horizontal velocity components the uncertainty is ~±0.3mm/yr while the vertical component has a slightly larger uncertainty ~±0.5mm/yr, both of which are reasonable for long time series GPS records.

The position of the source is tracked reasonably well, but not perfectly. The uncertainty of each component of the source position varies in time, but generally falls in the range ±200-500m. The uncertainty bounds determined using the UKF are similar to what the bootstrap analysis suggests. The uncertainty in the source position is largest when the volcanic source produces the least amount of deformation, which is not a surprising result since the ability to locate the source is expected to improve with increasing signal-to-noise ratio.

Figure 2.5 shows the simulated CGPS observations (red) and the site position predictions from the filter results. By visual inspection it is clear the UKF does an adequate job predicting the site position, but there is some mismatch at the end of the time series in the north component, although the residual is less than the data uncertainty. The mismatch results from the under-prediction of the north component of the regional velocity (Fig. 2.4).

Although the initial estimates have some effect on the final results, the UKF is capable of finding “true” parameter values from poor initial estimates. This means that

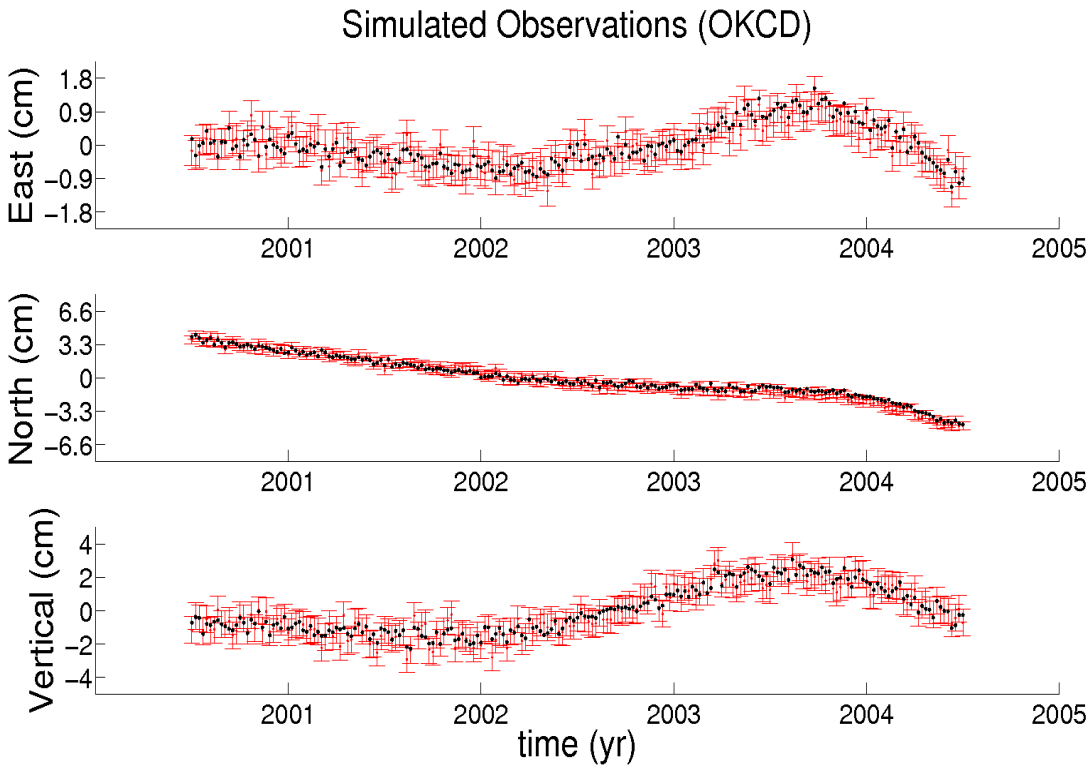

Figure 2.5: Simulated time series from site OKCD is shown in red and the station position estimate from the UKF is shown in black. There is very good agreement between the two, aside from a slight mismatch at the end of the time series in the north component. The disagreement is smaller than the data uncertainty and is the result of under-prediction of the north component of the regional velocity.

time does not need to be spent rigorously calculating *a priori* estimates of the state parameters. Tests were conducted to determine the effects of initial estimates on the filtered outcome. For this simulation, the initial horizontal position can be offset up to 10 km and the filter still recovers precise final position estimates. Likewise, when the depth is initialized at a 4 km offset from the true depth, the filter still gives a good estimate of the depth history. If both the depth and horizontal position are initially offset, the filter still recovers the true position. This highlights the need for caution when examining parameters that may have trade-offs with other parameters. These trade-offs can lead to reliable data estimates, but incorrect parameter values, which results in the inability to reliably assess the results without additional information and constraints. Although it is not explored in this study, the simple modification to the UKF proposed by *Perea et al.* [*2007*] may help the filter converge in these difficult instances.

If the filter estimates greatly differ from the initial values it is advisable to re-initialize the filter and re-estimate the parameter values. This increases the reliability of the UKF estimates by producing good estimates from the beginning of the time series to the end. The temporal correlation of the parameters means that bad estimates negatively affect other estimates nearby in time, so the best performance of the filter relies on good initial estimates.

2.5 Data

Campaign deployment of GPS instruments at Okmok began in the summer of 2000. Several reoccupations and expansions of the network have taken place since. In 2002 three continuous GPS instruments were installed at OKCE, OKCD and OKFG. Problems associated with file logging prevented complete records for the first year of operation. Sites OKCD and OKFG stopped logging during the year, and due to a configuration problem OKCE logged for only one hour per day. To improve results from the sparse phase data that were recorded during that year, we employ ambiguity resolution [*Blewitt, 1989*] using the Okmok network, sites located on nearby Akutan Volcano, and a few sites located on stable North America in the conterminous United States. In 2004 a

fourth continuous site, OKSO, was added to the network. The history of observations at each site is displayed in Figure 2.6.

Excluding the date range mentioned above the GPS data are processed in daily solutions using GIPSY-OASIS [*Zumberge et al., 1997*] release GOA4, in network mode, incorporating data from all GPS sites in and around Alaska, with ALGO as a reference clock. Elevation-dependent phase center models (IGS01) for each of the individual antennas are applied with a 10° elevation mask [*NOAA, 2008*]. The TPXO.2 ocean tidal model is used, and wet tropospheric path delays are estimated using the Niell mapping function [*Niell, 1996*].

There are a total of 37 GPS sites with multiple observations over a total span of more than seven years. The deformation signal does not have significant changes on timescales shorter than a week, so we use weekly averaged positions. This reduces the number of time-steps the UKF takes from nearly 1800 to 257, providing a reduction in CPU time without compromising any information in the data.

Figure 2.7 shows a few sample time series plots of the weekly averaged positions. All of the CGPS station time series are shown along with observations from a few campaign stations. During the first year of operation the positions for OKCE are determined with only one hour of data, resulting in a larger position variance, which is most evident in the vertical component. The two intra-caldera CGPS sites, OKCE and OKCD, clearly show two inflation periods, one following the other, between 2003 and 2005. The campaign sites inside the caldera, OK24 and OK12, on the other hand, suggest one extended period of inflation lasting from 2002 to 2005. Comparing these time series it is clear how even a few CGPS sites can contribute a view of the deformation history that is not possible with campaign sites alone. Sites OK30 and OK33 are examples of what the typical extra-caldera surveys look like. There are often gaps in the time series when a survey could not be conducted due to time or weather constraints (Fig. 2.6).

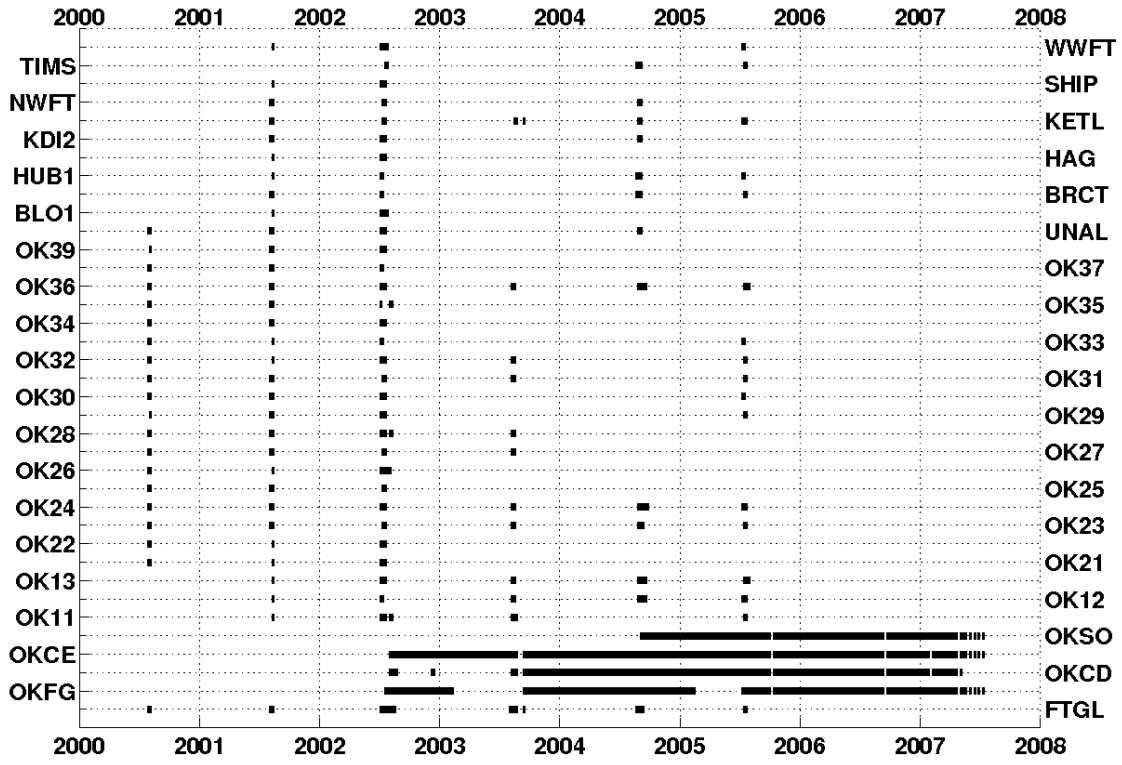

Figure 2.6: The observation times at each site in the network for the duration of the study are represented as a black bar on the time line. Gaps in the time line occur when there is more than one week without observations at that site.

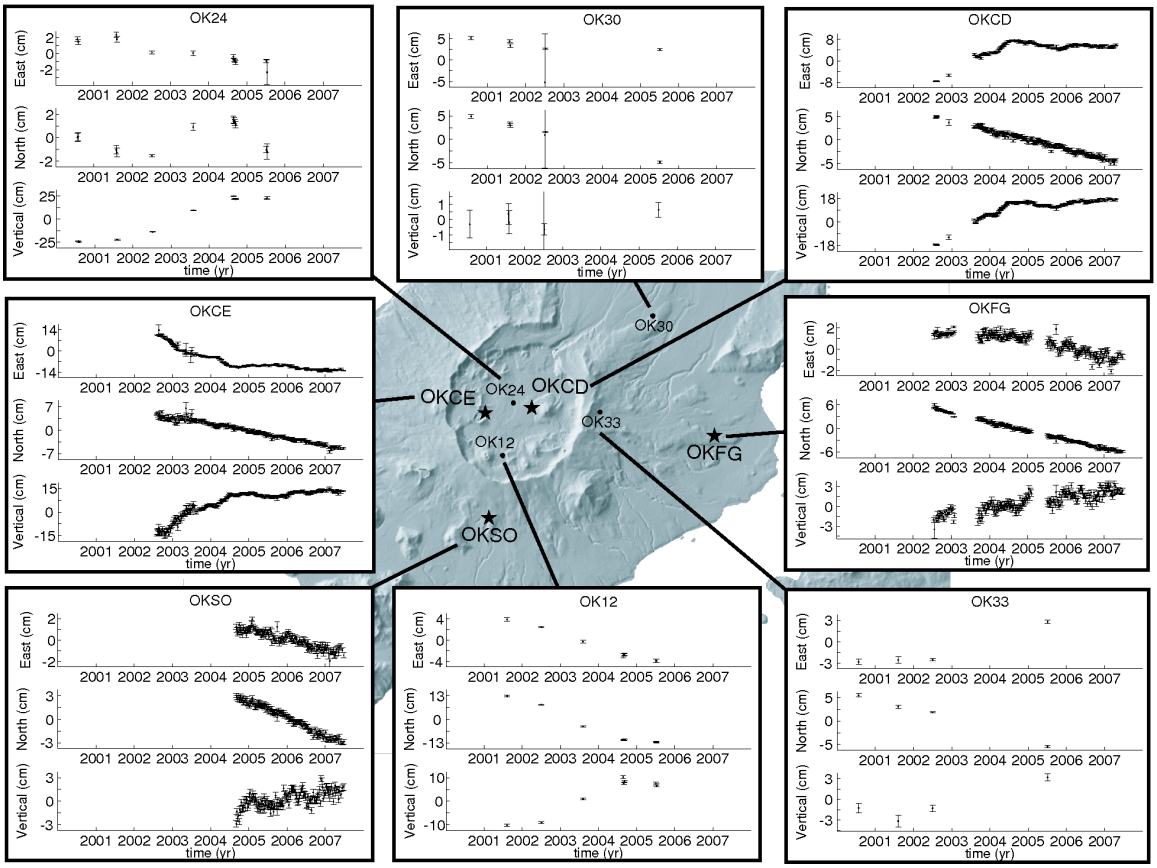

Figure 2.7: Examples of time series from select sites are shown along with the site locations on the volcano. The two intra-caldera CGPS sites, OKCD and OKCE, show inflation pulses that occurred in 2003 and 2004. Site OK24 recorded the largest vertical displacement, ~50cm. The time series are shown in the ITRF and the ~2cm/yr southwestward regional velocity (Table 2.3) is apparent particularly at stations OKSO and OKFG.

2.6 Results

We use the varying depth method of *Williams and Wadge* [*1998*] to account for topographic effects. The site elevation is added to the source depth when calculating the vertical deformation, but the horizontal deformation is determined using the mean elevation of the network. The depth determined by this method is the depth below sea-level.

Previous InSAR and GPS studies at Okmok locate a deformation source beneath the center of the volcano at 3km depth [*Lu et al., 2005*; *Miyagi et al., 2004*]. We initialize our point source at this approximate location with uncertainties on the order of several kilometers in the horizontal and vertical position. Any volcano deformation that occurred prior to the first GPS observation has no consequence to the results obtained here, so we assume that the initial source strength is zero.

There is a trade-off between the initial site position parameters and the initial estimate of the Mogi strength. This trade-off causes the estimates for the initial position to be adjusted away from or toward the volcano, consistent with displacements from a Mogi source. Although the cumulative effect should be negligible (initial position estimate + initial Mogi displacement = true initial position), it is not desirable to have an offset for the initial position estimate nor to have volcanic deformation before the temporal record begins. We get around this trade-off by setting the initial position variance to a small value for all the sites that were surveyed in 2000. Sites that were established after the first campaign have larger variances reflecting the time between the first observation at the site and the reference time, July 2000.

The results from the best-fitting freely moving and fixed source models are shown in Figures 2.8 and 2.9, respectively. The parameter estimates in both cases are very similar; however the fixed source model has a lower reduced-chi-squared value, so the discussion focuses on those results. We calculate reduced-chi-squared as $\frac{1}{dof}\sum_{k=1}^{N} r_k^T \boldsymbol{R}_k^{-1} r_k$; *dof* represents the degrees of freedom, and r_k is the residual vector for the k^{th} epoch.

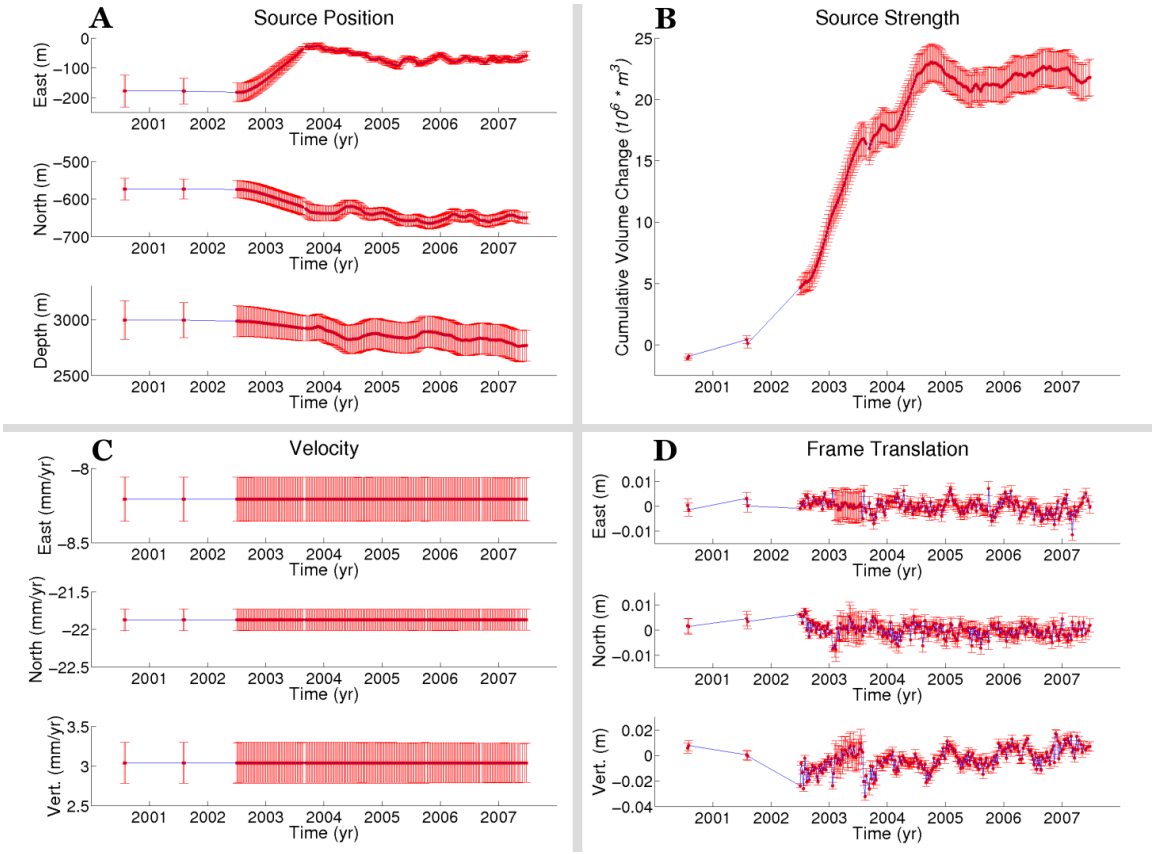

Figure 2.8: Results from the best fitting freely moving Mogi model are similar to the fixed position model (Figure 2.9). The discussion focuses on the fixed position model because it provides a better fit to the data. Panels show A, source position, B, source strength, C, tectonic velocity, D, reference frame error. All parameters are assumed to vary with time except for tectonic velocity, which is assumed to be constant in time. Reference frame errors are uncorrelated from time to time, while other parameters are assumed to vary smoothly with time.

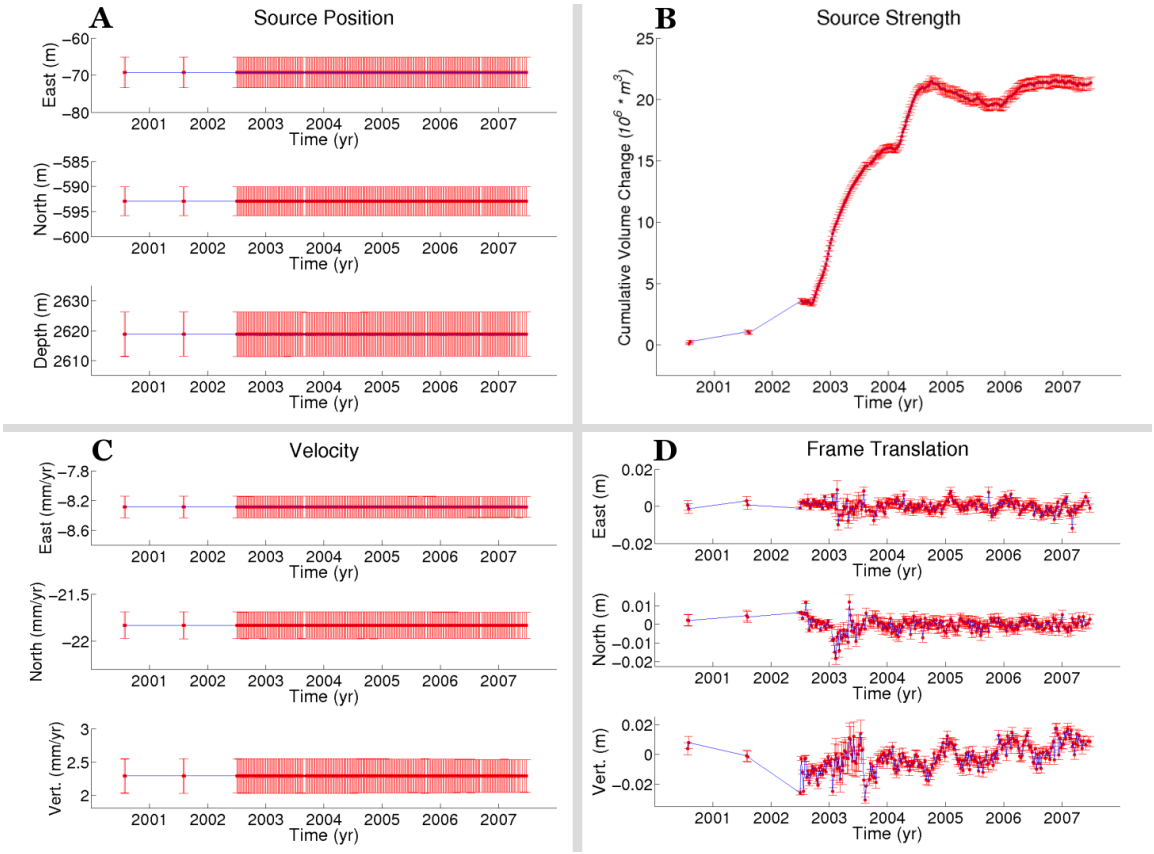

Figure 2.9: Results from the best fitting fixed position model, show the best position estimate to be at 70 m west, 590 m south (53.4330º N , 168.1400º W) of the caldera center and 2.6 km below sea level. Panels are the same as in Figure 2.8. The source strength is assumed to vary with time, while the tectonic velocity and source position are assumed to be constant in time. Reference frame errors are uncorrelated from time to time.

The other symbols are the same as previously used and described in Table 2.1 and 2.2. The number of free parameters is the number of all the time-invariant parameters plus the number of the time-variable parameters multiplied by the number of time steps. The degrees of freedom is the total number of data minus the number of free parameters. Note that in Figure 2.9, the source position is still estimated, but it does not move with time. Figure 2.8 (panel A) shows some apparent movement of the source, within a range of about 200m. If this is real it likely reflects different regions of the magma chamber being active at different times. The estimated movement, however, is about equal to the uncertainty obtained from bootstrap analysis (Figure 2.3) for those parameters. For this reason we do not think that it is possible to confidently distinguish separate active source regions.

The cumulative Mogi volume change history (Fig. 2.9, panel B) emphasizes the inflationary period that the volcano has been in since the 1997 eruption [*Lu et al., 2005; Miyagi et al., 2004*]. Two rapid inflation pulses stand out; the first begins in the summer of 2002 and lasts until late 2003, and the second begins in the spring of 2004 and lasts until the summer of that year. There is an extended period of deflation following the second rapid inflation period, in 2004-2005, with a volume loss of $1.8 \pm 0.5 * 10^6$ m^3. This volume was entirely recovered during the winter of 2005-2006. Since then the volume has remained stable with a slight loss in mid-2007. Uncertainty in the source strength is roughly $\pm 0.2 * 10^6$ m^3, which agrees very well with the bootstrap analysis.

Figure 2.9, Panel A shows the Mogi position estimates. The position is 70 m west and 590 m south of the caldera center and 2.6 km below sea level, which puts the surface projection of the point source at 53.4330º N and 168.1400º W. The UKF estimates the Mogi position uncertainty to be less than ±5m, which, although encouraging, is probably far too optimistic.

The accuracy of the network velocity estimate (Fig. 2.9C) is assessed by comparing it to the predicted North America velocity at the center of the network. Table 2.3 shows the Okmok network velocity estimated from the UKF and the North America velocity

from the *Sella et al.,* [*2007*] model, as well as the difference. The difference in the east and vertical components is small, but significant. There may be additional sources of network wide deformation caused by the convergence of the Pacific plate, or interseismic strain from the subduction zone. The orientation of the trench and direction of convergence are roughly perpendicular in this region, causing motion directed toward ~335° east of north. Southwest directed motion of the arc has been measured farther to the west near the Andreanof Islands, by *Cross and Freymueller* [*2007*] and also to the east along the Alaska Peninsula by *Fournier and Freymueller* [*2007*]. Okmok is situated in a part of the Aleutian arc that should lie on the Bering plate, according to *Cross and Freymueller* [*2008*]. They suggest a southward motion relative to North America due to Bering plate rotation. Together, plate convergence, Bering plate rotation and interseismic strain may be able to account for the residual westward and vertical motion observed by the Okmok network. If the combination of the Bering plate and North America rotation is subtracted from the velocity estimated at Okmok, then the residual velocity is directed at ~320°, nearly identical to the convergence direction. Further work needs to be done to untangle the tectonic details in this region, but the velocity determined by the UKF is an accurate estimate of the regional motion.

The reference frame adjustments are shown in Figure 2.9, Panel D. The accuracy of the reference frame estimates can be assessed by comparing the position estimates to the observations. Figure 2.10 shows a subset of the CGPS time series, taken from a time period when the volcanic signal was small. Site OKCD and OKCE have a moderate component of volcano related deformation during this time frame, particularly from late 2005 to early 2006, but this component is very small at OKSO and OKFG. Nevertheless, common mode error can be seen in the observations at all the stations (particularly the vertical component), and the position estimates show how the reference frame correction effectively characterizes that error. The time series shown in Figure 2.10 have the secular velocity of the Okmok network removed.

Table 2.3: Okmok network velocity compared to North America velocity.

	Okmok (mm/yr)	North America *Sella et al.* (mm/yr)	Difference (mm/yr)	Bering Plate *Cross et al.* (mm/yr)
East	-8.3 ± 0.2	-3.3 ± 0.1	-5.0	-1.4
North	-21.8 ± 0.2	-21.5 ± 0.2	-0.3	-4.7
Vertical	2.3 ± 0.3	-0. 1 ± 0.01	2.3	0

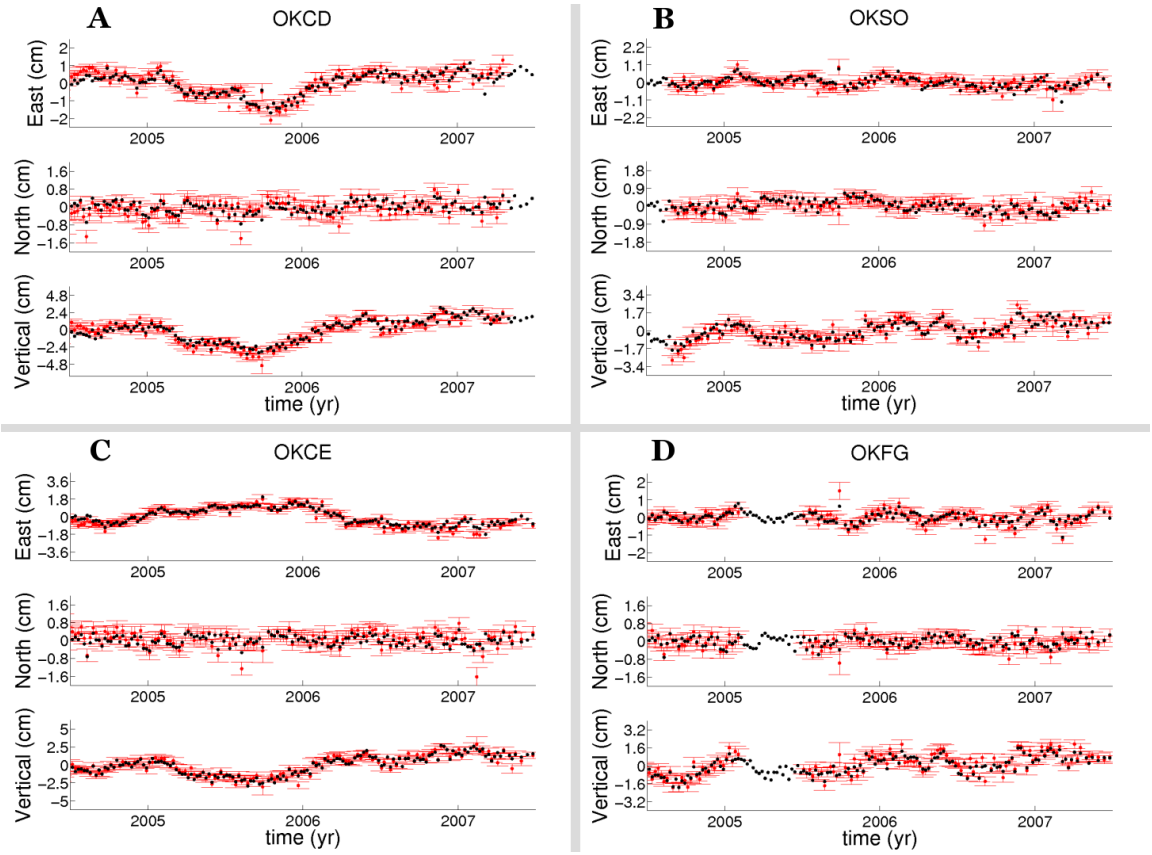

Figure 2.10: Time series at the four continuous sites are shown with the position estimates from the fixed source model. Red crosses and error bars show GPS observations and uncertainties. Black dots are position estimates from a fixed source model (Figure 2.9). The common mode error is successfully accounted for by the reference frame correction term that allows for network wide position adjustments. The network velocity determined by the UKF (Table 2.3) has been removed from the time series.

The residual maps in Figure 2.11 show the temporal and spatial distribution of residuals around each site location. For most of the sites the residuals cluster within 1 cm of zero, and for sites with large displacements the largest residuals are <10% of the deformation signal. The map can highlight specific regions where the model is misfitting the data or time periods when the model does not correctly describe the site motion. There are no areas or times that stand out with a consistent pattern of misfit, but the sites inside the caldera do show some systematic residuals. Those residuals suggest that a more complex source model or the heterogeneous structure of the volcano may need to be considered to account for the discrepancies.

Figure 2.12 shows the residuals from the stations shown in Figure 2.7. The displacements at all sites have been greatly reduced, but some residual signal still remains, particularly at the intra-caldera stations. This is most obvious at OKCE which has the longest continuous record. At that site the residuals start off ~2.5 cm to the south of the site and migrate northward, correlated with the first inflation pulse, until mid-2003 when they center on the site and remain for the rest of the time series. The volcanic signal at the site is almost exclusively in the east component (Fig. 2.7), the north component residuals, therefore, reflect error in the source geometry and/or location. The opposite sense of residuals on the north component at OKCD suggests that the simplification of the source geometry is the likely source of the problem. That is, a change in location of the Mogi source cannot fully account for the residual motion at these two sites, but a non-spherical or non-point source might. Like OKCE, almost all of the volcanic deformation seen at OKCD occurred in the east component.

Site OK24 is the closest station to the deformation source; therefore it has the largest vertical displacement, ~50cm. The model under-predicts the amount of vertical deformation at this site by a several centimeters (Fig. 2.12). At OK12 the vertical deformation is slightly over-estimated. At site OK13, on the north side of the caldera, roughly equal distance from the deformation source as OK12, the vertical deformation is matched very well. This suggests that a finite dimensional and probably asymmetric

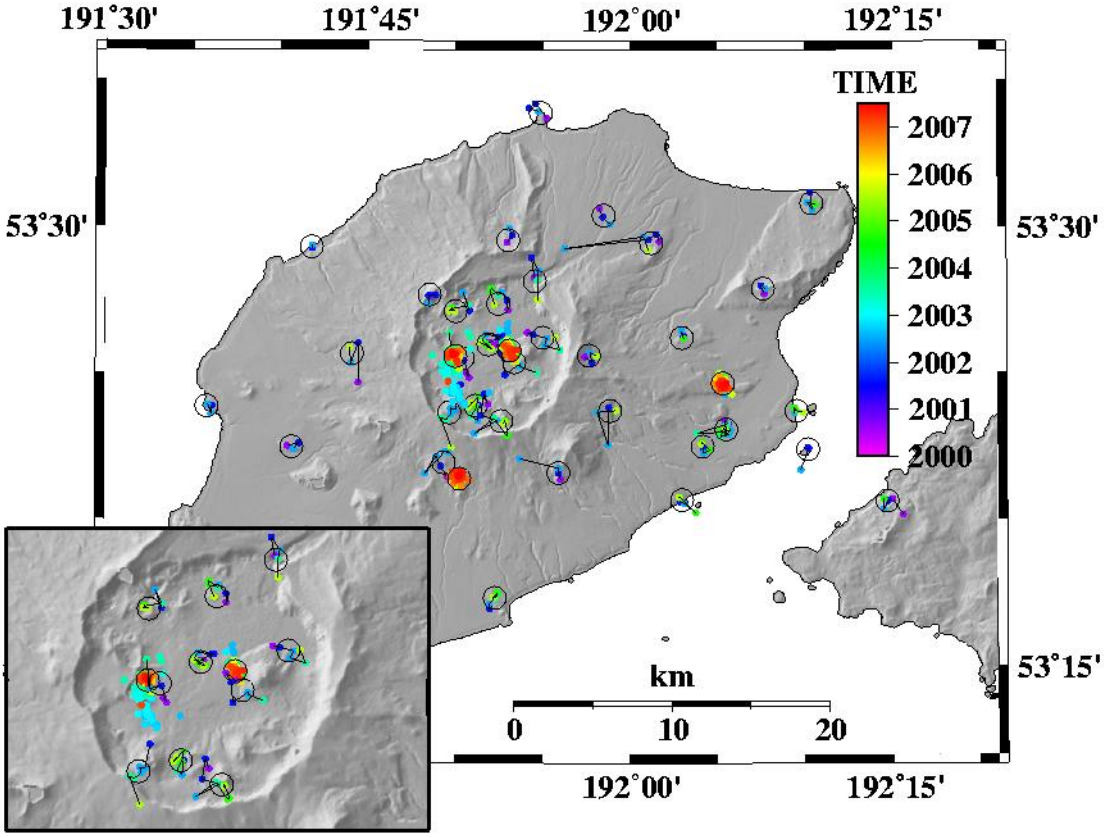

Figure 2.11a: The horizontal residual map shows each residual as a colored dot, where the color corresponds to the time of the observation. Open circles at each site represent 1 cm radial distance from the site. Campaign site residuals have a line connecting each residual to aid in associating each dot with the proper site.

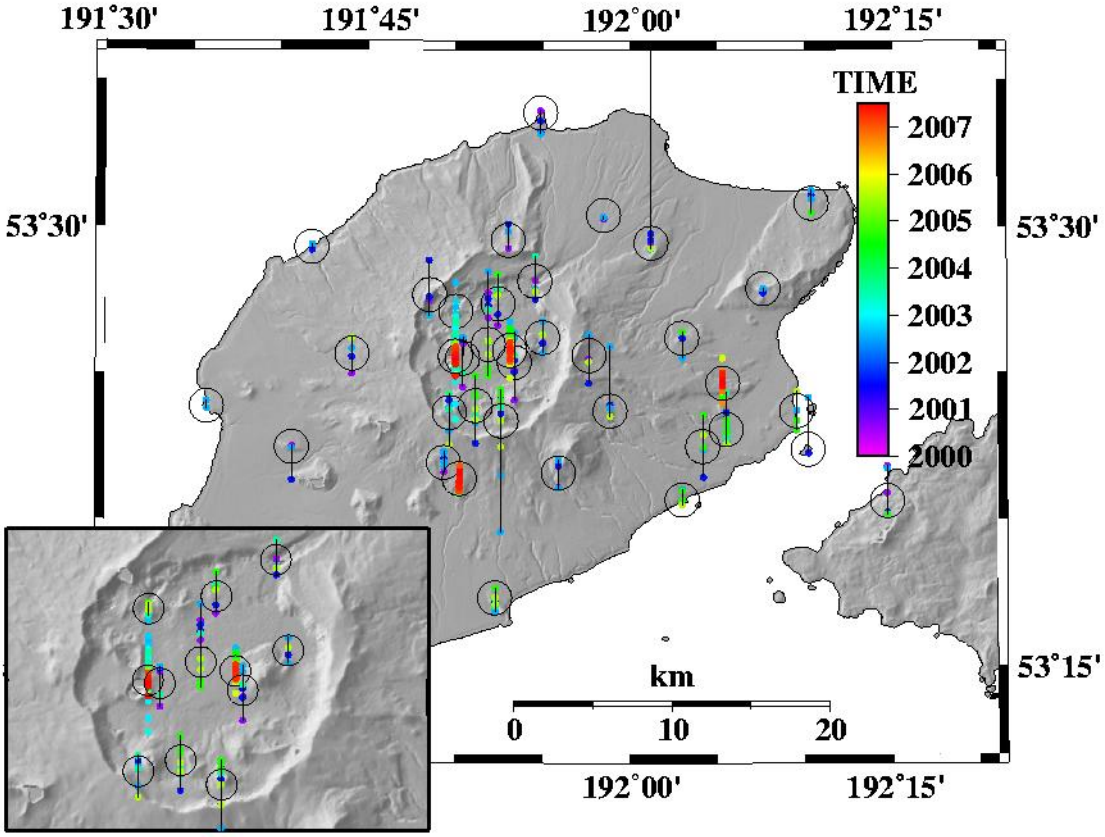

Figure 2.11b: The vertical residual map shows the vertical residuals at each site (similar to Fig. 2.11a). Each open circle represents a 2 cm radius centered on each site. The north-south alignment of residuals corresponds to positive and negative residuals respectively.

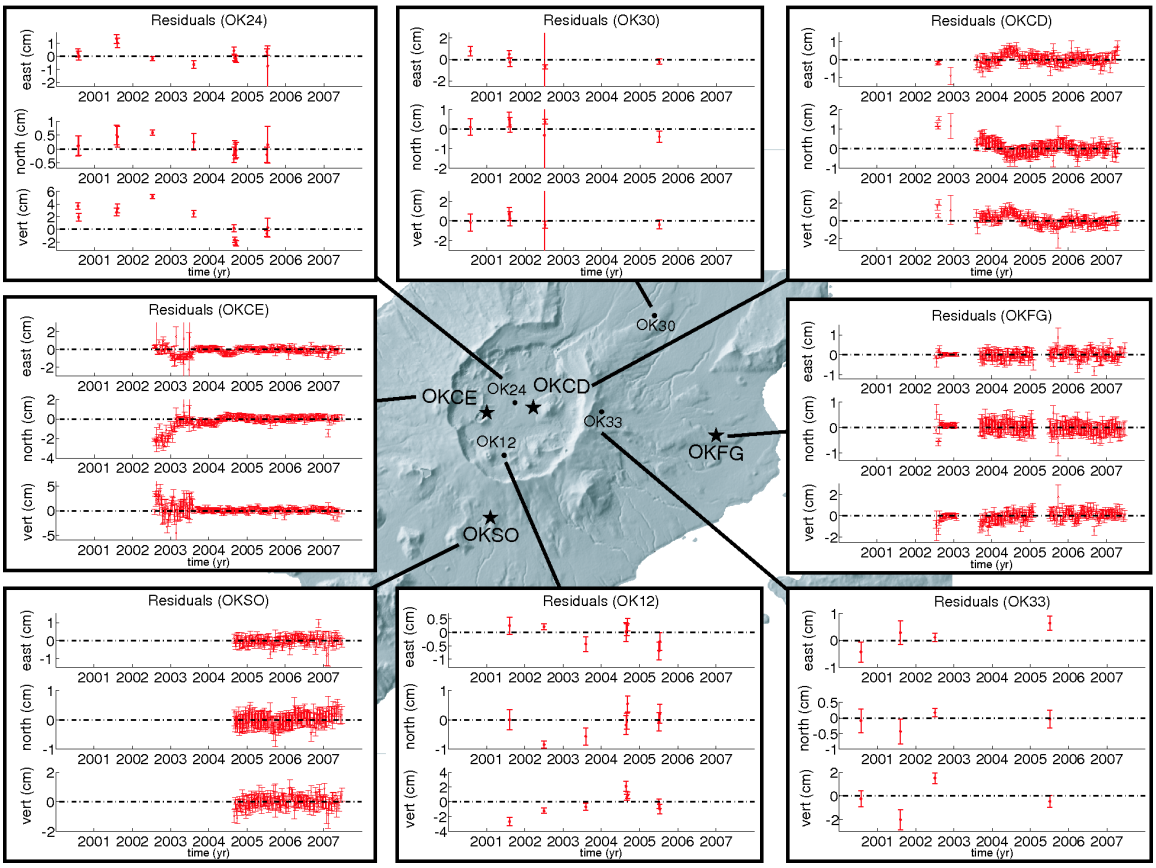

Figure 2.12: Examples of residuals from the sites shown in Fig. 2.7 are shown, along with the site locations on the volcano. Systematic errors are evident in the north component of both OKCE and OKCD. The model under-estimates the vertical deformation at OK24 by ~10%. The vertical deformation is over-estimated at OK12.

source is required to match at least some of these inconsistencies. See the supplemental material for residuals from all sites.

2.7 Discussion

We compare the results obtained here with the overlapping InSAR data (2000-2003) from *Lu et al.* [*2005*]. The rate of volume change and the cumulative volume change are shown in Figure 2.13. We used the UKF to solve for cumulative volume change at the source while *Lu et al.* [*2005*] solved for the volume flux. We calculate the flux by dividing the monthly (yearly for 2000-2002) volume change by the time span. Using a shorter time interval to calculate the flux introduces high frequency fluctuations that are within the uncertainty of the volume estimates. From the GPS there are three distinct inflation pulses (Fig. 2.13) and one deflation period. There is good agreement between both the InSAR and GPS derived flux and volume change. There is a slight disagreement between the fluxes in 2003, but this is a consequence of the long-term average that InSAR observes compared to the short-term fluctuations that are captured by the GPS. This is confirmed in the cumulative volume plot where, within the uncertainty, the cumulative volume is in agreement between the two methods. Since there is no baseline for the cumulative volume, the two sets of estimates are aligned so that there is minimal difference between the overlapping estimates in 2000 and 2001. The volume recovery can be compared to the loss associated with the 1997 eruption, $4.7 \pm 0.5*10^7$ m^3, calculated from InSAR [*Lu et al., 2005*]. For both the eruption volume and the post-eruption refilling, we are comparing the volume change of Mogi point sources fit to geodetic data, so we expect the values to be comparable no matter what biases or uncertainties may be introduced by using a simplified model. Since 2000 when GPS receivers were first deployed on Okmok a total volume increase of $\sim 2.1 \pm 0.05*10^7$ m^3 has occurred, assuming incompressible magma. Including observations from InSAR going back to 1998 (Figure 2.13) [*Lu et al., 2005*] the total volume change is $\sim 3.3*10^7$ m^3, or between 60% and 80% recovery of the volume lost during the 1997 eruption.

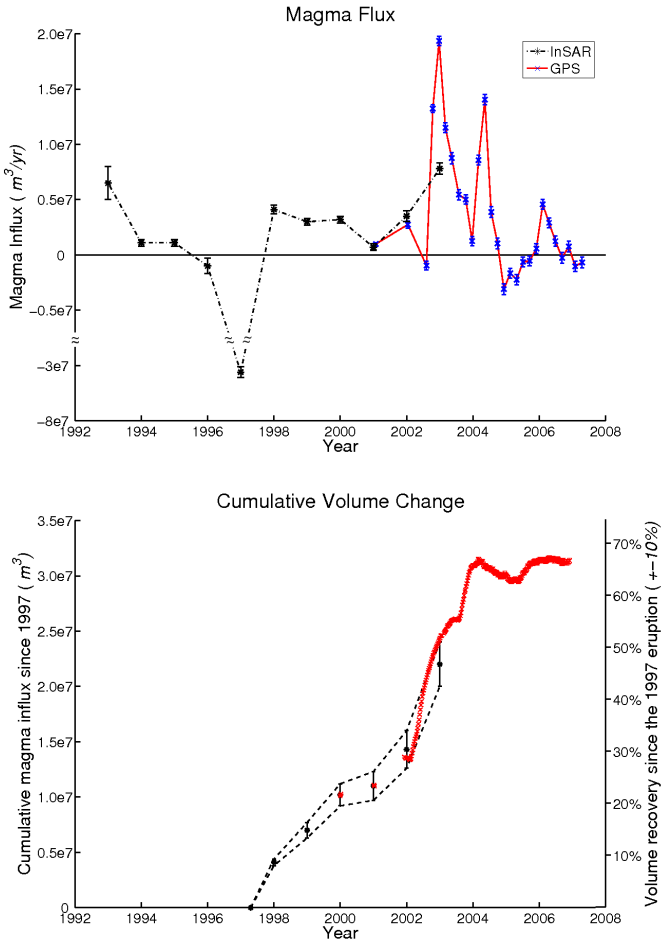

Figure 2.13: The rate of volume change and the cumulative volume change estimated from GPS are shown along with the results from InSAR. The top panel shows the rate of volume change from InSAR (black) and GPS (blue). There is good agreement in the rates for the years 2000 and 2001. The discrepancy in 2003 can be attributed to poor temporal sampling of InSAR which only shows the yearly averaged rate. The horizontal line distinguishes inflation (above) from deflation (below). The bottom panel shows the total volume change estimated from InSAR (black) since the 1997 eruption with the volume change estimates form GPS (red) overlying. The total volume recovered is ~60% - 80% of the volume lost during the 1997 eruption. (Modified from *Lu et al.* [*2005*], Fig. 9)

Recent volcanism at Okmok has originated from vents inside the caldera. The vents form a ring inside the caldera scarp with a radius of approximately 3-4km. Cone A, located in the southwest sector of the caldera (Fig. 2.1) has hosted all, except the most recent, eruptions at Okmok in the last century. Any intra-caldera eruption will likely fall along this ring of vents, which means that in order to reach the surface the magma needs to ascend ~3km vertically and traverse ~3km horizontally. This is most likely accommodated by dipping dikes or conduits established along conical fractures. Depending on the size of the melt storage region, the pathways have a dip not shallower than ~45° and maybe as steep as 90°. *Mann et al.* [*2002*] proposed a horizontally traversing pathway, based on a shallow deflationary signal along the path from the caldera center to Cone A. The signal is likely associated with the contracting 1958 lava flow [*Lu et al., 2005*], and the most likely path that magma travels during an eruption is a direct path from the reservoir to the surface (Fig. 2.14).

A schematic of the shallow magmatic system at Okmok is shown in Figure 2.14. The plumbing system consists of a central magma storage region, corresponding to the Mogi source of the deformation studies. Magma makes its way to the surface along ring fractures inside the caldera. *Finney et al.* [*2008*] suggest a relatively small chamber is insulated from the country rock by crystal accumulation along the margins of the chamber. There is evidence that the crystal margin undergoes hydrothermal alteration by meteoric water [*Finney et al., 2008*]. The caldera fill is likely highly fractured rock and pyroclasitic sediment.

The relatively long lived deformation source at ~3km beneath the caldera suggests a shallow melt storage region. InSAR observation that span the 1997 eruption and estimates of the lava flow volume confirm that the amount of volume withdrawn from this reservoir is approximately equal to the flow volume, assuming 25% porosity of the lava flow [*Lu et al., 2003a*]. This indicates that a majority of the melt existed in the shallow reservoir prior to eruption, as opposed to coming from depth and passing through

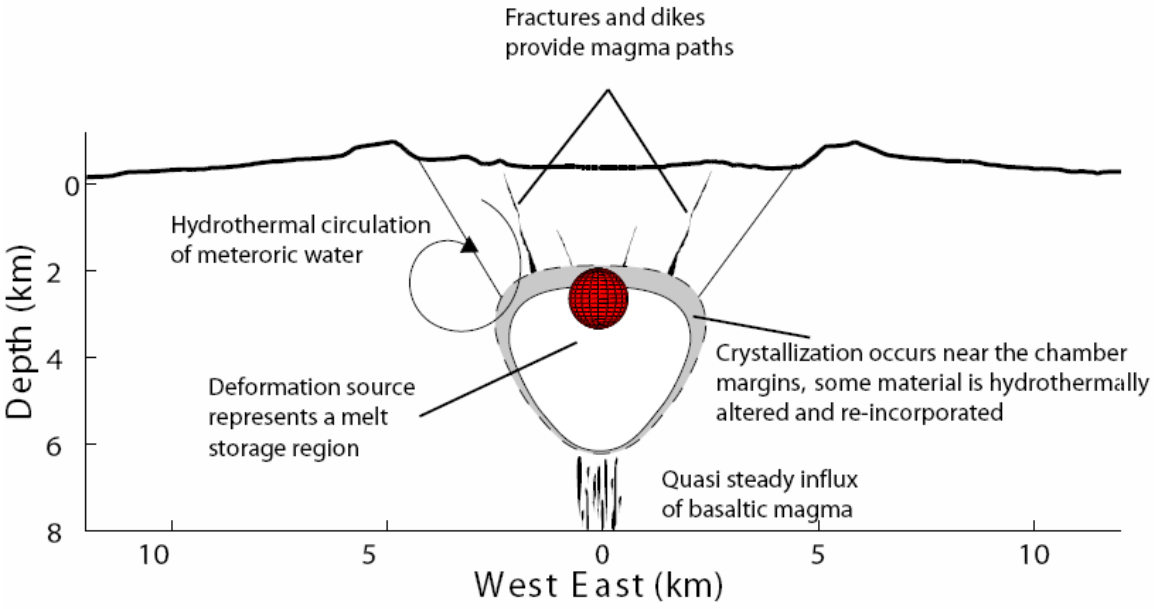

Figure 2.14: Schematic cross-section through Okmok that shows the deformation source located beneath the center of the caldera. The spherical source is drawn with a radius of ~500m and is only meant to indicate the location and finite region that the true source occupies. The true size and dimensions of the magma chamber are unknown. Conical fractures emanating from the magma storage region provide pathways to the cones in the caldera. Petrologic work by *Finney et al.* [*2008*] suggests that hydrothermal alteration occurs in crystals that accumulate near the chamber margins.

the shallow reservoir during the eruption. This suggests that the recent changes in the inflation rate are related to changes in the magma supply rate to the shallow chamber.

The deformation source likely represents a relatively long-lived shallow magma reservoir beneath Okmok. The 1997 flow volume [*Lu et al., 2003a*] is similar to the 1958 flow volume [*Lu et al., 2005*] indicating that a similar process of eruption capacity has existed since before 1958. Within 10 years of the last eruption, Okmok has replenished 60% -80% of the volume lost during that eruption. The CGPS at Okmok allow for assessment of the shorter term fluctuations in inflation rate while campaign GPS measurements provided only the time-averaged inflation rate. At least two-thirds of that volume recovery occurred in the two short duration bursts of rapid inflation between 2003 and 2005. Prior to those two inflation bursts, only yearly average estimates are available, but the 1998-2002 influx clearly was less than in 2002-2005.

Some variations in the inflation history leave unanswered questions. What, other than an eruption, causes the volcano to deflate in a predominantly inflating system? Draining magma is a simple explanation, but is not likely in a system where a pressure gradient between a deeper source and a shallow storage area is the driving force in the system. Based on the short deflationary period prior to the 1997 eruption and other studies [*Dvorak and Dzurisin, 1997*; *Lu et al., 2003b*], *Lu et al.* [*2005*] suggest that deflation at basaltic systems such as Okmok may be a precursor to an eruption. However, the past three years at Okmok have shown deflation and general stagnation without an ensuing eruption, which begs the question; how do we distinguish between variability in inflation rates and an actual precursor to an eruption? Stagnation at an actively deforming volcano can come from many causes. Reduction of a pressure gradient between the magma source region and the shallow storage area can prevent magma from making its way toward the surface, halting the inflation trend. The magma supply from depth can decrease or become choked off, resulting in slowed or halted growth of the edifice.

Deflation events preceding eruptions at Kilauea and Krafla are associated with magma leaving the summit reservoir and moving into the rift zones [*Dvorak and Dzurisin, 1997*]. Unlike Kilauea and Krafla, Okmok does not have an active rift system. All historic eruptions have occurred within the caldera. If the same mechanism, of magma moving toward the eruption site, is expected to be the source of deflation at Okmok, then the time between deflation and eruption would likely be very short, as the distance from the source to the surface is less than 5km. Any deflation would be quickly followed by an expansion of the pathway to the vent as the magma increases pressure along the conduit. Unlike Kilauea, at Okmok this inflation component would be spatially overlapping the subsiding area. The InSAR observations by *Lu et al.*, [*2005*] indicate that if deflation at Okmok is an eruption indicator, then the mechanism must be very different form the deflation indicators at Kilauea and Krafla.

For an eruption to be imminent it is fair to assume that the shallow chamber must be at a critical pressure very close to the confining pressure. Depressurization can lead to an eruption by triggering volatile exsolution that recovers and exceeds the pressure loss [*Nishimura, 2004*] and also overcomes the confining pressure. This type of eruption would be preceded by deflation, but that is not sufficient to be an eruption precursor. Pressure recovery due to bubble growth is a rapid process that occurs over short time scales and not over weeks or months, as observed at Okmok. This scenario also requires that the shallow chamber is "full", that is it is near the confining pressure, the minimum pressure required for magma to escape to the surface. In order to identify that a volcano is in a precursory eruptive stage we need to know more than simply the state of deformation.

2.8 Conclusions

The UKF is demonstrated as an effective tool for modeling deformation data from non-linear time-dependent systems. In the two simulated cases of a moving Mogi source the UKF was able to accurately determine all the model parameters and accurately track the changes in the non-linear parameters. It allows for the estimation of hyper-parameters

used for smoothing, and can be easily adapted to many applications to provide quick results. The ability of the UKF to perform with little or no a priori information means that models can be constructed and implemented rapidly. Any forward model, no matter how complex, can easily be incorporated into the filter without any additional coding because Jacobian matrices do not need to be calculated.

The shallow storage region at Okmok has been active since the first geodetic observations were made at the volcano, suggesting that it is a long lived structure. The deformation during the 1997 eruption shows that the magma was residing in the shallow chamber prior to the eruption. A lava flow that occurred in 1958 had a similar volume as the 1997 flow, indicating that the shallow storage region existed prior to that eruption and possibly longer.

The nature of magma emplacement at Okmok makes short duration pulses of rapid inflation that last on the order of months. InSAR observations have suggested a fairly steady inflation rate, but the observations are not frequent enough to capture the dynamics of these emplacement events. All of the deformation that has been recorded by the CGPS instruments has occurred as rapid pulses of inflation.

The rapid and extreme changes in deformation at Okmok demonstrate that simply using the pattern of inflation as a guide is not an appropriate forecasting tool. Okmok has been in a general state of inflation since the 1997 eruption with short and dramatic increases in the inflation rate. These short bursts of activity emplaced magma at 2-3km below sea level and are accountable for roughly two-thirds of the inflation since the 1997 eruption. In order to assess whether future inflation or deflation events will result in an eruption we need to better understand the link between surface deformation and magma dynamics.

2.9 References

Begét, J., J. Larsen, C. Neal, C. Nye and J. Schaefer, (2005), Preliminary Volcano-Hazard Assessment for Okmok Volcano, Umnak Island Alaska, *Alaska Department of Natural Resources Division of Geological & Geophysical Surveys, Report of Investigations 2004-3.*

Blewitt, G., (1989), Carrier phase ambiguity resolution for the Global Positioning System applied to geodetic baselines up to 2000 km, *J. Geophys. Res*., 94(B8), 10187-10203, doi:10.1029/89JB00484.

Cross, R., and J. T. Freymueller, **(**2008**),** Evidence for and Implications of a Bering Plate Based on Geodetic Measurements from the Aleutians and Western Alaska, submitted to *J. Geophys. Res.*, doi:10.1029/2007JB005136.

Cross, R., and J. Freymueller, (2007), Plate coupling variation and block translation in the Andreanof segment of the Aleutian arc determined by subduction zone modeling using GPS data, *Geophys. Res. Lett.*, 34, L06303, doi:10.1029/2006GL028970.

Delany, P., and D. McTigue, (1994), Volume of magma accumulation or withdrawal estimated from surface uplift or subsidence, with application to the 1960 collapse of Kilauea Volcano, *Bulletin of Volcanology*, vol. 56, pp.417-424.

Dvorak, J., and D. Dzurisin, (1997), Volcano geodesy: The search for magma reservoirs and the formation of eruptive vents, *Rev. Geophys.*, 35, 343– 384.

Finney, B., S. Turner, C. Hawkesworth, J. Larsen, C. Nye, R. George, I. Bindeman, and J. Eichelberger, (2008), Magmatic differentiation at an island-arc caldera: Okmok Volcano, Aleutian Islands, Alaska, *Journal of Petrology*, 49, 857-884, doi:10.1093/petrology/egn008.

Fournier, T. J., and J. T. Freymueller, (2007), Transition from locked to creeping subduction in the Shumagin region, Alaska, *Geophys. Res. Lett.*, 34, L06303, doi:10.1029/2006GL029073.

Fukuda, J., T. Higuchi, S. Miyazaki, and T. Kato, (2004), A new approach to time-dependent inversion of geodetic data using a Monte Carlo mixture Kalman filter, *Geophys. J. Int.*, 159, 17-39, doi: 10.1111/j.1365-246X.2004.02383.

Grey, D., (2003), Post-caldera eruptions at Okmok volcano, Umnak Island, Alaska, with emphasis on recent eruptions from Cone A., M.S. thesis, Univ. of Alaska, Fairbanks, Dec.

Haykin, S., (*2001*), The unscented Kalman filter, pp. 1-21, *Kalman Filtering and Neural Networks*, S. Haykin, ed., J. Wiley & Sons, New York.

Johnson , D., (1987), Elastic and inelastic magma storage at Kilauea Volcano, Volcanism in Hawaii, edited by R. Decker, T. Wright and P. Stauffer, *USGS Professional Paper 1350*, p. 1297-1306.

Johnson, D. J., F. Sigmundsson, and P. T. Delaney, (2000), Comment on "Volume of magma accumulation or withdrawal estimated from surface uplift or subsidence, with application to the 1960 collapse of Kilauea volcano" by P. T. Delaney and D. F. McTigue, *Bulletin of Volcanology*, vol. 61, pp. 491-493.

Julier, S. J., (2002), The scaled unscented transformation, *Proceedings of the American Control Conference*, pp. 4555-4559.

Julier, S. J., and J. K. Uhlmann, (2004), Unscented filtering and nonlinear estimation, *Proceedings of the IEEE*, 92, pp. 401-422, doi:10.1109/JPROC.2003.823141.

Larson, K., P. Cervelli, M. Lisowski, A. Miklius, P. Segall and S. Owen, (2001), Volcano monitoring using the Global Positioning System: Filtering strategies, *J. Geophys. Res.*, 106, doi:0148-0227/01/2001JB000305.

Lu, Z., T. Masterlark, and D. Dzurisin, (2005), Interferometric synthetic aperture radar study of Okmok volcano, Alaksa, 1992-2003: Magma supply dynamics and postemplacement lava flow deformation, *J. Geophys. Res.*, 110, B02403, doi:10.1029/2004JB003148.

Lu, Z., E. Fielding, M. Patrick, and C. Trautwein, (2003a), Estimating lava volume by precision combination of multiple baseline spaceborne and airborne

interferometric synthetic aperture radar: The 1997 eruption of Okmok Volcano, Alaska, *IEEE Transactions on Geoscience & Remote Sensing*, vol. 41.

Lu, Z., T. Masterlark, D. Dzurisin, R. Rykhus, and C. Wicks Jr., (2003b), Magma supply dynamics at Westdahl volcano, Alaska, modeled from satellite radar interferometry, J. Geophys. Res., 108(B7), 2354, doi:10.1029/2002JB002311.

Lu, Z., D. Mann, J. Freymueller, and D. Meyer, (2000), Synthetic aperture radar interferometry of Okmok volcano, Alaska: Radar observations, *J. Geophys. Res.*, 105, pp. 10,791-10,806.

Mann D., J. Freymueller, and Z. Lu, (2002), Deformation associated with the 1997 eruption of Okmok volcano, Alaska, *J. Geophys. Res.*, 107, doi:10.1029/2001JB000163.

McGuire, J., and P. Segall, (2003), Imaging of aseismic fault slip transients recorded by dense geodetic networks, *Geophys. J. Int.*, Vol. 155, pp. 778-788.

Miller, T., R. McGimsey, D. Richter, J. Riehle, C. Nye, M. Yount, and J. Dumoulin, (1998), Catalog of the historically active volcanoes of Alaska, *U.S. Geol. Surv. Open File Rep*., 98-0582.

Miyagi, Y., J. Freymueller, F. Kimata, T. Sato, and D. Mann, (2004), Surface deformation caused by shallow magmatic activity at Okmok volcano, Alaska, detected by GPS campaigns 2000-2002, *Earth Planets Space*, 56, pp. 29-32.

Mogi, K., (1958), Relations between the eruptions of various volcanoes and the deformations of the ground surfaces around them, *Bulletin of the Earthquake Research Institute*, vol. 25, pp. 99-134.

National Oceanic and Atmospheric Administration, (2008), National Geodetic Survey, GPS Antenna Calibration, http://www.ngs.noaa.gov/ANTCAL, last access, Dec. 2008.

Niell, A., (1996), Global mapping functions for the atmosphere delay at radio wavelengths, *J. Geophys. Res.*, 101, 3227-3246.

Nishimura, T., (2004), Pressure recovery in magma due to bubble growth, *Geophys. Res. Lett.*, 31, L12613, doi:10.1029/2004GL019810.

Ozawa, S., S. Miyazaki, T. Nishimura, M. Murakami, M. Kaidzu, T. Imakiire, and X. Ji, (2004), Creep, dike intrusion, and magma chamber deflation model for the 2000 Miyake eruption and the Izu islands earthquakes, J. Geophys. Res., 109, B02410, doi:10.1029/2003JB002601.

Perea, L., J. How, L. Breger, and P. Elosegui, (2007), Nonlinearity in Sensor Fusion: Divergence Issues in EKF, modified truncated SOF, and UKF, Proceedings of the AIAA Guidance, Navigation and Control Conference and Exhibit, AIAA 2007-6514.

Psiaki, M., and M. Wada, (2007), Derivation and simulation testing of a sigma-points smoother, *Journal of Guidance, Control, and Dynamics*, Vol. 30, No. 1, pp. 78-86.

Rauch, H.E., F. Tung, and C. T. Striebel, (1965), Maximum likelihood estimation for linear dynamic systems, *AIAA Journal*, Vol. 3, No. 8, pp. 1445-1450.

Segall, P., R. Bürgmann, and M. Matthews, (2000), Time-dependent triggered afterslip following the 1989 Loma Prieta earthquake, *J. Geophys. Res.*, 105, 5615-5634, doi:0148-0227/00/1999JB900352.

Segall, P., and M. Matthews, (1997), Time dependent inversion of geodetic data, *J. Geophys. Res.*, 102, 22,391-22,409, doi:0148-0227/97/97JB-01795.

Sella, G. F., S. Stein, T. H. Dixon, M. Craymer, T. S. James, S. Mazzotti, and R. K. Dokka, (2007), Observation of glacial isostatic adjustment in “stable” North America with GPS, *Geophys. Res. Lett*., 34, L02306, doi:10.1029/2006GL027081.

Van der Merwe, R., E. Wan, and G. Harvey, (2007), *ReBEL: Recursive Bayesian Estimation Library*, OGI School of Science and Engineering, Oregon Health & Science University, http://choosh.csee.ogi.edu/rebel/.

Van Zandt, J., (2002), Boost phase tracking with an unscented filter, *MITRE Corporation*, MS-M210, 202 Burlington Road, Bedford MA 01730, USA.

Wan, E.A., and R. van der Merwe, (2001), The unscented Kalman filter, pp. 221-280, *Kalman Filtering and Neural Networks*, S. Haykin, ed., J. Wiley & Sons, New York.

Williams, C., and G. Wadge, (1998), The effects of topography on magma reservoir deformation models: Application to Mt. Etna and radar interferometry, *Geophys. Res. Lett*., 25, 1549–1552.

Zumberge, J. F., Heflin, M. B., Jefferson, D. C., Watkins, M. M., and Webb, F. H., (1997), Precise point positioning for the efficient and robust analysis of GPS data from large networks, *Journal of Geophysical Research*, v. 102, p. 5005-5017.

Chapter 3: Deflation at Okmok Volcano and the role of volatiles in deformation

3.1 Abstract

The deformation record at Okmok Volcano consists of short periods of inflation followed be smaller magnitude deflation signals. This pattern is assumed to be caused by intrusion of magma to a shallow chamber followed by degassing of that magma. A degassing model is created using the thermodynamic program VolatileCalc. Constraints on the magma composition come from petrologic analysis of lava erupted in 1997. The model explores the effects that chamber size, degassing rate and volatile composition of the magma have on surface deformation. The model is applied to estimates of the volume change of the magma chamber obtained from the GPS network at Okmok. The analysis shows that the magma chamber has a radius between 1 and 2km and that the volatile content of the intruding magma contains less than ~500ppm CO_2.

3.2 Introduction

Volatile content plays an important role in bringing magma to shallow depth and in producing eruptions. Volatile behavior is a significant factor in contributing to surface deformation, and is important when considering the mass of magma that is causing the deformation [*Johnson et al., 2000*]. Accounting for gas compressibility and solubility in magma is an important step in understanding volcano deformation source processes. By combining knowledge of magma composition, surface position observations, and thermodynamic models, a more reliable estimate of magma mass can be determined.

Differences in geologic estimates of erupted volume and geodetic estimates of the magma withdrawn from the magma chamber can be linked, in part, to improper accounting of the compressibility of the magma [*Sigmundsson et al., 1992*], which is due chiefly to a gas phase in the melt. *Rivalta and Segall* [*2008*] showed that discrepancies between the volume changes at magma sources (storage regions) and magma sinks (dikes or sills) could be explained by accounting for the compressibility of the magma and the compressibility of the source and sink. *Bower and Woods* [*1997*] used a numerical

model to demonstrate the effect that magma compressibility has on eruption volumes. Not surprisingly, a larger volume of compressible magma is required to relieve magma chamber overpressures.

Surface displacement observations can provide estimates of the volume change of the magma chamber [*Sigmundsson et al., 1992; Delaney and McTigue, 1994; Johnson et al., 2000*], but this type of observation does not directly inform about the magma intrusion volume or mass. This is due to the fact that magma, particularly magma with volatiles, is a compressible material and will deform due to the same pressure change that causes a volume change in the magma chamber. Geodetic observations coupled with gravity provide a combination that can distinguish magma intrusion volumes [*Johnson, 1987*; *Battaglia et al., 2006; Gottsman et al., 2006*]. An alternate approach is to use geodetic observations and measurements of magma properties so that a reliable estimate of the compressibility can be used in calculating magma mass. The latter is the approach taken here. The mass estimate is then used to determine the amount of volatiles available for degassing.

We consider a shallow magma chamber filled with a compressible magma that is intruded by over-saturated magma, which in turn degasses in the low pressure environment. The intruding magma causes inflation of the volcano edifice and the resulting degassing produces deflation. This model is applied to the deformation record at Okmok Volcano, Alaska to determine if degassing is a reasonable explanation for the observed deflation.

3.3 Geologic Setting

Okmok is one of the most historically active volcanic centers in the Aleutian Arc with 17 reported eruptions since 1805 [*Grey,* 2003]. The large caldera at Okmok was formed in prehistoric eruptions 12,000 and 2000 years ago, which produced voluminous deposits [*Begét et al., 2005; Larsen et al., 2007; Finney et al., 2008*]. Most historic eruptions are believed to emanate from Cone A, a vent in the southwestern region of the caldera (Fig. 3.1) [*Miller et al., 1998*]. In 1997 Okmok erupted a basaltic-andesite lava

from Cone A, similar in composition to most historic eruptive products [*Miller et al., 1998; Grey, 2003*]. The 1997 eruption gives a glimpse of the likely composition of the magma involved in the recent deformation episodes. Eruptive products from the July 2008 eruption may be useful in further constraining or verifying the work presented here, but data from this episode were not available as of this writing.

At Okmok Volcano continuous GPS instruments (CGPS) have recorded pulses of inflation. These pulses are followed by a period of deflation. Since magma intrusion is the likely cause of the inflation, it is reasonable to suspect that the loss of exsolved gasses could be the cause of the deflation. The GPS record shows both high deformation rates and large displacements occur at Okmok. Between 1997 and 2008 maximum uplift exceeded 0.5m. Most of the deformation since the start of continuous observations in 2002 has occurred in discrete pulses rather than as steady uplift. Figure 3.2 has an example time series from OKCE showing the pulsating nature of inflation. A curious observation is that after each inflation pulse the volcano deflates slightly. The source of deflation may come from one of many processes: thermal contraction as the intrusion cools, crystallization of the magma body, draining of the magma, depressurization caused by the release of gas, or some combination of these. Although geodetic techniques can observe the deflation and determine where the deflation has occurred, it can not, by itself, shed light on the process that causes deflation. In this paper the deformation record is examined in light of petrologic constraints and thermodynamic models to determine the role that degassing plays in the deflation observed at Okmok.

3.4 Data

Okmok is host to a suite of volcanic monitoring instruments including CGPS and a seismic network as well as a network of campaign GPS benchmarks (Fig 3.1). Campaign GPS observations began in 2000 and the continuous sites were installed in 2002 and 2004.

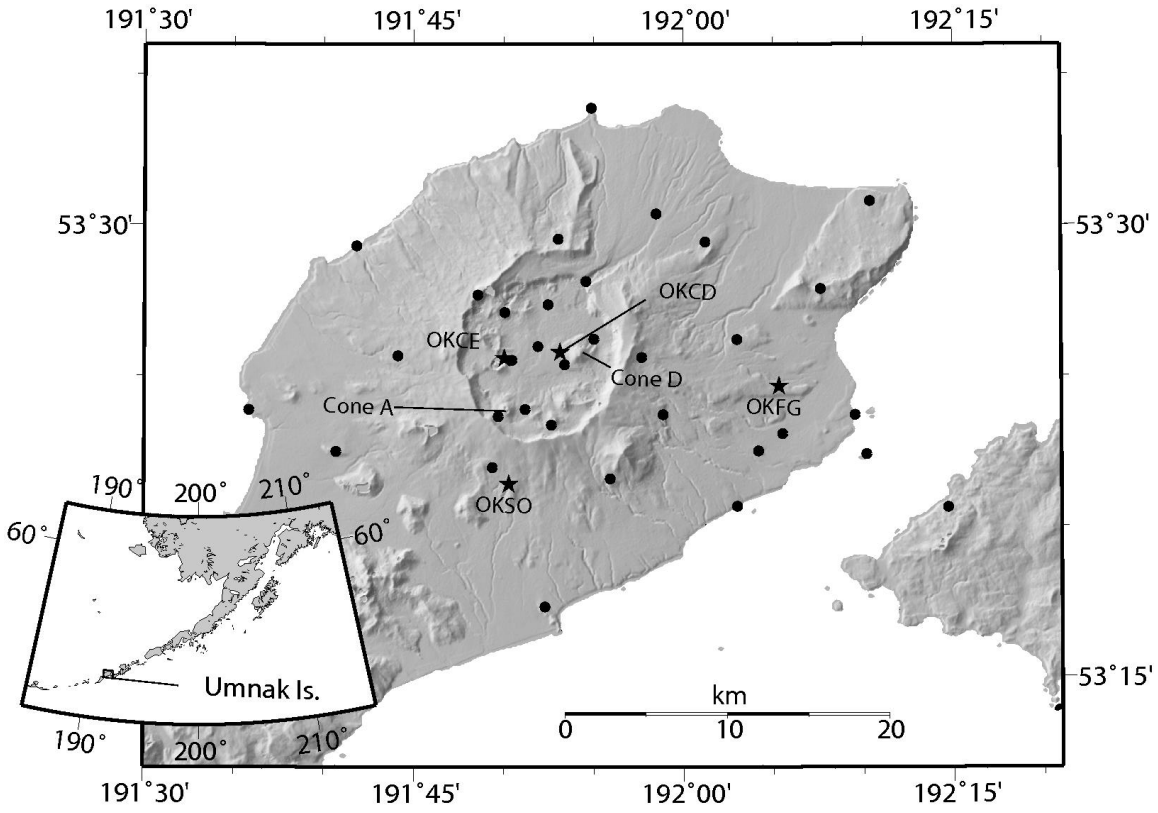

Figure 3.1: The GPS network on Okmok Volcano consists of 33 campaign GPS sites (dots) and 4 CGPS instruments (stars). Cone A is the site of most historic eruptions (including 1997). Cone D is the most prominent feature inside the caldera, and the site of the 2008 eruption. The base map is a digital elevation model obtained from the Shuttle Radar Topography Mission.

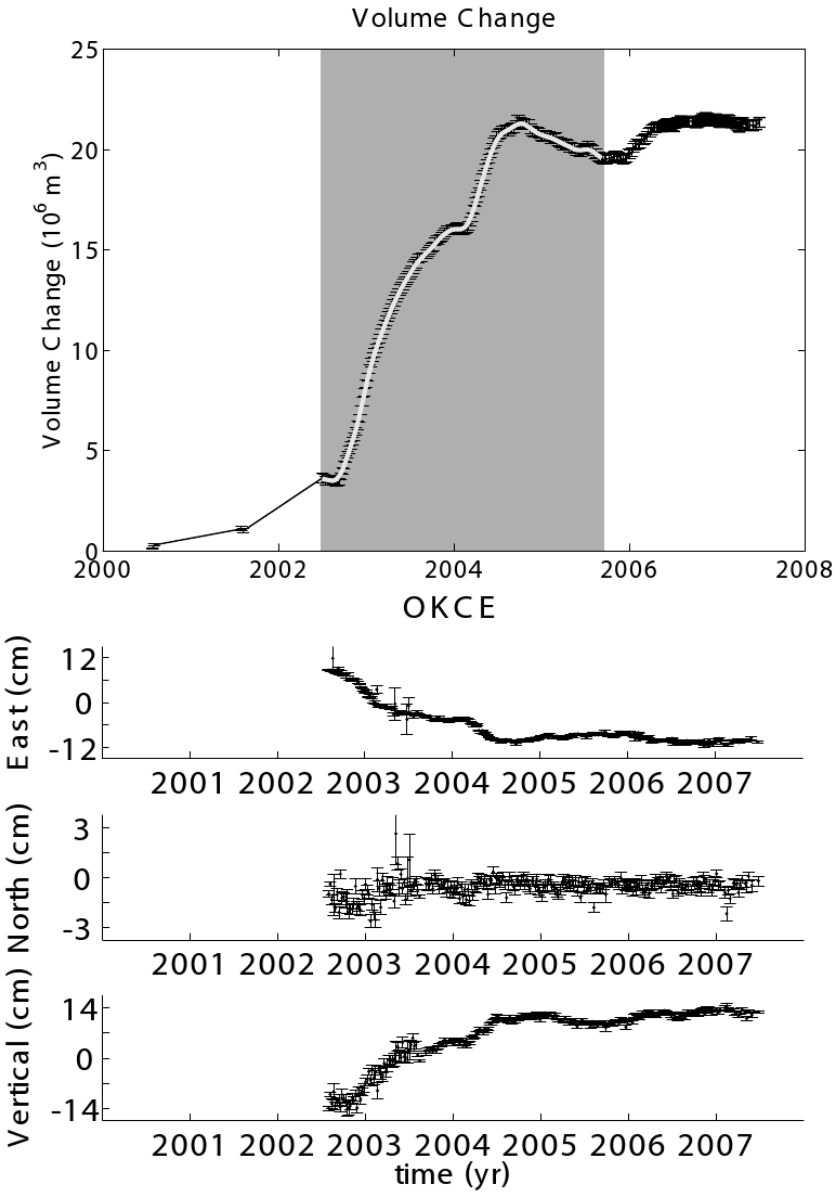

Figure 3.2: The volume change of the magma chamber beneath Okmok is tracked through time with the GPS network [*Fournier et al.,2008; Chp. 2*]. The top panel shows the estimate of the cumulative volume change since 2000, the period of time that this study focuses on is shown in gray. The white line is the smoothed volume change curve used as data in the study. The bottom panel shows the three component site motion of OKCE.

It has been observed with InSAR for more than a decade [*Lu et al., 2000; Mann et al. 2002; Lu et al., 2005*], with results showing active deformation throughout the time span. The active deformation of the volcano makes it an ideal location to study intrusive and extrusive behavior. In the past eight years campaign and continuous GPS instruments have recorded several periods of inflation in 2002, 2004 and 2006 [*Miyagi et al., 2004; Fournier et al., 2008*]. Model results from both InSAR and GPS indicate a source located approximately 3km beneath the center of the caldera. Seismic activity at Okmok consists of a low rate of volcano-tectonic style earthquakes, but lots of energetic tremor, roughly associated with times of active deformation.

This study focuses on the inflation from 2003 to 2004 and the associated deflation (gray region in Fig. 3.2). The volume change results from *Fournier et al.* (*in review*; *Chp. 2*) are used to test the degassing model. Those results used all the available GPS data to obtain the volume change estimates. The GPS data were inverted using the Unscented Kalman Filter [*Fournier et al., in review; Chp. 2*] for the best Mogi source location, depth and volume change. In order to better interpret the results, the volume change time series is smoothed to remove high frequency fluctuations due to noise. The smoothed volume change time series is used as the primary data for this study (Fig. 3.2).

The GPS data are processed in daily solutions using GIPSY-OASIS [*Zumberge et al., 1997*] release GOA4, in network mode, incorporating data from all GPS sites in and around Alaska, with ALGO as a reference clock. Elevation-dependent phase center models (IGS01) for each of the individual antennas are applied with a 10° elevation mask [*NOAA, 2008*]. The TPXO.2 ocean tidal model is used, and wet tropospheric path delays are estimated using the Niell mapping function [*Niell, 1996*].

Problems with data logging prevented complete records from the CGPS sites during the first year of operation. Stations OKCD and OKFG stopped logging during the year and OKCE only recorded one hour of data per day. In order to maximize the usefulness of the short observation period at OKCE, an ambiguity resolved solution [*Blewitt, 1989*] is employed for this time period that uses the Okmok network, sites

located on nearby Akutan Volcano, and a few sites located on stable North America in the conterminous United States.

3.5 Mechanisms for Deflation

The source of deflation may come from one of many processes: thermal contraction of a cooling intrusion, crystallization of the magma body, draining magma, and depressurization caused by the release of gas, or some combination of these. Although geodetic techniques can observe the deflation and determine where the deflation has occurred, by itself geodesy can only give a limited insight on the process that causes deflation. Here we use petrologic studies to constrain the volatile content and thermodynamic behavior of the magma. All of these mechanisms may cause deflation, but they may not adequately explain the characteristics of the signal observed at Okmok.

The process of thermal contraction is not likely. The subsidence observed at Okmok following the inflation period from 2002 to 2004 is much larger than anticipated from contraction of a cooling magma body, and the time frame over which the subsidence occurs is shorter than expected. The rate of cooling would have to be extremely rapid to match the deformation signal. Geodetic estimates put the magma body at approximately 3km below the surface. Using a geothermal gradient of 20˚C/km gives an ambient temperature of roughly 330˚C at this depth. To cool from ~1000˚C to 330˚C during the time span of the deformation would require a cooling rate of ~1˚C/day. Temperature measurements from bore holes in Kilauea Iki lava lake suggest a cooling rate of 0.5˚C/day [*Alut et al.,* 1965]. The larger size and insulated environment of a buried magma body should result in a slower cooling rate than a lava lake situated at the surface. Nevertheless, if the magma body at Okmok is cooling at a sufficiently rapid rate, thermal contraction still can not explain the total deformation signal. *Lu et al.* [*2005*] used a coefficient of thermal expansion of 10^{-5} K^{-1} to explain subsidence caused by cooling lava flows in Okmok Caldera. Using this value and assuming that the entire magma intrusion volume, ~20 million m^3, cools from the magma temperature, 1025˚C, to the ambient temperature at 3km depth gives a contraction volume ~0.14 million m^3. A uniform

contraction of this magnitude would produce roughly 4mm of subsidence. The observed subsidence in 2005 was a few centimeters.

Crystallization may begin soon after emplacement, but the magnitude of contraction is not expected to be large. Also, at low pressure crystallization can lead to second boiling by concentrating volatiles in the melt, resulting in inflation of the edifice [*Sisson and Bacon, 1999*].

Draining of the magma from the shallow chamber back to a deeper storage region might occur if the density of the magma increases. Densification of the magma is likely, particularly if degassing occurs in the shallow chamber. At Askja Volcano in Iceland mass changes observed by gravity surveys suggest that magma draining is the source of a long lived deflation from 1988 to 2003 [*de Zeeuw-van Dalfsen et al., 2005*]. The rift system and extensional environment at Askja Volcano provides many potential magma sinks that could accept a large volume of magma without a corresponding surface deformation expression. Okmok Volcano is located in a compressional environment and does not have a large rift system that could act as a sink for draining magma; such as exists at Kilauea, Krafla [*Dvorak and Dzurisin, 1997*] or Askja [*de Zeeuw-van Dalfsen et al., 2005*]. At Okmok Volcano, draining magma would have to move to a depth such that the surface deformation due to magma accumulation would not be detectable. Since magma draining is a mechanism that cannot be verified with the data from Okmok Volcano, we assume that this mechanism plays, at most, a minor role and instead focus on degassing as a mechanism for the observed deflation.

Gas loss, following an intrusion of volatile rich magma, provides a probable explanation for deflation. When the intruding magma reaches the shallow chamber it is oversatured in volatiles, resulting in volatiles entering the gas phase. Gases that are exsolved at shallow depth may escape the magma and be lost to the atmosphere, with a resultant deflation of the magma chamber. The following section outlines how degassing effects surface deformation and how volatile concentrations, both dissolved in the magma and in the gas phase, are calculated.

3.6 Degassing Hypothesis

We hypothesize that the deflationary signals observed in the Okmok deformation record are due to degassing of volatiles. GPS data allow for an estimate of volume change at depth, and from thermodynamic models the relative volume of exsolved volatiles can be separated from the magma volume. This gives volume estimates of two separate phases: a relatively incompressible liquid-crystal mixture and a highly compressible gas mixture. These two components contribute to the deformation observed at the surface and initially act as a single unit, liquid magma containing gas bubbles. The gas bubbles rise due to density differences and separate from the liquid part of the magma and eventually escape to the atmosphere. This process results in a decrease in volume (or pressure) of the magma chamber due to the loss of the gas phase, which in turn deflates the ground surface. The purpose of this study is to determine if the volume loss is enough to explain the GPS observations. The model in this study places boundaries on a few important parameters including: magma chamber dimension, maximum and minimum volatile content of the magma, the ratio of H_2O to CO_2 concentration, and degassing rate.

The thermodynamic modeling program VolatileCalc [*Newman and Lowenstern, 2002*] is used to create a degassing model that determines the magnitude of deflation caused by degassing of a magma intrusion. VolatileCalc provides a solution model for the basalt-H_2O-CO_2 system. It uses modified Redlich-Kwong equations to determine the vapor fugacities and resulting volatile concentrations [*Newman and Lowenstern, 2002, and references therein*]. Here we use VolatileCalc to calculate gas volumes, volatile concentrations, magma compressibility, and magma density.

The equations for the surface displacements caused by an isotropic point source are given by *Mogi* [*1958*],

$$u_r = C\frac{r}{\left(r^2 + d^2\right)^{3/2}} \tag{3.1}$$

$$u_z = C\frac{d}{\left(r^2 + d^2\right)^{3/2}}, \tag{3.2}$$

where r is the radial distance from the source to the observation point and d is the depth of the source. The displacements u_r and u_z correspond to the radial and vertical displacements, respectively. The coefficient in equations 3.1 and 3.2 are referred to as the source strength or potency and can be written in terms of properties of the magma chamber, $C = 3a^3\Delta P/4\mu$, where a is the chamber radius, ΔP is the pressure change inside the chamber that causes the deformation and μ is the shear modulus of the host rock. From the form of the source strength coefficient it is clear that the chamber radius and pressure change inside the chamber are not separable without additional information. The volume change caused by displacement of the chamber walls can be determined by surface deformation estimates. The displacement of the chamber wall results in a volume change, $\Delta V_c = 4\pi C/3$ [*Johnson, 1987*; *Delaney and McTigue, 1994*]. This volume change only represents the change associated with the deformation of the spherical chamber, but in the limiting case of an incompressible fluid this is also the volume of the fluid intrusion.

The volume of magma intrusion is better determined by considering the compressibility of the magma. The pressure associated with magma intruding into the chamber both expands the chamber walls and compresses the magma already existing in the chamber. The compression of the magma inside the chamber is dependent on the compressibility, β_m, of the magma occupying the chamber. From *Johnson* [*1987*] this relationship is

$$\Delta V_\beta = \frac{4}{3}\Delta P\beta_m\pi a^3 = \frac{16}{9}C\mu\pi\beta_m = \frac{4}{3}\Delta V_c\mu\beta_m. \tag{3.3}$$

In a system where all the magma is contained within the chamber (i.*e.* no degassing), the magma intrusion volume is the sum of the volume change of the chamber

walls and the compression of the magma inside the chamber, $\Delta V_i = \Delta V_c + \Delta V_\beta$. We write this in terms of the volume change caused by displacement of the chamber walls,

$$\Delta V_i = \Delta V_c\left(1+\frac{4}{3}\mu\beta_m\right). \tag{3.4}$$

Rivalta and Segall [*2008*] find the same relationship for the specific case of a dike or sill intrusion that is supplied by a magma chamber at the same depth. This is not a surprising result because both problems deal with the magma volume associated with a pressure change in an ellipsoidal chamber.

Degassing can be added to equation 3.4 simply by adding the degassed volume, ΔV_{dg}, to the right side of the equation,

$$\Delta V_i = \frac{4}{3}\pi a^3\Delta P\left(\frac{3}{4\mu}+\beta_m\right)+\Delta V_{dg} = \Delta V_c\left(1+\frac{4}{3}\mu\beta_m\right)+\Delta V_{dg}. \tag{3.5}$$

Using equations 3.1 and 3.2, observations from geodetic techniques can be used to estimate the volume change of the chamber, $\Delta\hat{V}_c$, providing partial control on the intrusion volume. With some knowledge of the magma composition, inferences can be made regarding ΔV_β and ΔV_{dg}.

The volume of degassed volatiles depends on the mass of exsolved volatiles in the magma chamber. The mass of exsolved volatiles, M_e, is expressed as $M_e = \phi_e\rho_m V_c$, where ϕ_e is the mass fraction of exsolved volatiles, ρ_m is the magma density and V_c is the chamber volume. Both the magma density and the mass fraction of exsolved volatiles are determined with VolatileCalc. To ensure that the two vapor components degas in the same proportion that exists in the gas phase, we use a degassing rate, r, to control the mass flux from the chamber. The degassed volume is proportional to the total volume of exsolved volatiles and the duration over which degassing occurs, Δt. The degassed volume is given by:

$$\Delta V_{dg} = \left(\frac{M_{eH_2O} v_{H2O}}{G_{H_2O}} + \frac{M_{eCO_2} v_{CO_2}}{G_{CO_2}} \right) r \Delta t , \qquad (3.6)$$

where G is the molar mass of the volatile species, and v is the molar volume of the gas species at the relevant temperature and pressure. Although degassing is a continuous process and the rate of degassing may vary with time, it is assumed that for short time steps degassing is constant.

The mass fraction of exsolved volatiles in the magma chamber is related to the total volatile content in the magma which is affected by the degassing rate and replenishment of volatiles by magma intrusion. If degassing occurs more slowly than the volatile input from intrusion then volatiles will accumulate in the magma chamber. If degassing dominates then the net flux of volatiles will be out of the chamber. The mass of volatiles in the chamber is

$$M_v = (\phi_{mH_2O} + \phi_{mCO_2}) \rho_m V_c + (\phi_{iH_2O} + \phi_{iCO_2}) \rho_i \Delta V_i - \left(M_{eH_2O} + M_{eCO_2} \right) r \Delta t , \qquad (3.7)$$

where the first term is the mass of volatiles in the chamber before the intrusion or degassing has occurred, the second term is the volatile input from intrusion and the last term is the amount of volatiles lost by degassing. The total mass fraction of volatiles in the chamber is ϕ_m, and in equation 3.7 the total mass fraction of each species is noted. The intrusion has density ρ_i, volatile mass fraction ϕ_i, and volume V_i.

The magma compressibility, magma density, and mass fraction of exsolved volatiles can be determined using VolatileCalc, provided the mass fraction of volatiles in the magma is known. The mass fraction can be written as,

$$\phi_{mH_2O} = \frac{M_{vH_2O}}{\rho_m V_c}, \qquad \phi_{mCO_2} = \frac{M_{vCO_2}}{\rho_m V_c} \tag{3.8}$$

where M_{vH2O} and M_{vCO2} are the total masses of H_2O and CO_2, respectively, in the magma chamber, and can be determined by modifying equation 3.7.

Figure 3.3 outlines how these equations are put together to determine the changes to the system. In order to determine the volume of intruded magma, we first need to determine the compressibility of the pre-existing magma, which depends on its volatile content. The magma in the chamber is initially assumed to be saturated in volatiles, but without any exsolved in the chamber, so the initial magma density and compressibility are determined from this state. The intrusive volume determines the amount of volatiles added to the chamber and the degassing rate determines how much has escaped. After accounting for the net flux of volatiles, the compressibility can be re-calculated and the entire procedure repeated. The symbols used in this section are explained in Table 3.1. The model outlined above is a forward model where the volume of the magma intrusion is constrained by the observed inflation. The mass of the intrusion depends on the magma composition, solution dynamics of the basaltic fluid, the chamber volume, and the degassing rate. The deflation of the volcano edifice ultimately depends on the volume of gas removed from the magma chamber, which is dependent on all of the above factors. Because the intrusion volume is required to match the data, there is only a potential for misfit during times of deflation. In the following sections, we discuss some constraints that are used to limit the parameter space.

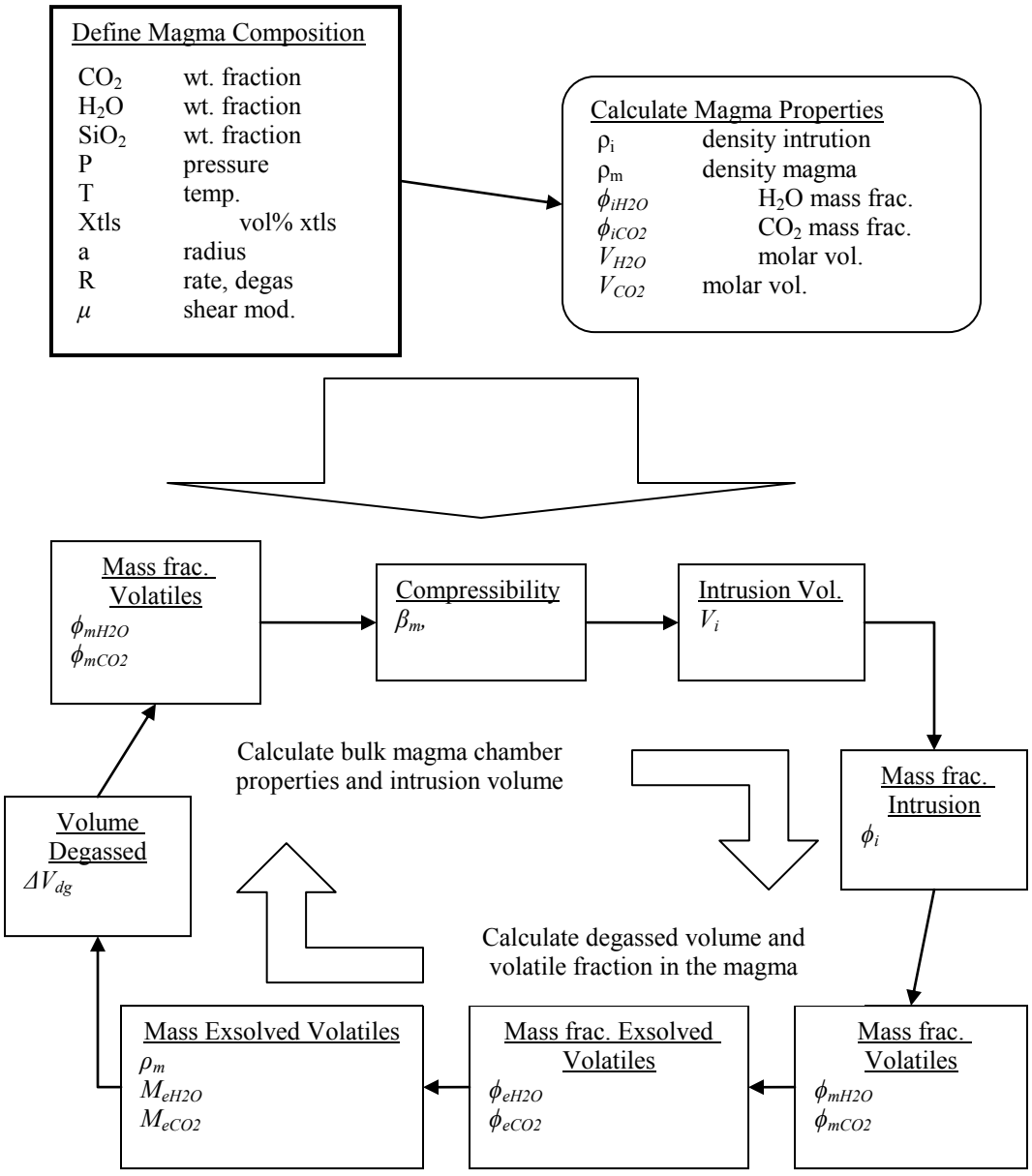

Figure 3.3: A flow chart for a linked magma intrusion/degassing system shows how calculations are performed. Each box shows the parameters calculated at that step.

Table 3.1: Symbols used to describe the degassing procedure.

Symbol	Description	Value range
	Magma Chamber Properties	
a	Chamber radius	500-5000m
V_c	Chamber volume	$4/3\pi a^3$
ΔP	Pressure change inside chamber	-
ΔV_o	Volume change observed by GPS	$\Delta V_o \approx \Delta V_c$
μ	Host rock shear modulus	30 GPa
ΔV_c	Volume change of the chamber	-
$\Delta \hat{V}_c$	Estimate of the chamber volume change (from GPS)	-
ΔV_i	Intrusion volume	-
ΔV_β	Volume change due to magma compression	-
ΔV_{dg}	Volume change from degassing	-
	Magma Properties	
β_m	Magma compressibility	-
ϕ_{mCO2}	Mass fraction CO_2 in the magma chamber	-
ϕ_{mH2O}	Mass fraction H_2O in the magma chamber	-
ϕ_{iCO2}	Mass fraction CO_2 in the intrusion	0-9000ppm
ϕ_{iH2O}	Mass fraction H_2O in the intrusion	2.5-8wt%
ϕ_e	Mass fraction of exsolved volatiles	-
M_{eH2O}	Mass of exsolved H_2O	-
M_{eCO2}	Mass of exsolved CO_2	-
M_{vH2O}	Mass of H_2O in the magma chamber	-
M_{vCO2}	Mass of CO_2 in the magma chamber	-
M_v	Total mass of volatiles in the magma chamber	$M_v = M_{vH2O} + M_{vCO2}$
ρ_m	Density of magma in the chamber	-
ρ_i	Density of magma intrusion	-
G_{H2O}	Molar mass of H_2O	18.0152 g/mole
G_{CO2}	Molar mass of CO_2	44.0095 g/mole
v_{H2O}	Molar volume (at 70 MPa)	149.62 cc/mole
v_{CO2}	Molar volume (at 70 MPa)	180.53 cc/mole
	Degassing Properties	
r	Degassing rate	.001-6 yr^{-1}
Δt	Time increment	1week
	Mogi Source Properties	
u_r	Radial displacement	-
u_z	Vertical displacement	-
r	Radial distance from the source to the station	-
d	Depth of the source	(3km)
C	Source strength	~0-4 x 10^6 m^3

3.7 Model Constraints

3.7.1 Magma Constraints

Products from the 1997 eruption provide an insight to the magma composition and volatile content at Okmok. The 1997 magma is ~53wt.% SiO_2 and 17vol.% crystals [*Izbekov et al., 2005*]. Phase equilibria experiments conducted on the 1997 samples confine the pressure-temperature regime to 62-76MPa and 1025-1050 °C [*Izbekov et al., 2005*]. At this pressure range, experiments and numerical models indicate that the magma would be saturated with ~2.5wt.% volatiles. Melt inclusions confirm that the melt contains ~2.5wt.% volatiles, and some melt inclusions have a volatile content as high as ~3.5wt.%, which likely formed at higher pressure. For the basaltic system, VolatileCalc only accepts a maximum of 49wt.% SiO_2, but the small difference in SiO_2 content is not expected to have a large impact on the solubility calculations [*Newman and Lowenstern, 2002*]. For each model run the temperature and pressure are fixed at 1025°C and 700 MPa, respectively.

It is important to know the initial volatile concentration in the magma as this will determine the rate at which volatiles enter the magma chamber and the availability of gas for degassing. An upper bound on the volatile content comes from worldwide observations of subduction related basaltic magmas. *Wallace* [*2005*] examined published melt inclusion and volcanic gas data and found that these systems can have as much as ~6wt.% H_2O and as much as 0.6-1.3wt.% CO_2 in the primary magma. CO_2 in these concentrations becomes saturated at depths shallower than ~20km, so that by the time the magma reaches lower pressure some of the CO_2 has left the system, some remains trapped in bubbles, and a small amount remains dissolved in the melt.

The dissolved volatile content measured in the 1997 lavas can be divided into relative amounts of H_2O and CO_2 provided the concentrations of other volatile components are small. In the two phase system a dissolved volatile concentration of 2.5wt.% can be achieved with a variety of primary H_2O and CO_2 concentrations. Figure

3.4 shows how dissolved volatile content varies as a function of the primary CO_2 and H_2O content in a basaltic magma with 49wt.% SiO_2 at 1300 K (1025°C) and 70 MPa. The figure can be used to predict the amount of exsolved volatiles in the magma, but more importantly it defines the range of initial volatile concentrations that are consistent with the amount of volatiles dissolved in the 1997 lava. For example, magma with an initial concentration of 4.5wt.% H_2O and 1000ppm CO_2 will have ~2.55wt.% volatiles dissolved in the melt and the remaining 1.95wt.% in the gas phase. With an uncertainty in the measured amount of dissolved volatiles greater than ± 0.05wt.%, this initial concentration would be in agreement with the 1997 observation. The uncertainty of the dissolved volatile content of the Okmok lava is unknown, but it is likely larger than 0.1wt.% which means that any initial volatile concentration above ~2.5wt.% H_2O is in agreement with the measurements from the 1997 lava.

Detailed examination of the melt inclusion data from the 1997 eruption might help to narrow the possible range of primary volatile content. *Papale* [*2005*] described a method to determine primary H2O and CO2 concentrations from the volatile concentrations in melt inclusions and their estimated pressures of formation. Although it is beyond the scope of this study, this method could help to constrain the results obtained here.

3.7.2 Degassing Constraints

The rate at which volatiles leave the system is an important constraint for limits on the model. Mass flux by degassing is highly dependent on the chamber radius, volatile content of the magma and the degassing rate. Measurements of gas flux from Okmok do not exist, so observations from volcanic systems world wide provide an upper bound on the CO_2 flux. During an inferred intrusive event at Mt. Spurr, Alaska in 2004 [*Power, 2004*] a maximum CO_2 flux was measured at 1400 tons/day [*Doukas and McGee, 2007*], compared to 12,000 tons/day, the highest flux measured during the 1992 eruption [*Doukas, 1995*]. From another inferred intrusive event in 2006 at Fourpeaked Volcano,

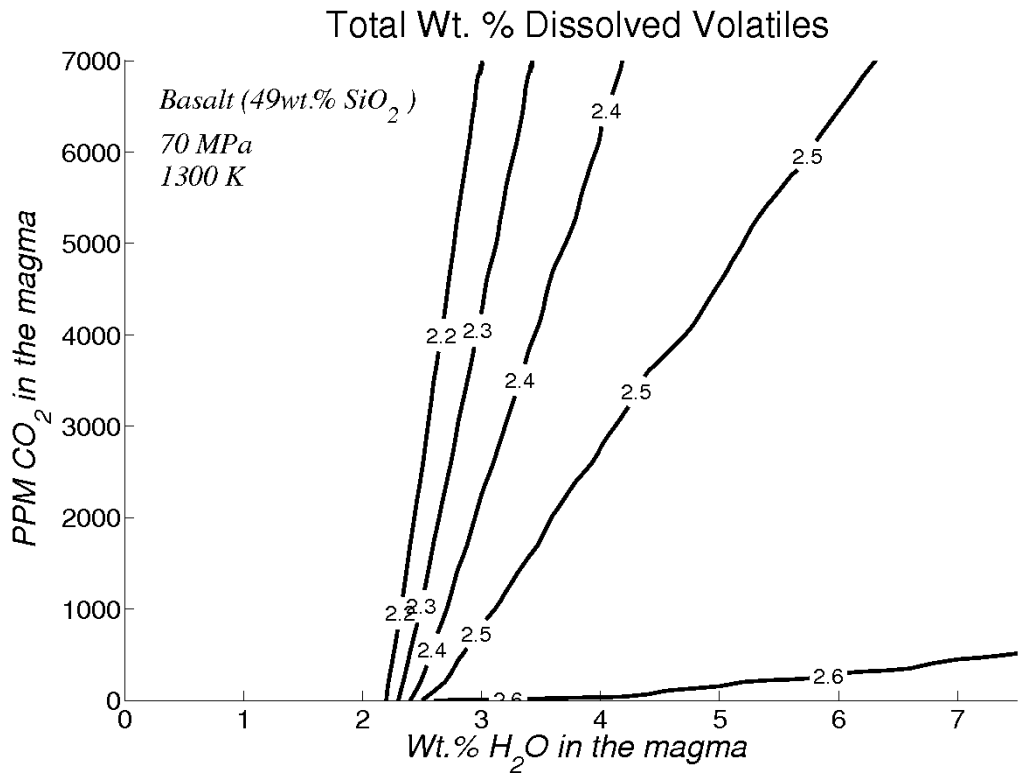

Figure 3.4: Dissolved volatile content varies as a function of the total H_2O and CO_2 content. Here the contours of wt.% total dissolved volatiles are plotted for magma with 49wt.% SiO_2 at 70 MPa and 1300 K. For magma with initial concentrations of 5wt.% H_2O and 4000ppm CO_2 roughly 2.5wt.% is dissolved in the melt and 2.5wt.% is in the gas phase.

Alaska a CO_2 flux of 830 tons/day was recorded [*Doukas and McGee, 2007*]. A 1996 intrusion beneath Iliamna Volcano, Alaska resulted in a measured CO_2 flux of 880 tons/day [*Roman et al., 2004*]. Passive degassing of the open system at Mt. Etna, Italy releases roughly 2000 tons/day with significant increases during eruptive activity [*Aiuppa et al., 2006*]. Because there have not been any measurements of gas flux at Okmok it is difficult to estimate a normal value, but from these examples a CO_2 flux of 1-2 kilotons per day should not be considered abnormal.

3.8 Evaluating Model Results

The model described in section 3.6 and outlined in Fig. 3.3 is run for a variety of parameter values. For each model run an intrusion volume is determined such that the predicted volume change of the chamber walls, ΔV_c, matches the volume change estimated by GPS, $\Delta \hat{V}_c$. Intrusion can occur at any time, but deflation can only be caused by the degassing of the magma chamber and depends on the amount of exsolved volatiles in the chamber and the rate at which the gas escapes. Misfit during deflation is caused by two different factors: 1) insufficient volatiles in the chamber, which is caused by small intrusion volumes or from low volatile concentrations in the intruding magma, and 2) a degassing rate that is too slow to match the deflation rate.

The overall fit to the data is assessed with the χ^2 statistic, calculated as the weighted sum of squared residuals. The inverse of the data variances are used as the weights. Because the model can only misfit the data during deflation, which occurs at less than half of the data points, χ^2 can have a very small value, and falls in the range ~0-580. A value of 30 is a rough cut-off between models with an acceptable or unacceptable fit to the data.

There is no constraint in the forward model to limit the mass flux of volatiles to an acceptable level, so an additional criterion is used to evaluate the models. Measurements of CO_2 mass flux are used as a guide when ranking the goodness-of-fit for the various models. The volatile mass flux is not set *a priori* in the model; instead it is

determined from the degassing rate and the amount of exsolved volatiles in the magma chamber which is a function of the chamber size and volatile content of the intruding magma. Lacking a measurement of mass flux, we opt not to have a hard constraint on the flux of CO_2 from Okmok. Instead we penalize models with excessive CO_2 fluxes. For any flux that exceeds a critical value the model is penalized according to a penalty function (Fig. 3.5), where the penalty increases with the amount that the critical value is exceeded by. We choose 2000 tons/day as the critical flux value, where any flux below this is not penalized and any flux exceeding this value receives a penalty according to *cosh(f/1500) -1*, where *f* is the flux. This functional form was chosen to allow models that exceed the critical flux by small amounts, but to effectively exclude any model that greatly surpasses the critical value. All models are ranked by the χ^2 value plus the sum of the penalties (Fig. 3.5). This ensures that the best models fit the data reasonably well and have realistic mass fluxes.

3.9 Results

At Okmok there are constraints for several of the parameters that describe the magmatic system, but not all of them. We take the approach of varying the unconstrained parameters to examine the effect that those parameters have on the deformation trends. For this study we use a temperature of 1025°C, a pressure of 70MPa, a basaltic magma with 49wt.% SiO_2, and 17vol.% crystals. The primary concentration of volatiles in the intruding magma is varied between 2.5 and 8.0wt.% for H_2O and 50 and 5000ppm for CO_2. The chamber radius is adjusted from 0.5-3km, and the degassing rate varies from 0.001 to 3 yr^{-1}. The mass flux of volatiles is constrained with the penalty function as described above.

The forward model requires that during inflation the magma intrusion must satisfy the volume change estimate from GPS, but during deflation the volume change estimate is the result of a combination of degassing and intrusion. There are three general cases that occur during deflation: 1) the excess volatiles bleed off while magma ceases to enter the shallow chamber and the degassing rate exactly matches the deflation rate, 2) the

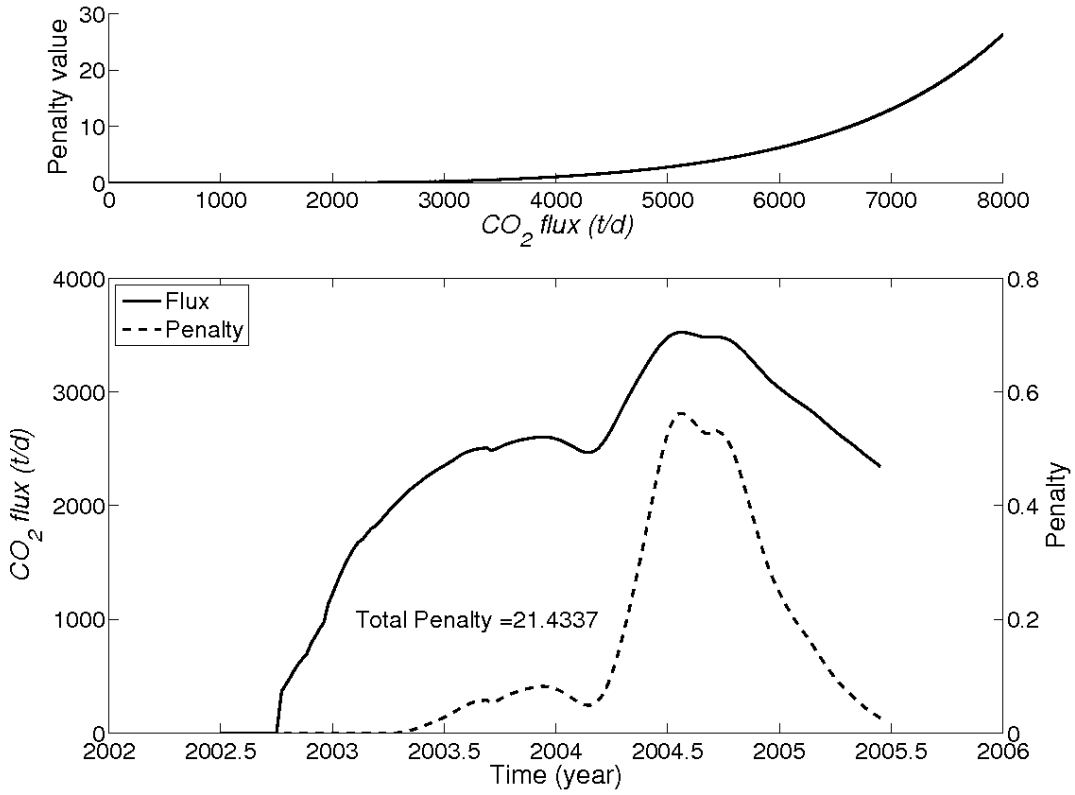

Figure 3.5: The penalty function is used to demote models with excessively high CO_2 mass fluxes. The top panel shows the penalty function. The bottom panel shows an example of how the penalty is applied. The CO_2 flux determined from the model is converted into a penalty value and all of the penalties are summed to come up with the total penalty which is added to the χ^2 value for the purpose of ranking the models.

degassing is too slow to account for the observed deflation, or 3) excess volatiles bleed off much faster than the deflation rate and the excess deflation is compensated by additional magma intrusion. Situations 1 and 3 result in very low χ^2 values, but case 3 often results in a large penalty because the flux of volatiles has the tendency to exceed the critical flux value.

Magma with primary CO_2 content above 1000ppm produces unrealistic mass fluxes and is not considered viable (Fig. 3.6). This suggests that magma intruding into the shallow chamber at Okmok has spent some residence in the crust, long enough for the vapor to equilibrate with the pressure regime. The models explored suggest that the CO_2 concentration of Okmok magmas contain less than ~500ppm prior to entering the shallow chamber.

The water content of the magma is not constrained very well, but there is a clear dependence of H_2O concentration on the CO_2 content in the magma (Fig 3.7). Low concentrations of H_2O require low CO_2 concentrations, in fact at 500ppm CO_2, models with H_2O concentration below ~4wt.% have high overall scores. With lower amounts of CO_2 almost any concentration of H_2O is allowable.

Larger magma chambers (> 2km) require more volatile rich magmas to be able to match the observed deflation rate, but they are excluded because they produce unrealistic CO_2 fluxes. Smaller chambers (< 1km) instead are sensitive to the CO_2 content and the degassing rate. Small chambers with high degassing rates require that the CO_2 level in the intruding magma be below 400ppm. Even with a slower degassing rate a small chamber will exceed the mass flux with CO_2 concentrations above 500ppm. One reason smaller chambers exceed the CO_2 flux limit is that relative to larger chambers the degassing rate must be higher in order to match the deflation trend. This results in high fluxes unless the CO_2 concentration is low.

Chambers between 1 and 2 km radius match the deflation trend with degassing rates between 0.1 and 1 yr^{-1}, with the optimal degassing rate in the range 0.5-0.8 yr^{-1} (Fig. 3.8) These chamber sizes are more sensitive to the water content in the magma. They

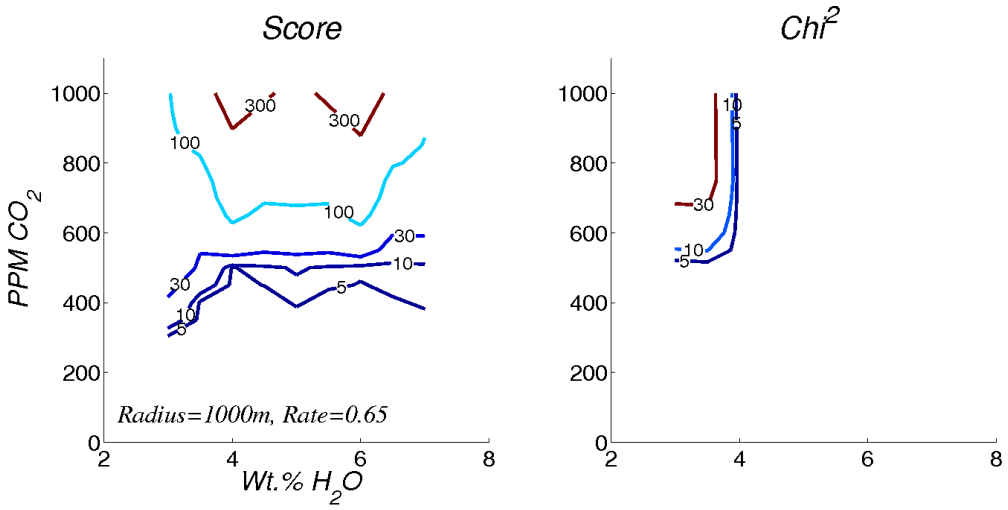

Figure 3.6: The results from the fixed radius and degassing rate models are summarized in the contour plot. The χ^2 and total score values are contoured for models with a radius of 1km and a degassing rate of 0.65yr^{-1}. Together the two contour plots are useful in assessing how well the models fit the data. The χ^2 plot (right) shows that almost any volatile concentration fits the volume change data exceptionally well, but the overall score (left) indicates that unless the CO_2 concentration is below ~500ppm these models result in an excessive flux of CO_2. Both χ^2 and score values are unit-less. Models with χ^2 or score less than ~30 or less are acceptable models.

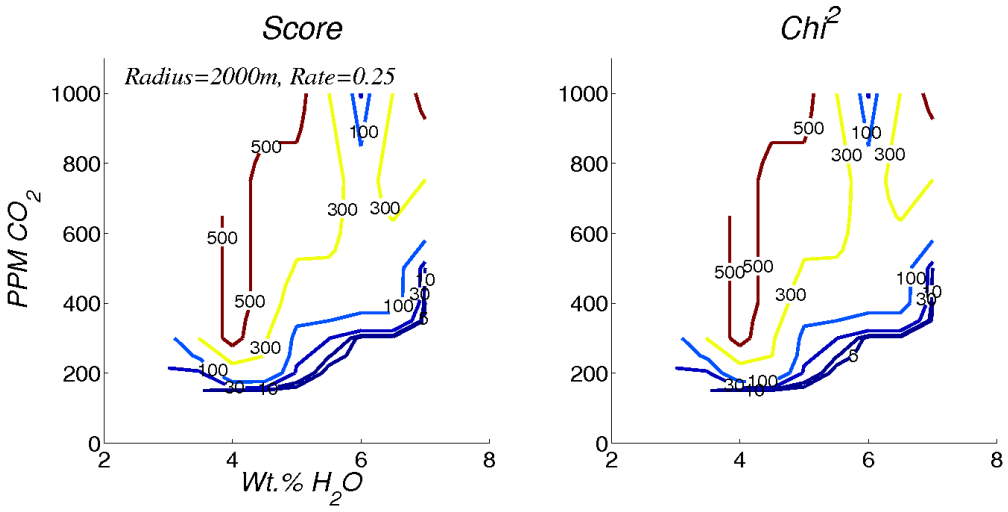

Figure 3.7: The results from the fixed radius and degassing rate models are summarized in the contour plot. The χ^2 and total score values are contoured for models with a radius of 2km and a degassing rate of 0.25yr^{-1}. Together the two contour plots are useful in assessing how well the models fit the data. The χ^2 plot (right) shows that for this chamber size, only high H_2O and low CO_2 concentrations adequately describe the data. For very low CO_2 concentrations (< 200-300ppm) any amount of H_2O above 2.5wt.% fit the data. The overall score (left) is the same as the χ^2, indicating that these models predict CO_2 fluxes that are below 2000 tons/day. Both χ^2 and score values are unit-less. Models with χ^2 or score less than ~30 or less are acceptable models.

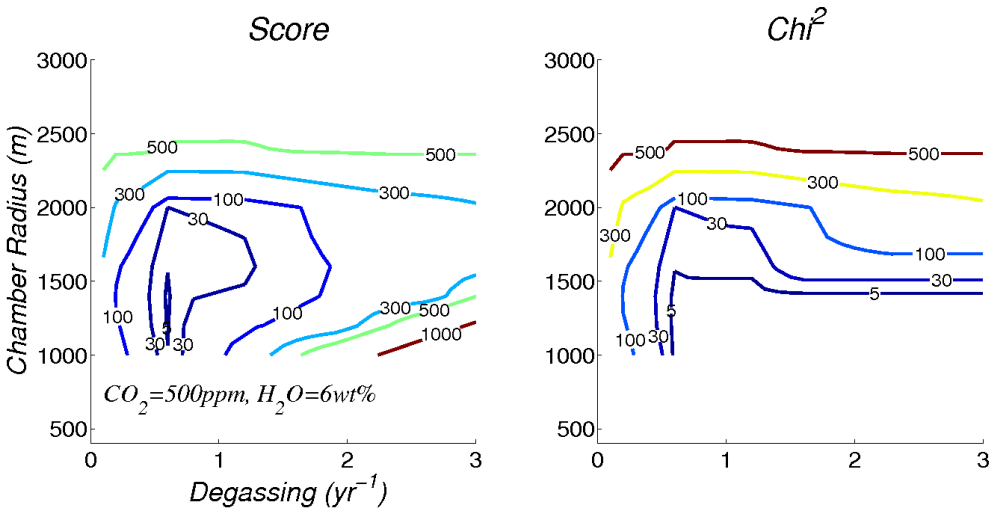

Figure 3.8: The results from the fixed volatile content models are summarized in the contour plot. The χ^2 and total score values are contoured for models with volatile concentrations of 500ppm CO_2 and 6wt.% H_2O. Together the two contour plots are useful in assessing how well the models fit the data. The χ^2 plot (right) shows that for magma with this volatile content, magma chambers must be less than ~2km in radius, and that a degassing rate greater than ~0.5yr^{-1} is adequate to fit the data. The overall score (left) indicates that the high degassing rates result in exorbitant CO_2 fluxes. The result is that chamber sizes in the range ~1-2km and degassing rates between 0.5 and 1yr^{-1} best fit the data. Both χ^2 and score values are unitless. Models with χ^2 or score less than ~30 or less are acceptable models.

also require low CO_2 concentrations (< 600ppm for ~7wt.% H_2O) with the amount of CO_2 decreasing with the H_2O content (Fig. 3.7). Models with high degassing rates often fit the geodetic volume estimates, but produce unrealistic mass fluxes. Together the χ^2 value and the penalty value are effective at limiting the results to models that can describe the geodetic volume estimates and match the expected CO_2 flux from observations of various magmatic intrusions.

Since the purpose of this model is to examine how degassing may contribute to deflation following magma intrusion, we do not attempt to examine the effects that the initial volatile content of the magma chamber has on the deformation.

3.10 Discussion

The numerical experiments show that degassing can account for the deflation observed in the GPS record. If the model assumptions are taken to be valid, then the analysis also provides some constraints on the magma system. The contour plots in Figures 3.6-3.8 show that the relationships between volatile content, magma chamber size and degassing rate are not simple. But, generally a chamber with a radius between 1 and 2km and magma with a CO_2 concentration below 500ppm are required to fit the observations.

The limits on magma chamber size agree with tomographic studies of Okmok which show a low velocity region ~1-2km in radius beneath the caldera [*Haney et al. in prep., 2008*]. The tomography results indicate the maximum extent of the magma chamber, because seismic velocity can be perturbed by factors, such as elevated temperature, which extend beyond a region of melt.

The magma chamber volumes determined with this method can be used to examine the possible range of internal pressure change. Using the relationships in section 3.6 a chamber with a 1km radius would require a pressure change of 180 MPa to produce the maximum uplift observed. A 2km chamber would only require a 20 MPa pressure change. These pressure change estimates are directly related to the assumed value of the host rock shear modulus, a stiff host rock requires larger pressure to produce a unit of

surface deformation. The large pressure change required in the 1km radius case may be the result of over-estimating the shear modulus, or it may indicate that smaller chambers are not realistic based on the internal pressure changes that are required to match the observations. In any case the predicted pressure changes highlight the need for future iterations of this model to account for the internal pressure when calculating the solution dynamics of the magma.

Although the model here does assume an ellipsoidal chamber (*e.g.*, equation 3.4) and uses a spherical chamber in the calculations, the degassing model is really only sensitive to the mass of magma available in the chamber. Any ellipsoidal chamber with a volume equivalent to the spherical chamber used in the model will produce similar results. The behavior of degassing from different types of ellipsoidal chambers might be different. For example, a prolate magma chamber may degas at a lower rate than an oblate chamber; the roof of an oblate chamber having a larger surface area for gases to escape through. Also, for the large chamber sizes modeled here, a spherical chamber at 3km depth is probably not realistic. However, a flattened chamber of equal volume could be considered.

The mass intrusion into the shallow chamber ultimately is ~10% of the initial chamber mass, assuming a 1-2km chamber radius. The intrusion mass, like the other predictable parameters, is dependent on the initialized parameters. The mass of the intrusion ultimately is dependent on the compressibility of the magma which in large part is dependent on the H_2O content of the intruding magma. Magma chambers filled with lots of exsolved H_2O can accommodate a larger intrusion mass by compressing the exsolved gases.

The model presented here explores first order effects of volatile solubility on surface deformation. Many details of the process have been simplified or ignored. For example, the degassing rate parameter used in this study describes how efficiently gases move from the magma chamber to the atmosphere. A more realistic model may take into account the bubble rise rate, permeability of the overburden and the pressure gradient

along the path. Since these are difficult parameters to constrain and the model proposed is already lacking some hard constraints, these details have been simplified as much as possible.

Anecdotal evidence for vigorous degassing comes from field parties who visited the volcano in the summers between 2000 and 2005. Incandescence seen in the vent at Cone A in 2004 [*C. Neal personal communication*] is the strongest evidence for an abundance of hot gases exiting from this vent. Unfortunately the observations are not consistent enough to make inferences about the relative changes or magnitude of the degassing during this time period.

Degassing, gas flow and gaseous magma can all be sources of seismic tremor under proper circumstances [*DeAngelis and McNutt, 2007*]. The seismic network at Okmok has recorded tremor from the time the network was installed to 2005, during the same time as the active deformation periods [*Reyes and McNutt, 2003*]. The tremor may indicate active degassing processes, such as bubble coalescence or circulation of magma in an open conduit. Besides the deflation recorded by GPS and InSAR, the seismic tremor may be the only other record of the degassing processes at Okmok. Although it is beyond the scope of this study, investigation of the seismic record may reveal further details of the degassing process.

These results, combined with work from others, provide a conceptual model for the subvolcanic system at Okmok Volcano. Figure 3.8 displays some of these results. Geodetic modeling [*Miyagi et al., 2004; Lu et al., 2005; Fournier et al., 2008, Chp. 2*] and petrologic studies [*Izbekov et al., 2005*] indicate a magma storage region ~3km below the caldera center. The input of magma into this chamber occurs quasi-periodically, from the pulse like nature of inflation [*Fournier et al. in review; Chp. 2*], but the longer term trend suggests a relatively continuous influx of magma [*Lu et al., 2005*]. A network of faults and fractures dissects the region above and surrounding the chamber [*Walter and Troll, 2001*]. These fractures, as well as dikes and open path ways to existing vents,

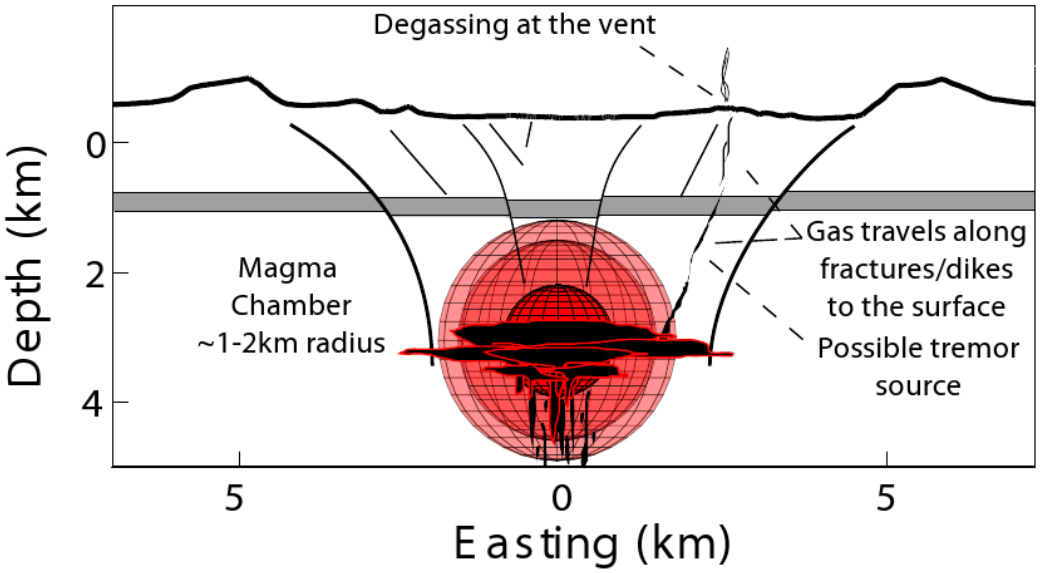

Figure 3.9: A conceptual model of the volcanic system at Okmok Volcano is created from observations at Okmok and volcanic systems world wide. Geodetic observations and the degassing model indicate a spherical chamber at 3km depth and roughly 1-2km in radius. The spherical chambers used in the modeling may be a representation of the more geologically acceptable sill like structure for magma storage. The gray unit is meant to show subsidence that has occurred on inferred faults inside the caldera. Gasses travel to the surface through fractures. Large dikes may allow magma circulation and could be a likely source for seismic tremor.

provide channels for gas to travel to the surface. Some dikes may be large enough to allow magma circulation that would provide an efficient mechanism for degassing. Such dikes are not apparent in the geodetic observations, but without changes to the internal pressure of dike, detecting them geodetically would not be possible. Degassing processes inside such a feature would be a likely source for the seismic tremor observed at Okmok Volcano [*Reyes and McNutt, 2003*].

Compressibility plays an important role in the intrusion dynamics. The compressibility moderates the amount of magma that enters the chamber. If a stiff magma is occupying the chamber, the intrusion volume will be much smaller than if a highly compliant magma is in the chamber, for an equivalent surface deformation. The compressibility of the magma is determined in large part by the amount of volatiles that are in the chamber. In the model presented here this means that when a magma chamber becomes enriched in exsolved volatiles the intrusion volumes remain high and sustain the transport of more volatiles into the chamber. For the models presented here the compressibility falls in the range $0.8\text{-}100\text{x}10^{-10}$ Pa^{-1}, where the smaller value represents magma without exsolved vapor.

This model only explores the end member situation where degassing is the only source of deflation. In reality many processes may be happening at once, and the observed deformation is the superposition of all of them. The model shows that for the shallow chamber at Okmok, degassing can and likely does play a significant role in the deformation signal.

3.11 Conclusions

A degassing model is proposed to explain the deflation signals observed at Okmok Volcano. Relatively small deflation signals are preceded by strong inflation pulses and we propose that the loss of the gas phase from the magma accounts for the deflation. In the model volatiles are supplied to the shallow chamber by intrusion of magma from depth. At lower pressure, the gases exsolve from the magma and escape to the atmosphere causing deflation.

This hypothesis is tested by examining how well the model accounts for the observed deflation signal at Okmok Volcano using various magma compositions, degassing rates and chamber sizes. There are certain conditions in which the model can describe the data. For the most part a magma chamber between 1 and 2km in radius and magma with less than 500ppm CO_2 can adequately explain the data. Acceptable degassing rates fall in the range 0.1-1.0 yr^{-1}. These values are in agreement with observations from Okmok Volcano including a tomographic study which shows a low velocity region approximately 1-2km in extent beneath Okmok.

Anecdotal evidence of degassing exists in the form of field observations and tremor recorded by the seismic network. Further examination of the seismic record may find that the tremor is associated with degassing and the seismicity may provide additional constraints for the type of examination presented here. The deformation data show that degassing is a likely mechanism for the deflation signal. Although the analysis does not put definitive numbers on parameters it certainly provides constraints that are not possible with geodetic data alone. Further constraints could come from gas flux measurements or better estimates of the volatile content of the parent magma.

Future observations at Okmok Volcano will help to constrain this model, and conversely additional constraints can be used along with continued geodetic observations to provide better estimates of intrusion masses. Improved constraints on the volatile content of the intruding magma will assist in narrowing down acceptable values for the other parameters. A thorough investigation of degassing mechanics may narrow the range of degassing rates used. Measurements of gas flux at Okmok would validate, or perhaps force a revision, to the penalty function that is used here. Mechanical models linking seismic tremor to degassing may be able to constrain degassing rates or flux, which could assist analyzing any past deformation episodes that occurred while the seismic network was in operation.

3.12 References

Alut et al., 1965

Aiuppa, A., C. Federico, G. Giudice, S. Gurrieri, M. Liuzzo, H. Shinohara, R. Favara, and M. Valenza (2006), Rates of carbon dioxide plume degassing from Mount Etna volcano, *J. Geophys. Res*., 111, B09207, doi:10.1029/2006JB004307.

Battaglia, M., C. Troise, F. Obrizzo, F. Pingue, and G. De Natale, (2006), Evidence for fluid migration as the source of deformation at Campi Flegrei caldera (Italy), *Geophys. Res. Lett.*, 33, L01307, doi:10.1029/2005GL024904.

Begét, J., J. Larsen, C. Neal, C. Nye, and J. Schaefer, (2005), Preliminary Volcano-Hazard Assessment for Okmok Volcano, Umnak Island Alaska, *Alaska Department of Natural Resources Division of Geological & Geophysical Surveys, Report of Investigations 2004-3.*

Blewitt, G., (1989), Carrier phase ambiguity resolution for the Global Positioning System applied to geodetic baselines up to 2000 km, *J. Geophys. Res*., 94(B8), 10187-10203, doi:10.1029/89JB00484.

Bower, S., and A. Woods, (1997) Control of magma volatile content and chamber depth on the mass erupted during explosive volcanic eruptions, *J. Geophys. Res*., 102(B5), p. 10,273-10,290.

DeAngelis, S., and McNutt, S.R., (2007), Observations of volcanic tremor during the January-February 2005 eruption of Mt. Veniaminof, Alaska, *Bulletin of Volcanology*, v. 69, p. 927-940, doi:10.1007/s00445-007-0119-4.

Delany, P., and D. McTigue, (1994), Volume of magma accumulation or withdrawal estimated from surface uplift or subsidence, with application to the 1960 collapse of Kilauea Volcano, *Bulletin of Volcanology*, vol. 56, pp.417-424.

de Zeeuw-van Dalfsen, E., H. Rymer, F. Sigmundsson, and E. Sturkell, (2005), Net gravity decrease at Askja volcano, Iceland: constraints on processes responsible for continuous caldera deflation, 1988–2003, *Journal of Volcanology and Geothermal Research*, 139, p. 227-239, doi:10.1016/j.jvolgeores.2004.08.008.

Doukas, M., (1995), A compilation of sulfur dioxide and carbon dioxide emission-rate data from Cook Inlet volcanoes (Redoubt, Spurr, Iliamna, and Augustine), Alaska during the period from 1990 to 1994, *U.S. Geological Survey Open-File Report 95-55*, 16p, available at http://pubs.er.usgs.gov/usgspubs/ofr/ofr9555.

Doukas, M., and K. McGee, (2007), A compilation of gas emission-rate data from volcanoes of Cook Inlet (Spurr, Crater Peak, Redoubt, Iliamna, and Augustine) and Alaska Peninsula (Douglas, Fourpeaked, Griggs, Mageik, Martin, Peulik, Ukinrek Maars, and Veniaminof), Alaska, from 1995-2006: *U.S. Geological Survey Open-File Report 2007-1400*, 13 p., available at http://pubs.usgs.gov/of/2007/1400/

Dvorak, J., and D. Dzurisin, (1997), Volcano geodesy: The search for magma reservoirs and the formation of eruptive vents, *Rev. Geophys.,* 35, 343– 384.

Finney, B., S. Turner, C. Hawkesworth, J. Larsen, C. Nye, R. George, I. Bindeman, and J. Eichelberger, (2008), Magmatic differentiation at an island-arc caldera: Okmok Volcano, Aleutian Islands, Alaska, *Journal of Petrology*, 49, 857-884, doi:10.1093/petrology/egn008.

Fournier, T., J. Freymueller, and P. Cervelli, (2008), Tracking magma volume recovery at Okmok Volcano using GPS and an Unscented Kalman Filter, *J. Geophys. Res.*, doi:10.1029/2008JB005837R.

Gottsmann, J., A. Folch, and H. Rymer, (2006), Unrest at Campi Flegrei: A contribution to the magmatic versus hydrothermal debate from inverse and finite element modeling, *J. Geophys. Res.*, 111, B07203, doi:10.1029/2005JB003745.

Grey, D., (2003), Post-caldera eruptions at Okmok volcano, Umnak Island, Alaska, with emphasis on recent eruptions from Cone A., M.S. thesis, Univ. of Alaska, Fairbanks, Dec.

Haney, M., …

Izbekov, P., J. Larsen, and J. Gardner, (2005), Pertrological and experimental constraints on the recent magma plumbing system at Okmok Volcano, Alaksa, USA, *EOS Trans., Fall Meet. Suppl.*, V13B-0533.

Johnson , D., (1987), Elastic and inelastic magma storage at Kilauea Volcano, Volcanism in Hawaii, edited by R. Decker, T. Wright and P. Stauffer, *USGS Professional Paper 1350,* p. 1297-1306.

Johnson, D. J., F. Sigmundsson, and P. T. Delaney, (2000), Comment on "Volume of magma accumulation or withdrawal estimated from surface uplift or subsidence, with application to the 1960 collapse of Kilauea volcano" by P. T. Delaney and D. F. McTigue, *Bulletin of Volcanology,* vol. 61, pp. 491-493.

Larsen, J., C. Neal, J. Schaefer, J. Begét, and C. Nye, (2007), Late Pleistocene and Holocene caldera-forming eruptions of Okmok Caldera, Aleutian Islands, Alaska, *Volcanism and Subduction: The Kamchatka Region, Geophysical Monograph Series 172*, p. 343364, doi:10.1029/172GM24

Lu, Z., T. Masterlark, and D. Dzurisin, (2005), Interferometric synthetic aperture radar study of Okmok volcano, Alaksa, 1992-2003: Magma supply dynamics and postemplacement lava flow deformation, *J. Geophys. Res.*, 110, B02403, doi:10.1029/2004JB003148.

Lu, Z., D. Mann, J. Freymueller, and D. Meyer, (2000), Synthetic aperture radar interferometry of Okmok volcano, Alaska: Radar observations, *J. Geophys. Res.*, 105, pp. 10,791-10,806.

Mann D., J. Freymueller, and Z. Lu, (2002), Deformation associated with the 1997 eruption of Okmok volcano, Alaska, *J. Geophys. Res.*, 107, doi:10.1029/2001JB000163.

Miller, T., R. McGimsey, D. Richter, J. Riehle, C. Nye, M. Yount, and J. Dumoulin, (1998), Catalog of the historically active volcanoes of Alaska, *U.S. Geol. Surv. Open File Rep*., 98-0582.

Miyagi Y., J. Freymueller, F. Kimata, T. Sato, and D. Mann, (2004), Surface deformation caused by shallow magmatic activity at Okmok volcano, Alaska, detected by GPS campaigns 2000-2002, *Earth Planets Space*, 56, pp. 29-32.

Mogi, K., (1958), Relations between the eruptions of various volcanoes and the deformations of the ground surfaces around them, *Bulletin of the Earthquake Research Institute*, vol. 25, pp. 99-134.

National Oceanic and Atmospheric Administration, (2008), National Geodetic Survey, GPS Antenna Calibration, http://www.ngs.noaa.gov/ANTCAL, last access, Dec. 2008.

Newman, S., and J. Lowenstern, (2002), VolatileCalc: a silicate melt-H2O-CO2 solution model written in Visual Basic for Excel, *Computers and Geosciences*, 28, 597-604.

Niell, A., (1996), Global mapping functions for the atmosphere delay at radio wavelengths, *J. Geophys. Res.*, 101, 3227-3246.

Papale, P. (2005), Determination of total H2O and CO2 budgets in evolving magmas from melt inclusion data, *J. Geophys.Res.*, 110, B03208, doi:10.1029/2004JB003033.

Power, J., (2004), Renewed Unrest at Mount Spurr Volcano, Alaska, *Eos Trans. AGU*, 85(43), doi:10.1029/2004EO430004.

Reyes, C., and S. McNutt, (2003), Quasi-periodic episodes of volcanic tremor at *Okmok* Volcano, Alaska, *Eos, Transactions, American Geophysical Union***,** vol. 84, no. 46, Suppl., Abstract V31B-03**.**

Rivalta, E., and P. Segall, (2008), Magma compressibility and the missing source for some dike intrusions, *Geophys. Res. Lett.*, 35, L04306, doi:10.1029/2007GL032521.

Roman, D. C., J. A. Power, S. C. Moran, K. V. Cashman, M. P. Doukas, C. A. Neal, and T. M. Gerlach, (2004), Evidence for dike emplacement beneath Iliamna Volcano,

Alaska in 1996: *Journal of Volcanology and Geothermal Research*, v. 130, n. 3-4, p. 265-284, doi:10.1016/S0377-0273(03)00302-0.

Sigmundsson, F., P. Einarsson, and R. Bilham, (1992), Magma chamber deflation recorded by the Global Positioning System: The Hekla 1991 eruption, *Geophys. Res. Lett.*, 19, pp. 1483-1486.

Sisson, T., and C. Bacon, (1999), Gas-driven filter pressing in magmas, *Geology,* July 1999, v. 27, no. 7, p. 613–616.

Wallace, P., (2005), Volatiles in subduction zone magmas: concentrations and fluxes based on melt inclusion and volcanic gas data, *Journal of Volcanology and Geothermal Research*, 140, 217-240, doi:101016/j.jvolgeores.204.07.023

Walter, T., and V. Troll, (2001), Formation of caldera periphery faults; an experimental study, *Bull. Volcanology*, 63, 191-203, doi:10.1007/s004450100135.

Zumberge, J., M. Heflin, D. Jefferson, M. Watkins, and F. Webb, (1997), Precise point positioning for the efficient and robust analysis of GPS data from large networks, *Journal of Geophysical Research*, v. 102, p. 5005-5017.

Chapter 4: Transition from locked to creeping subduction in the Shumagin Region, Alaska[2]

4.1 Abstract

GPS velocities from the Alaska Peninsula are modeled to determine the extent of locking on the Alaska-Aleutian subduction interface. The observations, which span from the Semidi Islands to Sanak Island, encompass the 1938, M_w 8.3, rupture zone and the transition into the Shumagin gap. Model parameters are optimized using a simulated annealing method. Coupling variation along strike of the plate interface show a nearly fully locked (90%) subduction zone at the Semidi Islands, decreasing to about 30% locked at the Shumagin Islands, and freely slipping to the west of the Shumagins. Independent rupture of the Shumagin segment could produce repeated M_w 7.6 earthquakes, unless a significant fraction of the slip on the interface occurs as afterslip following large earthquakes. Southwest directed velocities at most of the sites may be attributed to clockwise rotation of a Bering block.

4.2 Introduction

Subduction zone earthquakes are a major hazard for coastal populations both near and far from the epicenter, due to severe ground shaking and the potential to generate tsunamis. *Pacheco et al.* (*1993*) showed that seismic release at subduction zones varies worldwide. Identifying regions with low and high potential for sources of large subduction earthquakes is important for advancing our understanding of subduction zone seismicity, and local and regional hazards. Geodetic observations can be used to study the process of interseismic loading, and estimate the rate of slip deficit or moment deficit on the plate interface.

The Shumagin segment of the Alaska-Aleutian subduction zone (Figure 4.1) has not experienced a large earthquake that has ruptured the majority of the plate interface

[2] Fournier, T. J., and J. T. Freymueller, (2007), Transition from locked to creeping subduction in the Shumagin region, Alaska, *Geophys. Res. Lett.*, 34, L06303, doi:10.1029/2006GL029073.

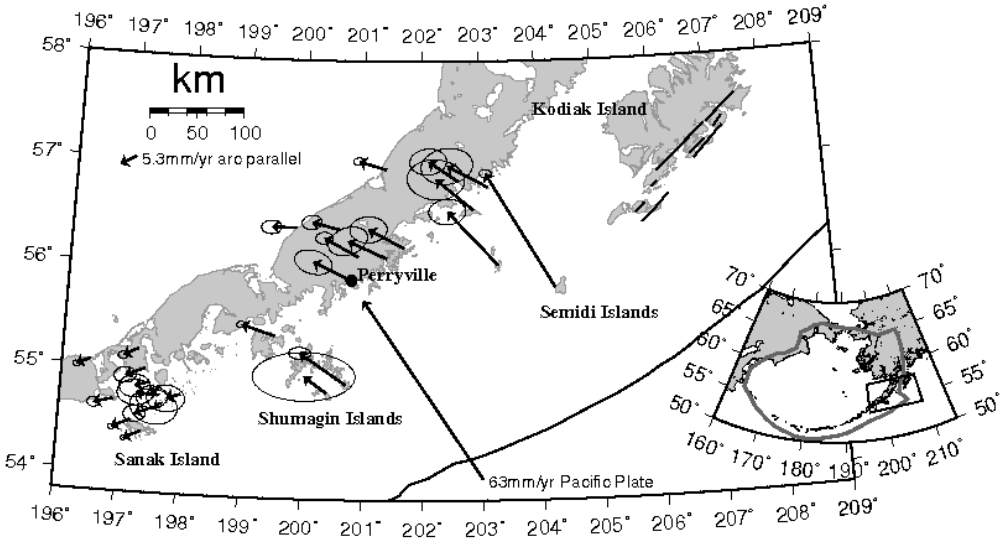

Figure 4.1: GPS station velocities along the Alaska Peninsula, relative to North America. The Bering Block proposed by *Mackey et al.* (*1997*) is the bold line in the inset map, with a rectangle outlining the region shown in detail. The black vectors show the observed velocity at each site, with 95% confidence ellipses. The convergence rate of the Pacific plate and the North American plate, from REVEL (*Sella et al., 2002*), is shown at the approximate coordinate for which it was determined. The arc velocity that is applied as a correction to the modeled data (see text) is shown at the upper left. Left-lateral faults on Kodiak Island and the Aleutian trench are shown as black lines.

since at least 1917, when an M_s 7.4 (*Estabrook and Boyd, 1992*) earthquake struck the region. That quake may have ruptured from the eastern edge of the Shumagins to somewhere west of the Shumagin Islands, but not as far as Sanak Island (*Boyd et al., 1988*). Other moderate sized earthquakes have been attributed to rupturing a portion of the plate interface in the Shumagin segment, including an M_s 7.5 in 1948 and an M_s 7.1 in 1993 (*Bufe et al., 1994*). No great earthquakes are known to have occurred in the Shumagin segment, and no large earthquakes are known from the western portion of the Shumagin segment.

Fletcher et al. (*2001*) used a single plane model to examine the plate coupling (slip deficit) along the Semidi segment (Figure 4.1). They determined that the interface in this region is presently ~80% coupled, that is, that the area of their 170 –km-wide model plane on average slips at about 20% of the plate motion rate and thus has a slip deficit accumulating at a rate of 80% of the plate motion rate. Farther to the southwest along the subduction zone, near Sanak Island, the plates are freely slipping (*Freymueller and Beavan, 1999*). The transition from the very wide, highly coupled zone in the north to the weakly coupled zone to the south occurs over a fairly small region surrounding the Shumagin Islands.

Here we construct a model that explains the GPS observations along the Alaska Peninsula and offshore islands, and examine this zone of transition from a very wide locked zone on the plate interface, which has historically generated great earthquakes, to a freely-slipping segment that has no record of great earthquakes. We then interpret patterns of thrust-zone seismicity in the area in relation to the inferred locked and creeping segments along the subduction zone.

4.3 Data

We use three component GPS velocities from 27 sites along the Alaska Peninsula, surveyed between 1991 and 2005 (Figure 4.1, Table 4.1). Most of the data were collected during 1993-1996, and subsets of the data set were used earlier by *Freymueller and Beavan* (*1999*) and *Fletcher et al.* (*2001*). However, new observations

Table 4.1: Alaska Peninsula GPS station locations and velocities (mm/yr) relative to North America. The ±1σ uncertainties are shown for the east, north and vertical components. The last two columns show the time span of the observations and the number of surveys at each site.

Station	Longitude	Latitude	East	North	Vertical	σ_e	σ_n	σ_v	Time (yr)	# of Surveys
ASPE	-157.37	56.85	-8.6	5.9	-3.0	2.2	1.6	4.5	2	2
CHIR	-155.73	55.83	-19.6	34.1	-11.1	0.7	0.5	1.4	4	3
CLFF	-158.30	56.21	-10.6	5.6	-6.6	2.2	1.6	4.6	2	2
HEID	-158.61	56.96	-8.2	2.5	2.8	0.6	0.5	1.2	5	4
HUEY	-156.86	56.79	-11.8	6.4	4.5	3.1	2.2	5.5	2	2
SEMI	-156.69	56.05	-14.7	16.0	6.7	2.2	1.5	4.4	2	2
WIK	-157.11	56.58	-10.9	9.2	1.9	3.4	2.4	6.2	2	2
STAR	-159.17	55.89	-11.8	5.6	6.1	2.2	1.5	4.2	14	3
SENI	-160.14	56.40	-7.6	0.0	5.7	1.2	0.8	2.4	3	2
ISLK	-158.60	56.11	-11.5	5.2	-3.3	2.3	1.7	5.3	5	2
YAST	-159.42	56.39	-8.0	2.1	3.7	1.2	0.9	2.5	3	2
VSG	-159.09	56.12	-10.1	5.6	1.2	1.0	0.7	2.1	3	2
SNDP	-160.48	55.35	-9.8	3.2	0.8	0.5	0.4	0.9	12	4
SMNF	-159.27	54.90	-13.6	9.3	-2.7	1.3	0.7	2.1	8	3
CHRN	-162.37	54.63	-6.6	2.5	1.3	1.3	1.0	2.8	3	3
CHNB	-159.58	54.81	-6.8	4.9	-0.9	6.2	2.9	8.5	4	3
CROW	-162.80	54.49	-5.5	2.5	3.9	0.4	0.3	0.7	11	4
DAY	-162.47	54.74	-4.8	0.5	1.8	2.2	1.5	4.3	2	2
FAWN	-162.36	54.82	-2.0	-3.4	2.8	1.9	1.3	3.9	3	3
KATY	-163.52	55.04	-4.1	-1.8	0.0	0.4	0.3	0.8	8	7
LAG	-162.30	54.66	-2.3	-1.3	1.8	2.9	2.1	6.0	2	2
LONE	-162.00	54.76	-4.3	-1.4	2.3	2.3	1.6	4.6	2	2
PANK	-163.11	54.68	-5.5	-1.4	4.3	0.8	0.6	1.6	6	4
PETE	-162.62	54.38	-5.0	-2.3	2.3	0.3	0.3	0.5	11	4
REEF	-162.52	54.86	-4.2	-1.4	3.2	1.9	1.4	3.9	3	3
SATT	-162.73	55.17	-4.5	-2.4	1.2	0.6	0.5	1.2	6	5
TELE	-162.60	54.98	-5.8	-2.2	1.1	1.3	0.9	2.8	3	3

of several sites were made between 2003 and 2005, so we have new velocities for several sites and much greater precision for others. All phase data have been analyzed along with phase data from surrounding continuous GPS stations using the GIPSY-OASIS GOA4 software, and each daily solution is transformed into the ITRF2000 reference frame (IGSb00 realization). We used the JPL non-fiducial orbits for solutions 1995 and later, but estimated orbits from a global data set for earlier data. The ITRF velocities are then rotated into a North America-fixed reference frame using the REVEL model (*Sella et al., 2002*). A sample time series is shown in Figure 4.2. A few sites have a long history of observations; these velocities have uncertainties of order 0.5 mm/yr, and as shown later, are fit by a model to a similar level of precision. All the surveys were conducted at roughly the same time in the summer; this mitigates the effects of seasonal variations.

There are three obvious features in the data: 1) the velocities are largest closest to the trench and decrease with distance form the trench, the result of convergence of the Pacific and North America plates; 2) sites that are farther east generally have larger velocities, given the same distance from the trench; and 3) sites in the west move in a nearly trench-parallel direction and show little or no variation in velocity with distance from the trench. This results in a clear counter-clockwise rotation in the velocity field with the sites farthest from the trench moving in a more trench-parallel direction than sites closer to the trench. These features can be explained by a combination of a westward translation of all sites combined with along-strike variations in the extent of the locked subduction zone.

We refer to the westward component to all of the data as the arc translation or arc velocity, because it is directed parallel to the arc, as previously noted by *Mann and Freymueller* (*2003*). The arc velocity is 5.3mm/yr directed toward 241˚, based on the average velocity of the sites in the western part of the network. The origin of this motion is not clear, but may have to do with clockwise rotation of a Bering micro-plate (*Mackey et al., 1997*). In this study we approximate block rotation with translation because the size of the network is small compared to the distance to the proposed Bering plate

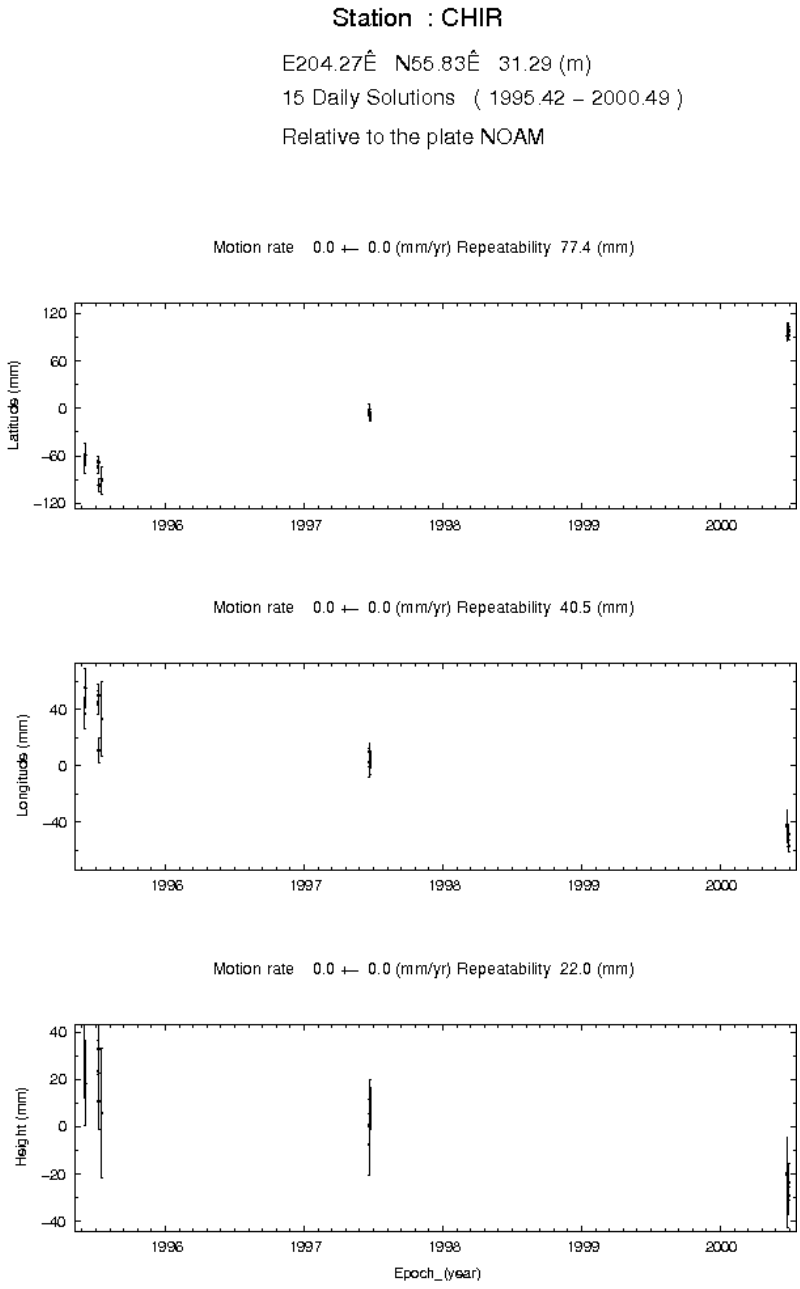

Figure 4.2: Example time series plot of station CHIR, on Chirikof Island Alaska, relative to North America. The data are used to determine site velocities used in the study.

rotation pole. After removal of the arc velocity, all the velocities (except CHIR) are nearly parallel to the Pacific–North America relative plate motion direction, indicating that the counter-clockwise rotation results from the superposition of translation of the Alaska Peninsula relative to North America with strain resulting from the locked subduction zone. Site CHIR on Chirikof Island near the trench (Figure 4.3) does not show this same arc translation. We suggest that a network of active trench parallel, left lateral strike-slip faults on Kodiak Island (*Sauber et al., 2006*) extends to the southwest past Chirikof Island, and passes between Chirikof and the rest of the sites. This fault system may represent the southern limit of the Bering block, or of westward extrusion of southwest Alaska, or it may be related to slip partitioning of oblique subduction that occurs in the western Aleutian subduction zone.

4.4 Methods

We use a simple four plane model to represent the locked portion of the interface. This simple model geometry creates discontinuities in the plate interface, but these are located at sufficient depth, and the model is not sensitive enough to the dip angle, to represent more than a second order effect. Smoother model geometry would be needed, for example, to investigate stress changes near the interface. Although we do not incorporate a transition zone from locked to creeping downdip of the locked zone, we have found that for any model with a transition zone a model with an abrupt transition located at the midpoint of the transition zone produced almost identical surface displacements. The downdip end of the locked zone in our model should be interpreted as the midpoint of the transition from locked to fully creeping, and the downdip transition may be narrow or as wide as ~50 km or perhaps more.

We estimated the optimal model using the simulated annealing technique described by *Cervelli et al.* (*2001*). The model space is loosely constrained based on previous geodetic and seismic studies (*Von Huene et al., 1987; Abers, 1992; Freymueller and Beavan, 1999; Savage et al., 1999; Fletcher et al., 2001, Sauber et al. 2006*). For each plane we determine the length, width, dip and the slip deficit; the planes are

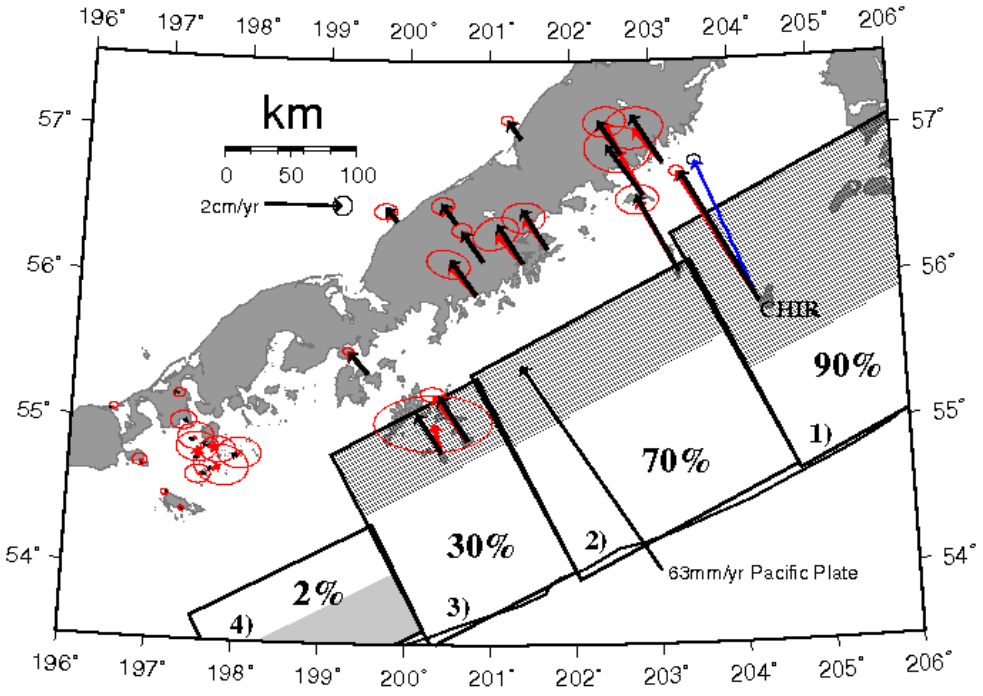

Figure 4.3: Subduction zone model for the eastern Aleutian arc and predicted velocity vectors. Data (red) and model (black) velocity vectors are shown. All of the data have been corrected for arc translation, except CHIR. The blue vector shows the velocity at CHIR if an arc translation correction is applied at that site. The surface projections of the locked interfaces are shown as black rectangles with the amount of coupling shown on each plane as the percentages in black. The planes are numbered according to Table 4.2. For planes 1-3 the locked area of the fault can be decreased to the area of the stipple pattern with the amount of coupling increased to 100%, 80% and 40% respectively. The gray region on interface 4 is the widest possible fully locked interface.

constrained not to overlap or have gaps between them. Each fault plane is represented by a dislocation in a homogeneous elastic half-space (*Okada, 1992*). Deformation is modeled by the superposition of steady slip on the interface at the plate convergence rate with slip deficit represented by backslip on the same interface (*Savage, 1983*). The slip deficit is allowed to vary from 0 to 100 percent of the plate convergence rate, determined from the REVEL plate velocity model (*Sella et al., 2002*).

4.5 Results

Table 4.2 shows the parameter values of the optimal model. This model has locking depths ranging from ~20-30km, which is consistent with previous studies of this area (*Fletcher et al., 2001, Savage and Lisowski, 1986*) and subduction zones in general (*Oleskevich et al., 1999*). The model is not very sensitive to variations in dip, but seismic observations constrain the dip angles to a relatively narrow range. The 10˚-13˚ dip along the western segment agrees with seismicity in the Shumagin area which indicates a dip of 10-15˚ (*Savage and Lisowski, 1986; Abers, 1992; Zheng et al., 1996*). In the Semidi Island region, the results determined here for dip, locking depth and amount of coupling agree well with the model reported by *Fletcher et al.* (*2001*). This is expected, because in this region we have very little new data beyond what they used. At the Shumagin Islands the slip deficit drops to 30% of the plate rate, and then to nearly zero west of the Shumagins. Details of the nature of locking on the interface are not discernable with the data.

We estimated uncertainties through a series of parameter searches centered on the optimal model. We varied parameters independently or together to study tradeoffs, but in all cases only one plane is modified at a time, while the other planes are fixed to the best model values (Table 4.2). We estimated the range of acceptable parameters from the increase in misfit over the optimal model (Figures 4.4 and 4.5). Except for the fault lengths, which cause all faults in the model to shift, varying the parameters for one fault has only a minor effect on the parameters of the others

Table 4.2: The model parameters for each subduction zone segment. The longitude and latitude describe the eastern-most corner of each plane. Depth is the vertical distance to the top and bottom of each plane. The planes are numbered 1-4 from east to west. Parameter uncertainties and tradeoffs are discussed in the text.

Plane	Long.	Lat.	Length (km)	Width (km)	Dip (˚)	Strike (˚E)	Depth (km)		Coupling
							top	base	
#1	-152.241	55.496	217	207	8	60	5	28	90%
#2	-155.342	54.702	189	179	10	61	5	30	70%
#3	-157.993	54.002	125	168	11	62	5	32	30%
#4	-159.777	53.597	155	92	13	63	5	20	2%

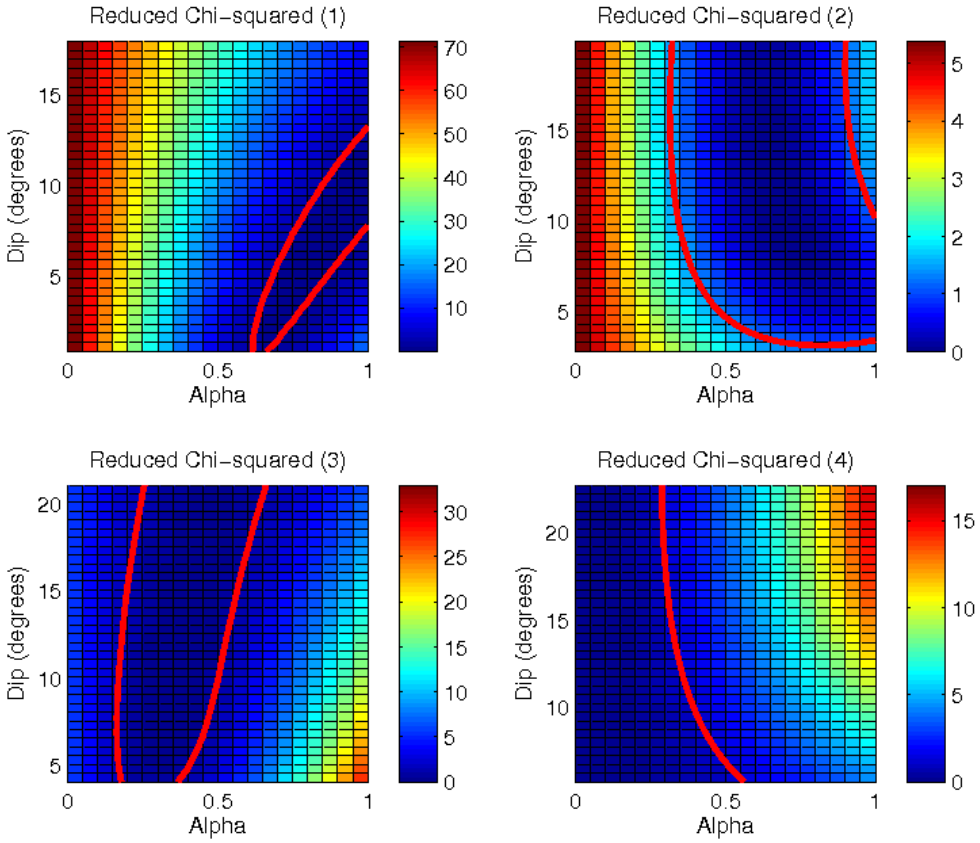

Figure 4.4: Misfit plots of dip vs. slip-deficit for each plane in the modeled subduction interface. The figure shows the reduced-chi-squared values for models with varying dip and parameter alpha. Alpha is a parameterization of slip-deficit where alpha multiplied by the convergence velocity is equal to the slip deficit. The red line in each panel is the 95% confidence contour. Panels 1-4 correspond to the model planes 1-4 described in the text.

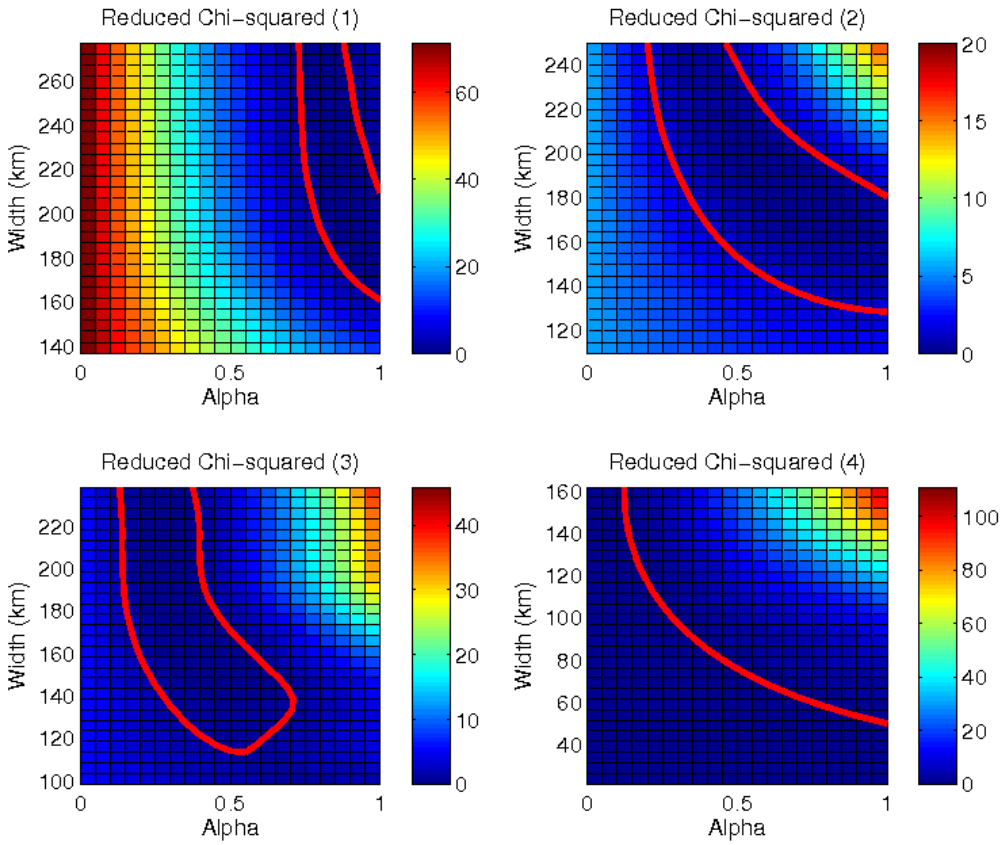

Figure 4.5: Misfit plots of width vs. slip-deficit for each plane in the modeled subduction interface. The figure shows the reduced-chi-squared values for models with varying width and parameter alpha. Alpha is a parameterization of slip-deficit where alpha multiplied by the convergence velocity is equal to the slip deficit. The red line in each panel is the 95% confidence contour. Panels 1-4 correspond to the model planes 1-4 described in the text.

The dip is not very well constrained by the observations (Figure 4.4), but variations in dip have only a modest affect on other parameters. For example if the dip on plane #1 is changed from 5˚ to 12˚, there is a ~20% decrease in the amount of locking on the interface. A comparable change in dip on planes #2 and #3 results in only ~10% change in coupling. Plane #4 has essentially no coupling, so all other parameters for this plane can be varied with no change to misfit, but an increase in coupling increases misfit.

Width and slip deficit show a negative correlation (Figure 4.5). Plane #1 has ±40km uncertainty with a slip deficit of almost 100% locked for the narrower plane to less than 80% locked for the wider plane. The tradeoff is more dramatic for plane #2 where the locking amount decreases from 90% to 50% over the range of widths, 130km to 210km. Plane #3 has a larger width uncertainty, ±70km, than the other planes due to sparse data in this region. Over this range of widths the slip deficit only varies from 30% to 20%. Considering all uncertainties, we estimate the uncertainty in the plate coupling fraction to be ~20%.

Resolution of the state of the plate interface close to the trench is very poor, due to a lack of observations there. The sensitivity of the updip limit of the locked zone was assessed using a grid search in which the depth to the updip edge of the locked zone was increased and the slip deficit was re-estimated. Figure 4.3 shows the narrowest possible downdip locked region, at the 95% confidence level, with a stippled pattern. If planes 1-3 are reduced to their narrowest, the coupling on each plane increases to 100%, 80%, and 40% respectively. This shows that the data are not sensitive to the shallow portion of the plate interface. The top of the locked zone in this case is at 12km, 19km, and 21km depth from east to west respectively.

The western most plane has nearly zero slip deficit, so instead of determining the sensitivity to a shallow creeping zone we determine the data sensitivity to a shallow locked region. The gray box in Figure 4.3 shows the largest fully locked interface that can be allowed within the 95% confidence limits of the data. The downdip edge of this zone is at 11km. *Oleskevich et al.* (*1999*) used thermal modeling to show that in the

Cook Inlet region of Alaska the plate interface probably is not locked shallower than 12km, and if the same is valid for the Sanak region there is probably no locked zone at all.

4.6 Discussion and Conclusions

The model shows a transition from the wide locked zone of the 1938 rupture to the creeping zone south of Sanak (Figure 4.6). The edge between the wide locked zone and the weakly coupled Shumagin segment in the model agrees with the edge of the 1938 rupture zone estimated from the aftershock distribution. Between the 1938 rupture zone and the Sanak segment, the plate interface becomes more dominated by creep. Velocities of sites along the Alaska Peninsula between longitudes 201°E and 202°E show no variation, so the transition from dominantly locked to dominantly creeping (plane 2 to plane 3) must be abrupt, occurring over an along-strike distance that is very small compared to the width of the locked zone. Over a distance of ~50 km SW of the Shumagin islands, the remaining locked regions on the interface disappear.

Past estimates of the extent of the locked region on the plate interface in the Shumagin Islands by *Savage and Lisowski* (*1986*) and *Larson and Lisowski* (*1994*) found a smaller locked zone width than we find here, but they also assumed the slip deficit had to equal the full plate convergence rate. *Zheng et al.* (*1996*) found that 20% coupling worked well to describe the data. Their assumed locked zone extended farther down dip and thus closer to the geodetic network, which has the effect of requiring less coupling to produce the observed strains. Increasing the downdip length of the locked zone and decreasing the amount of slip deficit results in a constant moment deficit, so all of these have similar moment deficit rates. Since both the *Zheng et al. (1996)* and *Savage and Lisowski* (*1986*) models are two dimensional we can compare the yearly energy stored on the length equivalent to the Shumagin segment (plane 3) in the model determined here. Although our model extends the locked interface all the way to the trench, this is a modeling convenience and we have shown that this is not required by the data. Based on the distribution of microseismicity *Zheng et al.* (*1996*) used ~16km for the updip end of

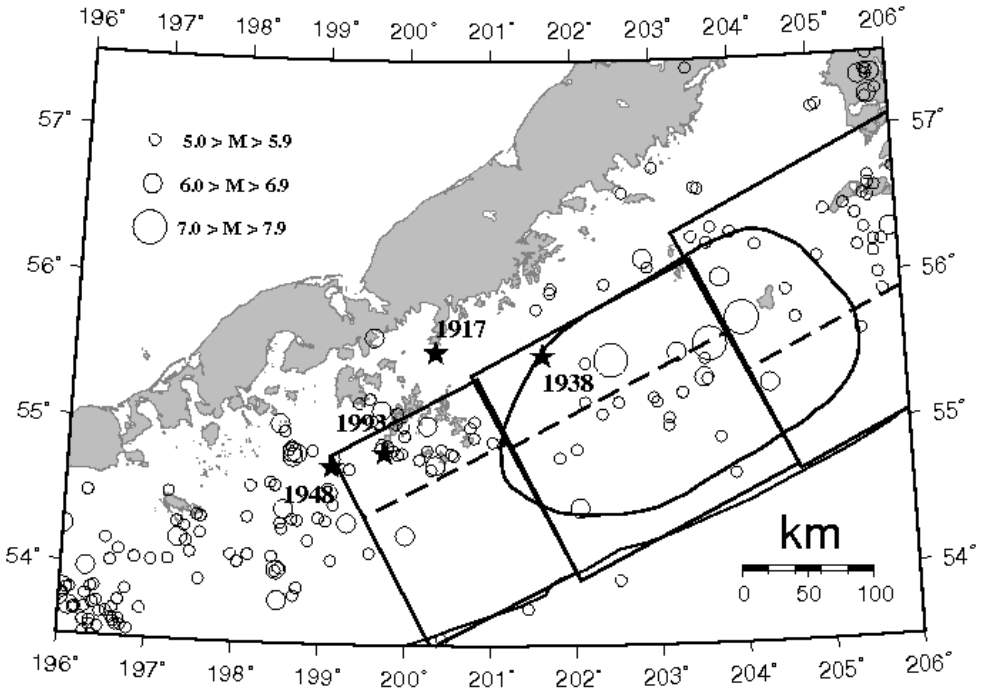

Figure 4.6: The seismicity along the Alaska Peninsula is plotted along with the partially locked interfaces from the model. The dashed lines are the same as in figure 4.3. Events with M≥5.0 and depth < 50 km from the AEIC seismic catalog are plotted as circles. Black stars show significant earthquakes in the region; 1917 M_s 7.4 (*Estabrook and Boyd, 1992*), 1938 M_w 8.3, 1948 M_s 7.5, 1993 M_s 6.9 (*Abers et al., 1995*). The extent of the 1938 rupture is shown as a black outline.

the locked zone. Since this is shallower than the sensitivity limit of our data (21km in this region) and we do not expect that the locked interface extends to the trench, we use 16km as the upper limit to the locked zone. With a rigidity of 3E10 Pa this provides a moment deficit rate of 6.4E18Nm/yr for our model compared to 5.2E18Nm/yr for the *Zheng et al.* (*1996*) model and 9E18Nm/yr for the *Savage and Lisowski* (*1986*) model. In terms of magnitude this amount of energy is equivalent to an Mw 6.47, 6.41 and 6.57 each year, respectively.

Boyd et al. (*1988*) estimated the average recurrence interval for major earthquakes in the Shumagin region to be about 65 years, and *Nishenko and Jacob* (*1990*) estimated 64 years. If the Shumagin plane determined in this model is ruptured every 65 years, this would amount to an average slip of 1.4 m, and would produce roughly an M_w 7.6 quake, which is in agreement with the size and rupture area reported by *Estabrook and Boyd* (*1992*) for the 1917 earthquake. The relatively low average slip deficit, and the occurrence of two M~7 earthquakes in the region since 1917, makes it possible that instead of rupturing in one large earthquake, more frequent moderate earthquakes may be likely. The magnitudes of the 1948 and 1993 earthquakes (M_s 7.5 and M_s 7.1) are roughly consistent with rupture of this entire zone every ~40 years, making up the full moment deficit. In a region characterized by creep, it is also possible that a significant fraction of the slip on the interface may occur as afterslip following large earthquakes, as has been observed for parts of the plate interface in northern Japan (*Heki and Tamura, 1997; Heki et al., 1997; Igarashi et al., 2003*).

The seismicity during the last century and the geodetic observations of the past decade show a similar transition in character from east to west. Figure 4.6 shows Alaska Earthquake Information Center (AEIC) catalog (M>5) events from the last century. In the east the 1938 rupture zone has relatively few earthquakes but does have several large sized shocks and one great earthquake. In the west there are many small earthquakes but no large events. The Shumagin transition zone has a high density of smaller quakes and a

few large tremors. This contrast is similar to that of creeping and non-creeping segments of the San Andreas fault in California (*Wiemer and Wyss, 1997*).

4.7 References

Abers, G., (1992), Relationship between shallow- and intermediate-depth seismicity in the Eastern Aleutian subduction zone, *Geophys. Res. Lett.*, 19, 2019-2022.

Abers, G., J. Beavan, S. Horton, S. Jaumé and E. Triep, (1995), Large accelerations and Tectonic setting of the May 1993 Shumagin Islands earthquake sequence, *Bull. Seismol. Soc. Am.*, 85, 1730-1738.

Boyd, T., J. Taber, A. Lerner-Lam, and J. Beavan, (1988), Seismic rupture and arc segmentation within the Shumagin Island seismic gap, Alaska, *Geophys. Res. Lett.*, 15, 201-204.

Bufe C., S. Nishenko, and D. Varnes, (1994), Seismicity trends and potential for large earthquakes in the Alaska-Aleutian region, *Pure Appl. Geophys.*, 142, 83-99.

Cervelli, P., M. Murray, P. Segall, Y. Aoki, and T. Kato, (2001), Estimation source parameters from deformation data, with an application to the March 1997 earthquake swarm off the Izu Peninsula Japan, *J. Geophys. Res.*, 106, pp. 11,217-11,237.

Estabrook, C., and T. Boyd, (1992), The Shumagin Islands, Alaska, earthquake of 31 May 1917, *Bull. Seismol. Soc. Am.*, 82, 755-773.

Fletcher, H., J. Beavan, J. Freymueller, and L. Gilbert, (2001), High interseismic coupling of the Alaska subduction zone SW of Kodiak Island inferred from GPS data, *Geophys. Res. Lett.*, 28, 443-446.

Freymueller, J., and J. Beavan, (1999), Absence of strain accumulation in the western Shumagin segment of the Alaska Subduction zone, *Geophys. Res. Lett.*, 26, 3233-3236.

Heki, K., and Y. Tamura, (1997), Short term afterslip in the 1994 Sanriku-Haruka-Oki earthquake, *Geophys. Res. Lett*., 24, 3285–3288.

Heki, K., S. Miyazaki, and H. Tsuji, (1997), Silent fault slip following an interplate thrust earthquake at the Japan Trench, *Nature,* 386, 595-598, doi:10.1038/386595a0.

Igarashi, T. T. Matsuzawa, and A. Hasegawa, (2003), Repeating earthquakes and interplate aseismic slip in the northeastern Japan subduction zone, *J. Geophys. Res.,* 108, doi:10.1029/2002JB001920.

Larson, K., and M. Lisowski, (1994), Strain accumulation in the Shumagin Islands: Results of initial GPS measurements, *Geophys. Res. Lett.*, 21, 489-492.

Mackey, K., K. Fujita, L. Gunbina, V. Kovalev, V. Imaev, B. Koz'min, and L. Imaeva, (1997), Seismicity of the Bering Strait region; Evidence for a Bering block, *Geology*, 25, 979-982.

Mann, D., and J. Freymueller, (2003), Volcanic and tectonic deformation on Unimak Island in the Aleutian Arc, Alaska, *J. Geophys. Res.*, *108*(B2), 2108, doi:10.1029/2002JB001925.

Nishenko, S., and Jabob, K., (1990), Seismic potential of the Queen Charlotte-Alaska-Aleutian Seismic Zone, *J. Geophys. Res.*, 95, 2511-2532.

Okada, Y., (1992), Internal deformation due to shear and tensile faults in a half-space, *Bull. Seismol. Soc. Am.*, 82, 1018-1040.

Oleskevich, D., R. Hyndman, and K. Wang, (1999), The updip and downdip limits to great subduction earthquakes: Thermal and structural models of Cascadia, south Alaska, SW Japan and Chile, *J. Geophys. Res.*, 104, 14,965-14,991.

Pacheco, J., L. Sykes, and C. Scholz, (1993), Nature of seismic coupling along simple plate boundaries of the subduction type, *J. Geophys. Res.*, 98, 14133-14159.

Sauber, J., G. Carver, S. Cohen, and R. King, (2006), Crustal deformation and the seismic cycle across the Kodiak Islands, Alaska, *J. Geophys. Res.*, 111, B02403, doi:10.1029/2005JB003626.

Savage, J., (1983), A dislocation model of strain accumulation and release at a subduction zone, *J. Geophys. Res.*, 88, 4984-4996.

Savage, J., and M. Lisowski, (1986), Strain Accumulation in the Shumagin seismic gap, Alaska, *J. Geophys. Res.*, 91, 7447-7454.

Savage, J., J. Svarc, and W. Prescott, (1999), Deformation across the Alaska-Aleutian subduction zone near Kodiak, *Geophys. Res. Lett.*, 26, 2117-2120.

Sella, G., T. Dixon, and A. Mao, (2002), REVEL; a model for recent plate velocities from space geodesy, *J. Geophys. Res.,* 107, doi:10.1029/2000JB000033.

Von Huene, R., M. Fisher, and T. Burns, (1987), Geology and evolution of the Kodiak margin, Gulf of Alaska, *Geology and Resource Potential of the Continental Margin of Western North America and Adjacent Ocean Basins – Beaufort Sea to Baja California*, D. Scholl, A. Grantz, J. Vedder, eds. Houston, Texas, Circum-Pacific Council for Energy and Mineral Resources, pp. 119-212.

Wiemer, S., and M. Wyss, (1997), Mapping the frequency-magnitude distribution in asperities: an improved technique to calculate recurrence times?, *J. Geophys. Res.,* 102, 15,115-15,128.

Zheng, G., R. Dmowska, and J. Rice, (1996), Modeling earthquake cycles in the Shumagin subduction segment, Alaska, with seismic and geodetic constraints. *J. Geophys. Res.,* 101, 8383-8392.

Chapter 5: Inflation Detected at Mt. Veniaminof Alaska with Campaign GPS[3]

5.1 Abstract

In 2005 a repeat GPS campaign was conducted at 12 sites on Mt.Veniaminof Volcano and the surrounding region. A previous survey in 2002 provided initial locations for the sites. The deformation that occurred in the three years between the two surveys consist of ~2-4cm of displacement caused by the northwest convergence of the Pacific and North America Plates and ~0.5-1cm displacements caused by a deep intrusion that may be associated with eruptive activity in 2003-2005. The site velocities are corrected for compression due to a locked subduction zone and modeled with volcanic sources in homogeneous and layered material. Although the data are fit equally well by several source models, we nevertheless gain important information about the deformation source. The best fitting models have depths that range from 4.7 to 11km and volume changes of 3.2 to 7.1 x10^6 m^3/yr, assuming incompressible magma.

5.2 Introduction

Mount Veniaminof is located on the Alaska Peninsula ~750 km southwest of Anchorage (Fig. 5.1). Veniaminof is a large, 350 km^3, volcanic edifice capped by an ice filled caldera that is 8 km in diameter. Historical eruptions have consisted of small-volume basaltic to andesitic Strombolian and effusive eruptions from a cone located in the western portion of the caldera. An eruption in 1983-1984 produced a 40x10^6 m^3 lava flow that formed a melt pit in the caldera glacier at the foot of the eruptive cone [*Miller et al., 1998*]. During 1993-1995 activity at the eruptive cone produced a small lava flow approximately 20x10^6 m^3 [*Miller et al., 1998*]. Between 2003 and 2005, steam and ash emissions were observed from the intra-caldera cone. In February 2005, incandescent lava fountaining was visible from the nearby village of Perryville [*McGimsey et al., 2008; De Angelis and McNutt, 2007*], and was captured by an Alaska Volcano Observatory

[3] Fournier, T., and J. Freymueller, (2008), Inflation detected at Mt. Veniaminof, Alaska with campaign GPS, *Geophys. Res Lett.,* 35, L20306, doi:10.1029/2008GL035503.

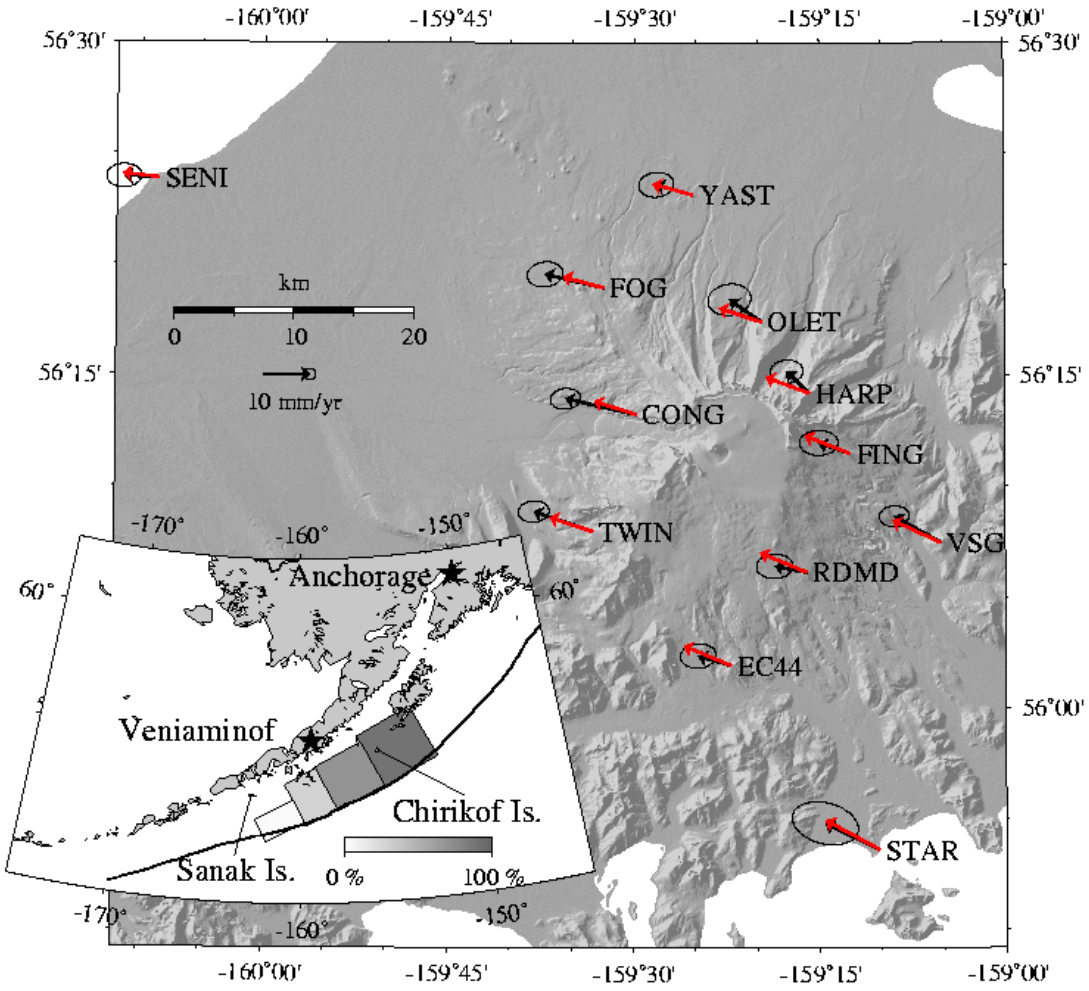

Figure 5.1: Veniaminof volcano and the GPS sites used in the study are shown with the site velocities relative to North America and 95% confidence ellipses in black. The red vectors are the velocities predicted by the *Fournier and Freymueller* [*2007*] subduction zone model, shown in the inset, with the scale bar showing the amount of locking on each rectangular patch. The inset map shows southwest Alaska and the location of Veniaminof and other localities discussed in the text (section 5.2). The thick black line is the location of the Aleutian trench. The base map is a digital elevation model obtained from the Shuttle Radar Topography Mission.

(AVO) web-camera located in the village. *De Angelis and McNutt* [*2007*] interpret seismic activity in November-December 2004 as an indication of an intrusion, and tremor that occurred in January-February 2005, during the most vigorous seismic and eruptive activity in the recent unrest, as a result of gas release processes. The activity in 2005 led to the reoccupation of 12 GPS benchmarks located on and near the volcano, most of which had been previously surveyed in 2002 (Fig. 5.1). This is the first study of deformation at Veniaminof.

Subduction related deformation is a major contributor to the deformation field in the region. Deformation caused by convergence of the Pacific Plate varies substantially along strike of the Alaska Peninsula, and can be as large as 1.5cm/yr, so it must be removed before the volcanic signal can be studied. *Fletcher et al.* [*2001*] examined the plate interface to the northeast of Veniaminof, near Chirikof Island, and found a large slip deficit equivalent to ~80% of the plate convergence rate. *Freymueller and Beavan* [*1999*] studied site velocities to the southwest near Sanak Island and determined that the plates were freely slipping in that region. Thus, Veniaminof lies in a transitional region between the two extremes. *Fournier and Freymueller* [*2007*] used velocities from 27 sites along the Alaska Peninsula to construct a regional subduction model. Sites close to Veniaminof were specifically excluded from that study, in order to avoid contamination of the tectonic model with volcanic deformation. Their results showed a gradation of the amount of locking on the plate interface from highly coupled near Chirikof Island to freely slipping near Sanak Island (Fig. 5.1). The plate interface near Mt. Veniaminof features a wide locked zone, very similar to the Chirikof Island region, which produces significant compression across the peninsula where the GPS network is located.

5.3 Data

Data from 12 sites are used to examine volcanic deformation at Veniaminof. Two campaign GPS surveys conducted in the summer of 2002 and the summer of 2005 are used to determine site velocities relative to the North America plate. All daily positions are determined using the GIPSY-OASIS processing software version GOA4, and site

velocities are determined in a least squares sense from the daily position estimates. These velocities are a subset of a much larger velocity solution [*Freymueller et al., 2008*]. The velocities are corrected for tectonic convergence between the Pacific and North American plates using the model of *Fournier and Freymueller* [*2007*] and examined for deformation associated with Veniaminof Volcano. We use the three-component velocities to constrain a deformation source beneath the volcano (Table 5.1).

Figure 5.1 shows the Veniaminof site velocities relative to North America (black) and the model results (red) from *Fournier and Freymueller* [*2007*]. The residuals from those velocities indicate a volcanic source of deformation (Fig. 5.2). We examine that residual deformation in the next section.

5.4 Methods

Two different source geometries are used to investigate the volcano deformation: an isotropic point source [*Mogi, 1958*], and a planar dislocation representing an expanding sill [*Okada, 1992*]. We solve for displacements due to these sources in a homogeneous half-space with a shear modulus of 30GPa and in a layered half-space that is constructed from a 1-D seismic velocity structure [*Sanchez, 2005*] (Fig. 5.2). In both earth models we assume a Poisson's ratio of 0.25. The elastic model is simplified into four layers (Fig. 5.2) and the propagator method is used to solve for displacements caused by a sill and isotropic point source in the layered half-space [e.g. *Johnson and Segall, 2004; Wang et al., 2003*]. For each source we use the simulated annealing (SA) algorithm [e.g. *Cervelli et al., 2001*] to find the optimal location, orientation and strength.

The SA method involves randomly sampling the parameter space from a probability distribution function (PDF), while at the same time systematically altering the characteristics of the PDF. The PDF is defined as

$$P_i = e^{-\frac{MSE_i}{T}}, \tag{5.1}$$

where MSE_i is the mean square error for the *ith* set of possible parameter values. The temperature, T, is used to alter the characteristics of the PDF and progresses, according to

Table 5.1: Veniaminof GPS network station locations and velocities (mm/yr) relative to North America and with the regional velocity model of *Fournier and Freymueller* [*2007*] removed. ±1σ uncertainties are shown for the east, north and vertical components.

Station	Longitude	Latitude	East	North	Vertical	σ_e	σ_n	σ_v
YAST	-159.4203	56.3856	0.8	-0.2	2.8	1.5	1.1	3.2
FOG	-159.5409	56.3158	-3.9	0.6	1.9	1.6	1.1	3.3
OLET	-159.3277	56.2904	2.3	1.8	3.3	1.9	1.4	4.1
CONG	-159.4965	56.2207	-6.1	0.6	10.3	1.3	0.9	2.9
HARP	-159.2629	56.2366	4.5	1.2	9.4	1.5	1.0	3.2
FING	-159.2085	56.1913	3.0	-1.6	5.6	1.7	1.1	3.4
TWIN	-159.5546	56.1327	-3.4	1.3	11.7	1.4	0.9	2.9
RDMD	-159.2668	56.1019	3.1	-2.9	4.6	1.6	1.1	3.3
VSG	-159.0865	56.1241	3.1	0.9	-0.8	1.3	0.9	2.8
STAR	-159.1699	55.8936	-0.1	-0.7	2.5	2.9	1.9	5.5
EC44	-159.3684	56.0319	3.1	-2.2	-0.6	1.6	1.1	3.3
SENI	-160.1434	56.3976	0.2	-0.6	5.4	1.5	1.0	3.2

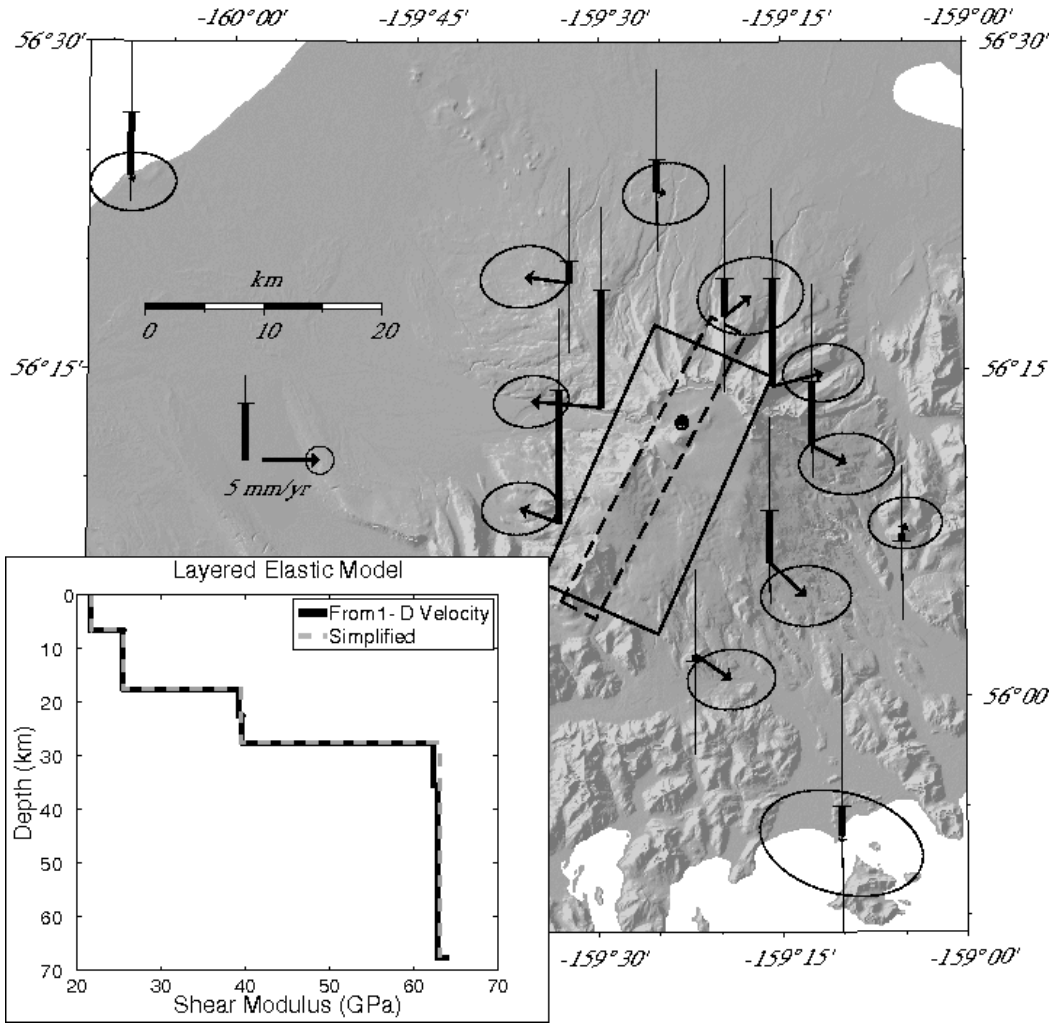

Figure 5.2: The GPS velocities highlight the volcano deformation after the tectonic component has been from the observed North America relative velocities (Figure 5.1). Horizontal velocities are indicated by the arrows with 95% confidence ellipses. Vertical velocities are the vertical bars with a horizontal bar indicating up or down motion. The 95% confidence interval for the vertical component is indicated by the thin vertical line. The best fitting models are shown; sill in homogeneous half-space (solid line), sill in a layered half-space (dashed line), Mogi source in a homogeneous half-space (solid dot), Mogi source in a layered half-space (open dot) (note that the both Mogi sources are in almost the exact same location). The layered model, calculated using a p-wave velocity model [*Sanchez, 2005*] is shown in the inset (black). The elastic structure is simplified into a four layer model (grey dashed) that is used for the deformation source inversions.

a “cooling schedule”, from a high to a low value at each iteration of the annealing process. For each simulation the PDF begins as an evenly distributed function and is allowed to grow sharper with more defined peaks as the simulation evolves. This allows for the model to step out of local misfit minima and converge on the global minimum.

To initialize the SA process we define a parameter space that is searched for the optimal model geometry. Each model is allowed to be located within a 20x20 km area, centered on the active cone and at depths between 0.5km and 30km. In addition to the location each model requires a strength term which is related to the magnitude of deformation. The strike and dip of the sill are allowed to have any value in the range -180º to 180º and 0º to 90º respectively, accounting for either a sill or a dike. The inversion excludes everything except shallowly dipping sills. The lengths of the sides of the sill are given a range of 0.1km to 15km. The final step of the SA process is a Levenberg-Marquardt “steepest-descent” algorithm to find the local minimum. This step does not have boundaries on the parameter space so the final model may fall outside of the initially defined region.

5.5 Results

All of the models predict similar attributes about the deformation source including the depth, horizontal location and the volume change (Table 5.2). The best fitting Mogi models are each located in the northwest quadrant of the caldera at ~8km depth, while the sills strike northeast across the caldera but have depth estimates that changes by a factor of 2 when a layered space is used in place of a uniform half-space. At the 95% confidence level, each volcanic source model improves the fit to the data over the tectonic model alone.

All of the source models provide a comparable fit to the data. A sill in a homogeneous half-space provides the smallest MSE, but the models are not distinguishable in terms of the misfit to the data. A relatively deep source depth, or large areal extent for the sill models, is required to give the proper distribution of uplift at the closest sites. The amount of opening on the sill is inversely proportional to the size of the

Table 5.2: Best fitting model parameters fit to velocities derived from GPS campaigns in 2002 and 2005 at Veniaminof Volcano.

	MSE	X(km) [a]	Y(km)[a]	Depth(km)	Length(km)	Width(km)	Dip(º)	Strike(º)	ΔV (m^3/yr)
Mogi	1.76	0.1	1.4	7.4	-	-	-	-	3.5e+6
Mogi (layer)	1.80	0.1	1.5	8.3	-	-	-	-	3.2e+6
Sill	1.00	-7.0[b]	-1.1[b]	4.7[b]	24	11	-5	200	9.1e+6[c]
Sill (layer)	1.21	-3.8 [b]	-1.6[b]	11[b]	27	3.3	-4	210	7.1e+6[c]

[a] The horizontal position is relative to the active cone; 159.39º W 56.196º N.

[b] The sill location is defined by the middle top edge of the plane.

[c] The change in volume corresponds to ~0.04m (sill) and ~0.08m (sill,layer) opening per year.

plane, such that a smaller sill with more opening will produce similar displacements as a larger sill with less opening. Even with this trade-off, the larger sill is needed to fit the horizontal and vertical velocities observed at TWIN and EC44. The small amount of opening estimated for the sill models does not likely represent the full dimensions of an intrusion. This is likely the result of either over-estimating the area of the sill or the 2002-2005 inflation representing only part of the expansion of a pre-existing sill.

Figure 5.2 shows the surface projection of the four models. The sill models have a northeast-southwest orientation and extend beyond the edifice in the southwest direction. The extreme length of the sills may be the result of lacking station coverage on the southwest flank to constrain the length of the sill in this direction. Table 5.2 gives the parameter values of the best fitting models. The volume change estimates given here assume incompressible magma. We also tried a spheroid source [*Yang et al., 1988*], but exclude these results because the orientation of the best-fitting spheroid is not consistent with geologic structures.

Figures 5.3-5.6 show the results from uncertainty analysis of the source models, conducted by randomly perturbing the data by amounts that have been sampled from a distribution described by the data covariance matrix. A Levenberg-Marquardt algorithm is used to invert the perturbed data for the model parameters, where the best model from the SA results is used as the initialization for the inversion. Regardless of source model or earth model, there is a strong peak for most parameters, but long non-Gaussian tails to the distribution of models. The tails are often asymmetric, as a result of the non-linearity of the inversion. Both 68% and 95% confidence intervals are given in Table 5.3 to give a truer assessment of the uncertainty and indicate the magnitude of skewness in the distributions. For example the Mogi source depth has a 95% confidence interval of ~3.5-17km while the 68% confidence interval is ~5-12km, indicating the tail toward the deeper depth range. While the Mogi source models have a similar depth ranges, there is a clear distinction between the depth estimates for the sill in a homogenous medium, compared

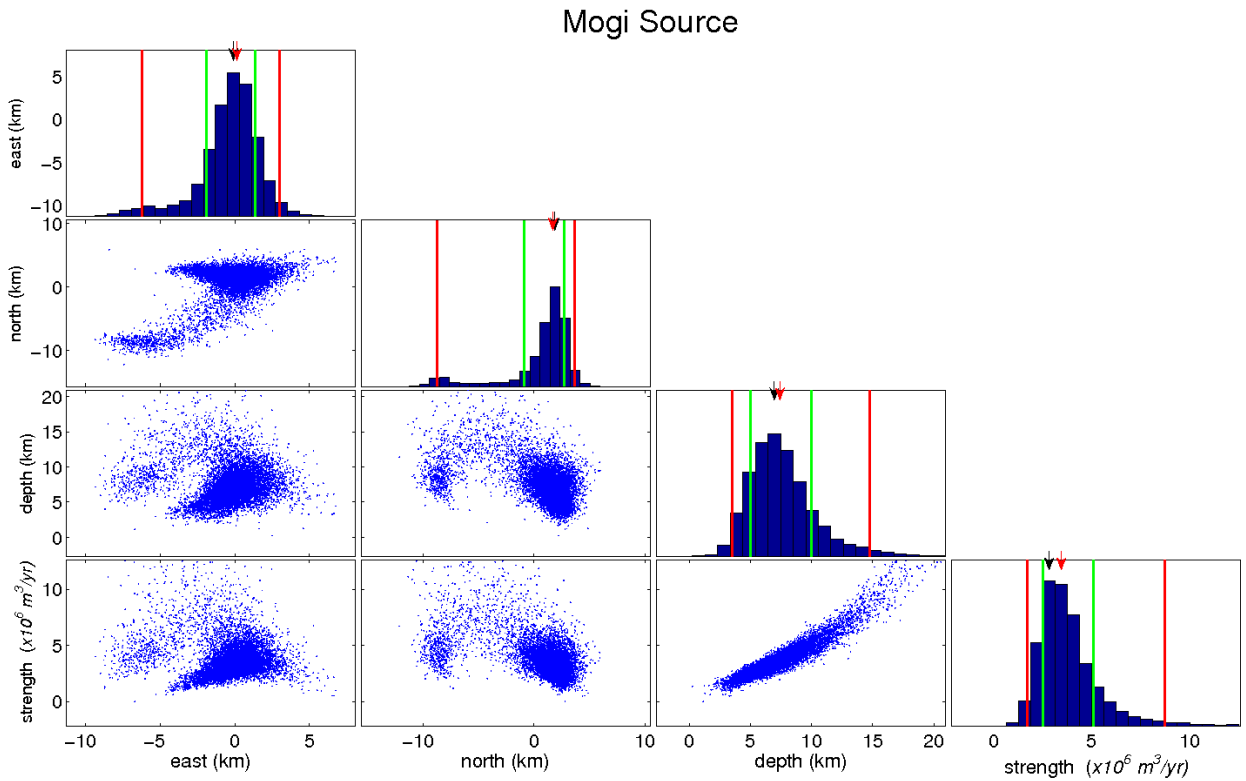

Figure 5.3: Uncertainties in the Mogi source parameters are determined using data perturbation. The red lines in the histograms show the upper and lower 95% confidence boundaries for each parameter, and the greens lines are the 68% (1σ) boundaries. East, north and depth are the geometric position of the Mogi source and strength is the volume change. The red arrows show the parameter values from the simulated annealing results and the black arrows show the peaks of the distributions.

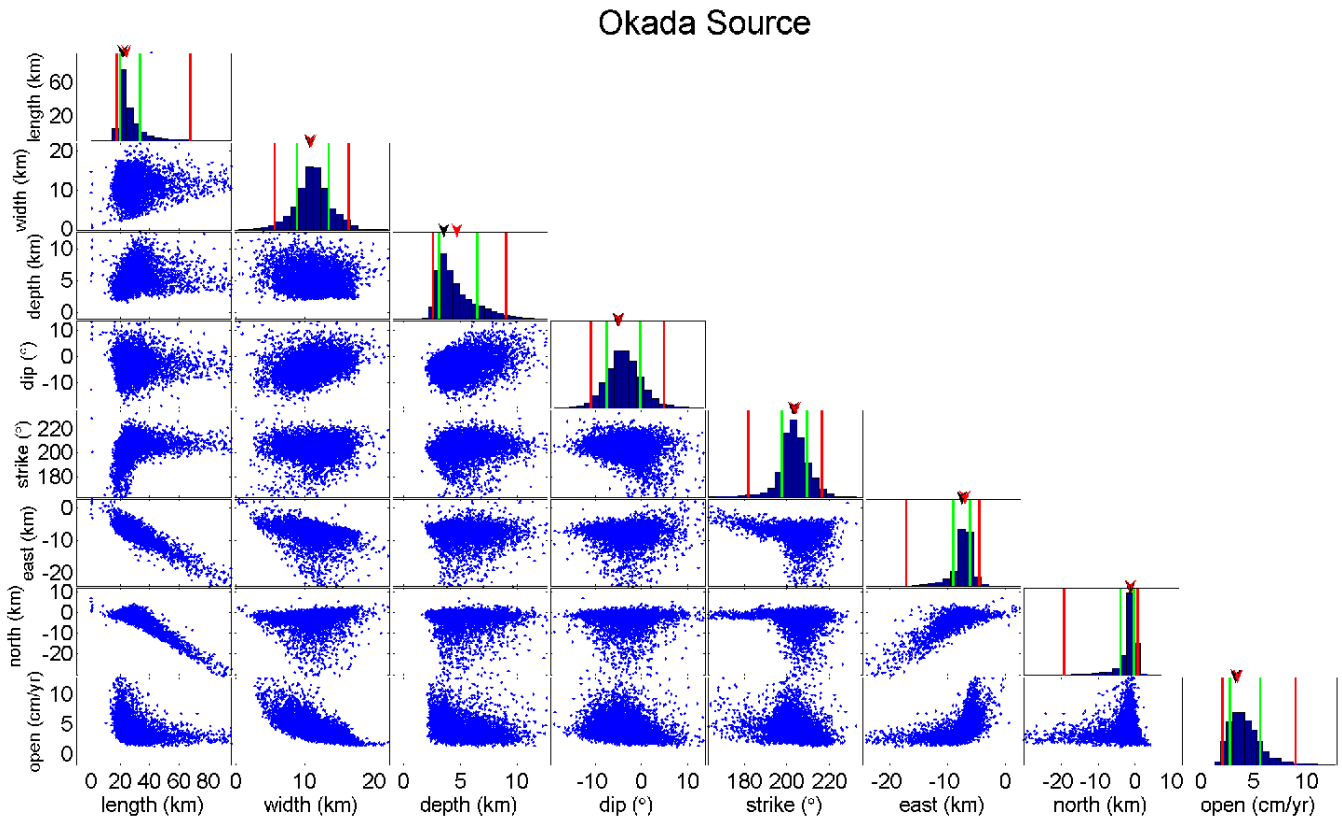

Figure 5.4: Uncertainties in the sill source parameters are determined using data perturbation. The red lines in the histograms show the upper and lower 95% confidence boundaries for each parameter, and the greens lines are the 68% (1σ) boundaries. The red arrows show the parameter values from the simulated annealing results and the black arrows show the peaks of the distributions.

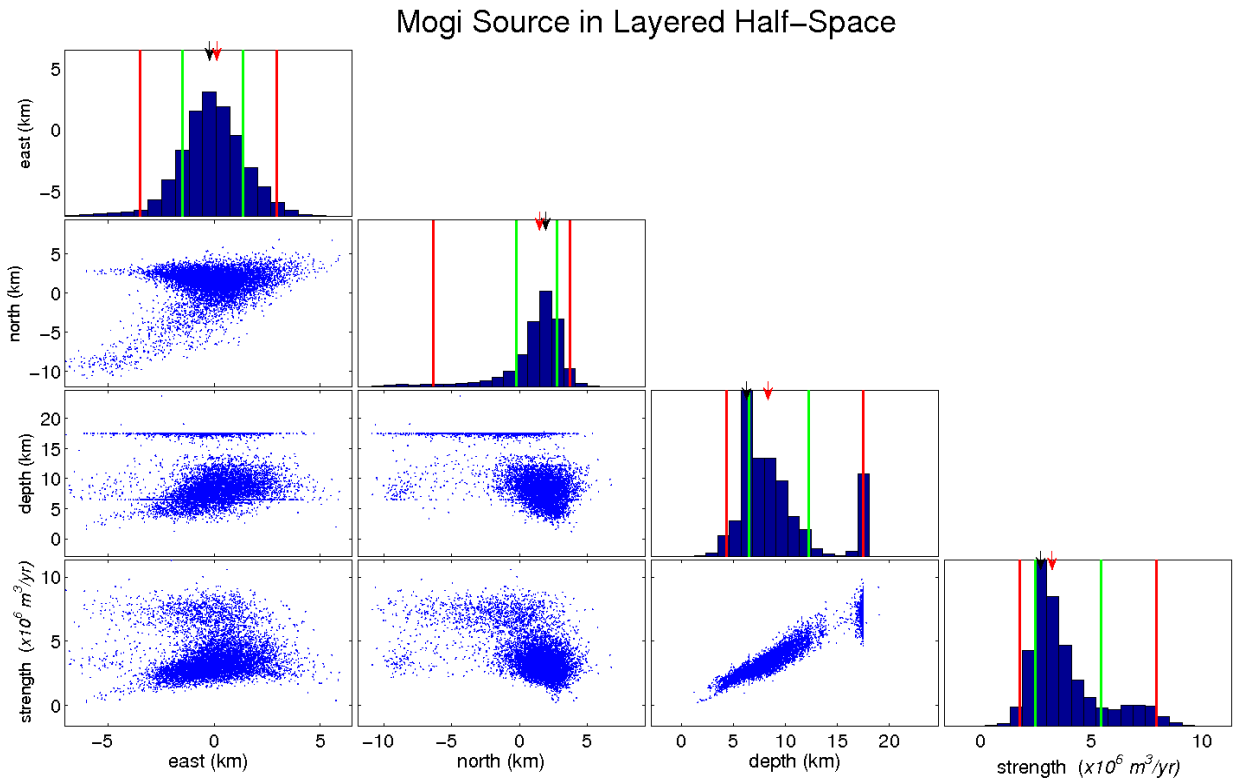

Figure 5.5: Uncertainties in the parameters for a Mogi source in a layered half-space are determined by data perturbation. The red lines in the histograms show the upper and lower 95% confidence boundaries for each parameter, the green lines show the 68% (1σ) boundaries. East, north and depth are the geometric position of the Mogi source and strength is the volume change. The red arrows show the parameter values from the simulated annealing results and the black arrows show the peaks of the distributions.

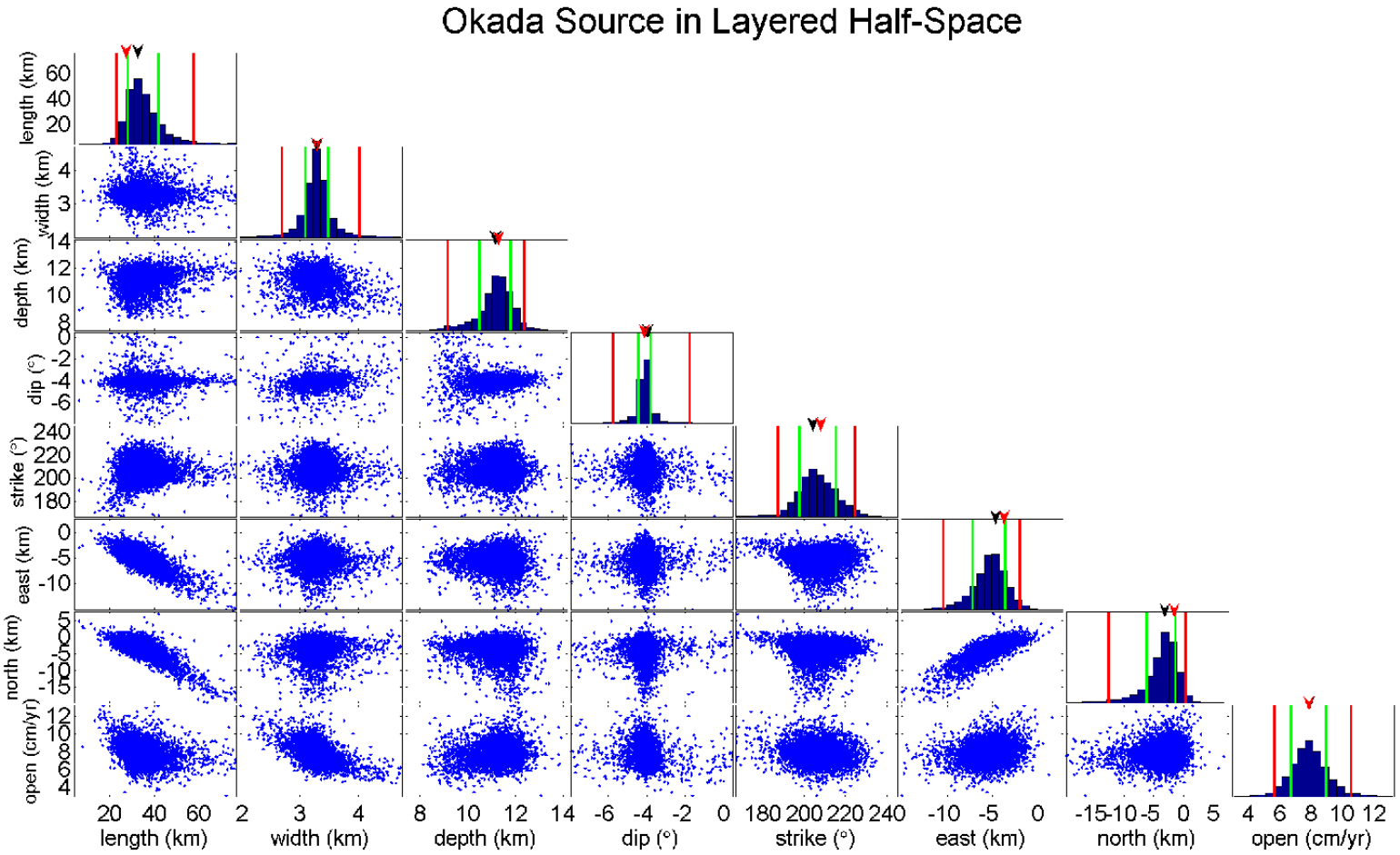

Figure 5.6: Uncertainties in the parameters for a sill source in a layered half-space are determined by data perturbation. The red lines in the histograms show the upper and lower 95% confidence boundaries. The red arrows show the parameter values from the simulated annealing results and the black arrows show the peaks of the distributions.

Table 5.3: Confidence boundaries are determined by data perturbation. The 95% and 68% confidence boundaries for source models fit to velocities derived from GPS campaigns in 2002 and 2005 at Veniaminof Volcano are shown. Figures 5.4-5.6 show the bootstrap results from which these confidence bounds were derived.

	Mogi				Mogi (layer)				Sill				Sill (layer)			
	95% limits		68% limits		95% limits		68% limits		95% limits		68% limits		95% limits		68% limits	
East (km)[a]	-6.2	3.0	-1.9	1.4	-3.5	2.9	-1.5	1.4	-17	-4.3[b]	-9.0	-6.0[b]	-10	-1.9[b]	-7.2	-3.6[b]
North (km)[a]	-8.8	3.7	-0.9	2.7	-6.4	3.7	-0.2	2.7	-19	0.8[b]	-3.9	-0.2[b]	-13	0.4[b]	-6.2	-1.3[b]
Depth (km)	3.5	15	5.0	9.9	4.3	17	6.5	12	2.6	9.1	3.2	6.5	9.2	12	11	12
$\Delta V(x10^6\ m^3/yr)$/ opening (cm/yr)	1.7	8.7	2.5	5.1	1.8	8.0	2.5	5.4	2.0	9.0	2.8	5.6	5.7	11	6.8	9.0
Dip (°)	-	-	-	-	-	-	-	-	-11	5.0	-7.4	-0.1	-10	-1.9	-4.4	-3.8
Strike (°)	-	-	-	-	-	-	-	-	180	220	200	210	190	220	200	220
Length (km)	-	-	-	-	-	-	-	-	18	68	20	34	23	58	28	42
Width (km)	-	-	-	-	-	-	-	-	5.7	16	8.9	14	2.7	4.0	3.1	3.5

[a] The horizontal position is relative to the active cone; 159.39º W 56.196º N.

[b] The sill location is defined by the middle top edge of the plane.

to the sill in a layered medium. Except for the depth of the sill model, the uncertainties in the layered and homogeneous models are comparable.

5.6 Discussion

The inflation at depth is a result of either the intrusion of new magma, or from pressurization of existing magma at depth caused by an increase in its volatile volume. Either of these processes may be providing magma or fluids to shallower depths. *De Angelis and McNutt*, [*2007*] suggest that shallow degassing, within a few hundred meters of the surface, may be the trigger for harmonic tremor that was recorded on the local seismic network from January–February 2005. They suggest that volcano-tectonic earthquakes in December 2004 and January 2005 may be associated with ascent of magma to the shallow sub-surface, and low-frequency earthquakes that occurred in January 2005 could be associated with degassing through the shallow magma column. The inflation recorded during this time may reflect a deep accumulation of magma prior to or coincident with magma ascent to shallow depths. Our station distribution cannot resolve sources at shallow depths.

Petrologic observations provide constraints for the relative structure of the magmatic system beneath Veniaminof. *Bacon et al.* [*2007*] describe a first order model of a crystal mush column below Veniaminof. They suggest that a shallow region of segregated felsic magma tops a crystal mush column that is occasionally intruded by basaltic magmas. The historical basaltic andesite eruptions indicate that this is the likely composition of any magma intrusion. The seismic pattern during the 2005 unrest is indicative of magma making its way to the shallow subsurface [*De Angelis and McNutt, 2007*]. The wide aperture GPS network can not detect shallow activity that may be occurring beneath the active cone, but the deep deformation source may signify a region where magma accumulated before a small portion made its way to shallower depth. The magma accumulation area at depth may be a long-lived storage zone or a one-time intrusion. This intrusion agrees with the structural model proposed by *Bacon et al.* [*2007*] (Fig. 5.7),

and also provides a depth constraint as to where intrusions are occurring, although mafic intrusions likely occupy a range of depths beneath the volcano.

5.7 Conclusions

An inflation source is inferred at Veniaminof Volcano from two GPS campaigns conducted three years apart. Relatively small displacements at the 12 sites used in the study become evident when the data are examined in the context of regional compression across the Alaska Peninsula. The dispersed network is unable to resolve specific source geometries, but it does provide some important constraints on the depth of the deformation source. The best estimate of the source depth ranges from 4.7 to 11 km, depending on the source model and earth model assumed, indicating an intrusion into the middle of the upper crust.

Seismic and GPS observations during the recent unrest, characterized by steaming and minor ash emissions, indicate a magma intrusion at depth that eventually reached the surface. The observations indicate deformation is occurring within the crystal mush column described in the model put forward by *Bacon et al.* [*2007*] (Fig. 5.7), and is likely associated with mafic magma, consistent with their hypothesis. In their depiction of the sub-volcanic magma system the crystal mush column comprises a broad depth range below shallower segregated felsic magmas, and is occasionally intruded by basaltic magmas supplying heat to the system.

It is possible that this deformation is part of a long term trend or is an inflationary pulse unrelated to the eruptive activity. Even though the timing and distribution of observations are suboptimal, the deformation at Veniaminof can still be characterized by a relatively deep and small magnitude source.

Low level activity continues at Veniaminof. In late 2007 the seismic activity level increased, characterized by tremor, and by February 2008 the seismicity appeared similar to the observations during the 2005 eruptive event. Steam and ash plumes were observed during this time. As of this writing activity at the volcano has diminished, but the record

shows that low level activity comes and goes frequently and deformation observations can be useful in determining the source of unrest.

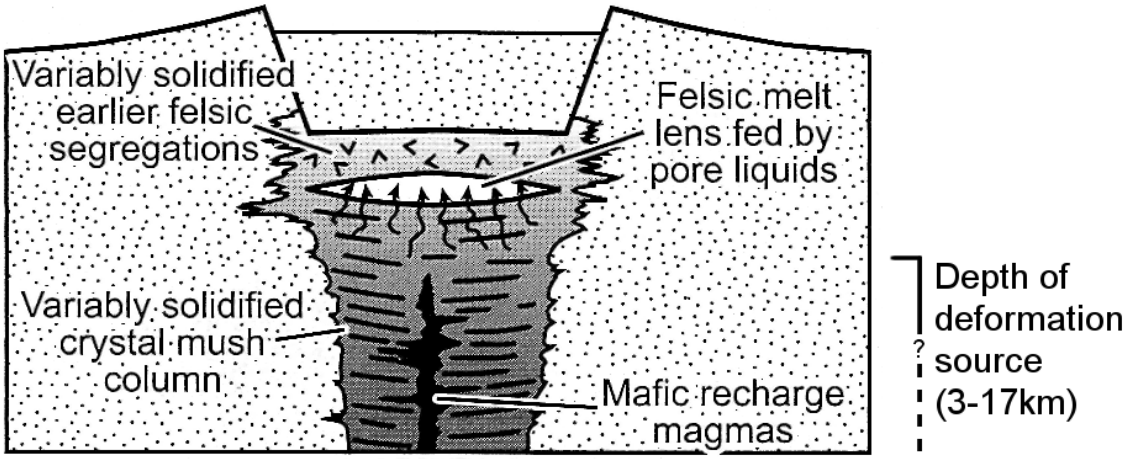

Figure 5.7: A diagram of the magmatic system beneath Veniaminof (modified from *Bacon et al.* [*2007*]) shows a relatively shallow region of felsic magmas above a crystal mush column. The observed deformation is consistent with originating from within the crystal mush column.

5.8 References

Bacon, C., T. Sisson, and T. Mazdab, (2007), Young cumulate complex beneath Veniaminof caldera, Aleutian arc, dated by zircon in erupted plutonic blocks, *Geology 35(6):* doi: 10.1130/G23446A.1.

Cervelli, P., M. Murray, P. Segall, Y. Aoki, and T. Kato, (2001), Estimating source parameters from deformation data, with an application to the March 1997 earthquake swarm off the Izu Peninsula, Japan. *Journal of Geophysical Research 106(B6),* doi: 10.1029/2000JB900399.

De Angelis, S., and S. McNutt, (2007), Observations of volcanic tremor during the January-February 2005 eruption of Mt. Veniaminof, Alaska, *Bulletin of Volcanology*, v. 69, p. 927-940, doi:10.1007/s00445-007-0119-4.

Fletcher, H., J. Beavan, J. Freymueller, and L. Gilbert, (2001), High interseismic coupling of the Alaska subduction zone SW of Kodiak Island inferred from GPS data. *Geophysical Research Letters 28(3):* doi: 10.1029/2000GL012258.

Fournier, T., and J. Freymueller, (2007), Transition from locked to creeping subduction in the Shumagin region, Alaska, *Geophys. Res. Lett.*, 34, L06303, doi:10.1029/2006GL029073.

Freymueller, J., and J. Beavan, (1999), Absence of strain accumulation in the Western Shumagin Segment of the Alaska Subduction zone, *Geophysical Research Letters, 26, p.3233-3236.*

Freymueller, J., H. Woodard, S. Cohen, R. Cross, J. Elliott, C. Larsen, S. Hreinsdóttir, and C. Zweck, (2008), Active deformation processes in Alaska, based on 15 years of GPS measurements, *Active Tectonics and Seismic Potential of Alaska, AGU Monograph.*

Johnson, K., and P. Segall, (2004), Imaging the ramp – decollement geometry of the Chelungpu fault using coseismic GPS displacements from the 1999 Chi-Chi, Taiwan earthquake, *Tectonophysics*, 278, doi:10.1016/j.tecto.2003.10.020.

McGimsey, R., C. Neal, J. Dixon, and S. Ushakov, (2008), 2005 Volcanic activity in Alaska, Kamchatka, and the Kurile Islands: Summary of events and response of the Alaska Volcano Observatory, *U.S. Geological Survey Scientific Investigations Report*, 2007–5269.

Miller, T., R. McGimsey, D. Richter, J. Riehle, C. Nye, M. Yount, and J. Dumoulin, (1998), Catalog of the historically active volcanoes of Alaska, *U.S. Geol. Surv. Open File Rep*., 98-0582.

Mogi, K., (1958), Relations between the eruptions of various volcanoes and the deformations of the ground surfaces around them, *Bulletin of the Earthquake Research Institute*, vol. 25, pp. 99-134.

Okada, Y., (1992), Internal deformation due to shear and tensile faults in a half-space, *Bull. Seismol. Soc. Am., 82, pp. 1018-1040*.

Sanchez, J., (2005), Volcano seismology from around the world: Case studies from Mount Pinatubo (Philippines), Galeras (Colombia), Mount Wrangell and Mount Veniaminof (Alaska), *University Of Alaska, Faribanks, Ph.D. Thesis*, pp. 128-169.

Wang, R., F. Martin, and F. Roth, (2003), Computation of deformation induced by earthquakes in a multi-layered elastic crust—FORTRAN programs EDGRN/EDCMP, *Computers and Geosciences*, 29, 195-207.

Yang, X., P. Davis, and J. Dieterich, (1988), Deformation from inflation of a dipping finite prolate spheroid in an elastic half-space as a model for volcanic stressing, *Journal of Geophysical Research, 93(B5), pp. 4249-4257.*

Chapter 6: Looking to the Future

6.1 Summary

The previous chapters demonstrated the usefulness and challenges in using GPS observations for studying volcano and tectonic deformation. The temporal variation of the deformation rate at Okmok was examined and interpreted as volatile rich magma intruding into a shallow reservoir followed by degassing. The study of Mt. Veniaminof showed that important inferences can be made even with a limited data set. It also stressed the importance of understanding the regional strain field. The change in properties along the subduction interface beneath the Alaska Peninsula has implications for the seismogenic potential of the region.

The Unscented Kalman Filter was used in Chp. 2 to track volume changes beneath Okmok Volcano. The non-linear inversion technique was shown to be useful in combining data from the entire GPS network and in reducing noise and undesirable signals from the displacement record. The filtering method estimated a deformation source located at the center of the caldera and at ~2.5km below sea level. This is consistent with previous studies.

The volume change estimate obtained in Chp. 2 reveals deflation signals following large inflation pulses at Okmok. The volume change record is examined in further detail in Chp.3, where a degassing model is proposed to explain the deflation signals. A thermodynamic model is used to determine magma properties, and volatile concentrations. In the model, degassing is assumed to be the source of deflation. A degassing intrusion explains the observations when the magma chamber is assumed to be <2.5km in radius and when the volatile concentration is >4.5wt.% H_2O.

Chp. 4 examines the regional strain field along the Alaska Peninsula. The convergence of the Pacific and North American Plates is a major contributor to deformation in the region. The source of the deformation is plate coupling in the seismogenic region of the mega-thrust. Velocities from GPS sites along the Alaska

Peninsula show that the amount of coupling decreases dramatically south of the Shumagin Islands. The amount of coupling directly affects the seismic potential of the fault.

Mt. Veniaminof is located on the Alaska Peninsula in the region covered in Chp. 4. Chp. 5 presents the first observations of deformation at Mt. Veniaminof. The relatively small volcanic signal is masked by deformation caused by plate convergence. The model created in Chp. 4 is applied to the data at Mt. Veniaminof to reveal a clear volcanic deformation source. An intrusion associated with eruptive activity in 2005 is the source of the deformation.

6.2 Future Studies

The work presented here can be expanded on to increase our understanding of volcanic processes of Okmok and Mt. Veniaminof. The models and analysis techniques can be utilized for different volcanic systems. Outlined below are a few ways to expand on these studies.

The time series analysis method presented in Chp. 2 can be used for rapid interpretation of real-time data to assist in volcano and earthquake monitoring. The 2008 eruption of Okmok Volcano is a great example. The Unscented Kalman Filter was used to estimate the volume change beneath the volcano. Although the system was not set up for automated processing the eruption showed the usefulness of this method and illustrated the benefit that having these solutions in near real-time would provide.

The deformation record at Okmok should be examined in further detail in light of the recent eruption, and together with information from InSAR, seismology, and petrology. The analysis on degassing at Okmok in Chp. 3 could be expanded with additional constraints from petrologic experiments. The seismic record could be examined during times of supposed vigorous degassing to see if seismic stations may have recorded such an event.

The transition from a locked to a creeping subduction zone interface along the Alaska Peninsula has important implications for the seismic hazard posed by the mega-

thrust. The transition also poses some important questions such as, what causes the interface to slip easily or become locked. A better understanding of this transition zone can be partly achieved by a denser GPS network in the region and continuous GPS to provide a better temporal record of ground motion. This study should be revisited after the recently installed Plate Boundary Observatory (PBO) GPS network has collected enough data for precise site velocity estimates. Although the PBO network adds to our current record, more stations would further rectify the transition zone along the plate interface.

The small volcanic deformation signal observed at Mt. Veniaminof would have been exceedingly difficult to identify and harder to interpret without the use of an accurate regional model. Out of this study come some important recommendations to improve future deformation studies at Mt. Veniaminof. Too few data is often the reality when conducting geophysical studies, but the addition of one or two more stations could dramatically improve the constraints on the plumbing system beneath the volcano. The frequent low level activity at the volcano makes it an ideal candidate for investigations on fluid migration and studies comparing pre-eruptive deformation to deformation not associated with eruptive activity.

6.3 Concluding Remarks

GPS instruments have been proven as an effective tool for examining active geologic processes. With recent advances in computing and processing methods, GPS is beginning to move toward a real time and rapid response tool. The ability to obtain GPS solutions rapidly requires tools to quickly and accurately interpret the results. The Unscented Kalman Filter can be useful in promptly analyzing data from many sites in terms of a specific model. Further studies of these systems can also improve our ability to interpret the observations.